Project 010 Aircraft Technology Modeling and Assessment

Georgia Institute of Technology and Purdue University

Project Lead Investigators

Dimitri Mavris (PI)
Regents Professor
School of Aerospace Engineering
Georgia Institute of Technology
Mail Stop 0150
Atlanta, GA 30332-0150
404-894-1557
dimitri.mavris@ae.gatech.edu

William Crossley (PI)
Professor
School of Aeronautics and Astronautics
Purdue University
701 W. Stadium Ave
West Lafayette, IN 47907-2045
765-496-2872
crossley@purdue.edu

Jimmy Tai (Co-PI)
Senior Research Engineer
School of Aerospace Engineering
Georgia Institute of Technology
Mail Stop 0150
Atlanta, GA 30332-0150
404-894-0197
jimmy.tai@ae.gatech.edu

Daniel DeLaurentis (Co-PI)
Professor
School of Aeronautics and Astronautics
Purdue University
701 W. Stadium Ave
West Lafayette, IN 47907-2045
765-494-0694
ddelaure@purdue.edu

University Participants

Georgia Institute of Technology

- PI(s): Dr. Dimitri Mavris (PI), Dr. Jimmy Tai (Co-PI)
- FAA Award Numbers: 13-C-AJFE-GIT-006, 13-C-AJFE-GIT-012, 13-C-AJFE-GIT-022, 13-C-AJFE-GIT-031, 13-C-AJFE-GIT-37, 13-C-AJFE-GIT-041, 13-C-AJFE-GIT-50, 13-C-AJFE-GIT-52, 13-C-AJFE-GIT-56, 13-C-AJFE-GIT-76, 13-C-AJFE-GIT-94
- Period of Performance: September 1, 2020 to August 31, 2021

- Task(s):
    1. Demand assessment
    2. Fleet analysis
    3. Aviation Environmental Design Tool (AEDT) supersonic modeling
    4. Support Committee on Aviation Environmental Protection (CAEP) supersonic exploratory study
    5. SST modeling in AEDT
    6. Coordination

Purdue University

- PI(s): Dr. William A. Crossley (PI), Dr. Daniel DeLaurentis (Co-PI)
- FAA Award Numbers: 13-C-AJFE-PU-004, 13-C-AJFE-PU-008, 13-C-AJFE-PU-013, 13-C-AJFE-PU-018, 13-C-AJFE-PU-026, 13-C-AJFE-PU-032, 13-C-AJFE-PU-035, 13-C-AJFE-PU-044
- Period of Performance: September 1, 2020 to August 31, 2021
- Task(s):
    1. Demand assessment
    2. Fleet analysis
    4. Support CAEP supersonic exploratory study
    5. SST modeling in AEDT

Project Funding Level

The project is funded by FAA at the following levels: Georgia Institute of Technology: $1,200,000; Purdue University; $222,116. Cost-sharing details are below:

The Georgia Institute of Technology has agreed to a total of $1,200,000 in matching funds. This total includes in-kind cost-sharing from GE and Boom; salaries for the project director, research engineers, and graduate research assistants (GRAs); and funding for computing, financial, and administrative support, including meeting arrangements. The institute has also agreed to provide tuition remission for the students, paid by state funds.

Purdue University provides matching support through salary support for the faculty PIs, and through salary support and tuition and fee waivers for one of the GRAs working on this project. OAG Aviation Worldwide Limited also provided in-kind cost-sharing to the Purdue team.

Investigation Team

Georgia Institute of Technology

- PI: Dimitri Mavris
- Co-Investigator: Jimmy Tai (Task 4)
- Vehicle Modeling Technical Leads: Greg Busch, Russell Denney, Jai Ahuja, Christian Perron, and Chung Lee
- Fleet Modeling Technical Leads: Holger Pfaender, Dushhyanth Rajaram, Michelle Kirby, Mayank Bendarkar, and Mohammed Hassan (Tasks 1, 2, and 5)
- Graduate Students: Nikhil Iyengar, Barbara Sampaio, Edan Baltman, Kaleb Cornick, Brennan Stewart, Ezgi Balkas, David Shalat, Mengzhen Chen, Joao De Azevedo, Colby Weit, Jiajie (Terry) Wen, and Ted Vlady

Purdue University

- PI: William Crossley (Tasks 1,2, 4, and 5)
- Co-Investigator: Daniel DeLaurentis (Tasks 1, 2, 4, and 5)
- Graduate Students: Samarth Jain, Suzanne Swaine, Tien-Yueh Fung, and Boning Yang

Project Overview

Georgia Institute of Technology (Georgia Tech) and Purdue University have partnered to investigate the future demand for supersonic air travel and the environmental impact of supersonic transports (SSTs). In the context of this research, environmental impacts include direct carbon dioxide (CO_2) emissions and fuel consumption. The research is conducted as a collaborative effort to leverage the capabilities and knowledge available from the multiple entities that make up the ASCENT university partners and advisory committee. The primary objective of this research project is to support the Federal Aviation Administration (FAA) in modeling and assessing the potential future evolution of the next-generation supersonic aircraft

fleet. The research in this project consists of five integrated focus areas: (a) establishing fleet assumptions and performing demand assessment; (b) performing preliminary SST environmental impact prediction; (c) testing the ability of the current Aviation Environmental Design Tool (AEDT) to analyze existing supersonic models; (d) performing vehicle and fleet assessments of potential future supersonic aircraft; and (e) modeling SSTs by using the modeling and simulation environment Framework for Advanced Supersonic Transport (FASST).

To better understand the potential demand for supersonic air travel, the team developed a parametric airline operating-cost model to explore the sensitivities of key vehicle, operational, and cost parameters on the required yield that an airline would need to target for ticket prices on potential new supersonic aircraft. The current model, however, assumes fixed parameters for key vehicle metrics, which can be changed but do not include sensitivities to key vehicle design choices such as vehicle size, design cruise Mach number, and maximum range. This task will examine the implications of the physical and technical dependencies on airline operational cost. Through the vehicle performance sensitivities, such as passenger capacity and design cruise Mach number, the combined "sweet spot," i.e., the most profitable vehicle for an airline to operate, can be determined. To accomplish this goal, the existing vehicle models created in the prior year will be utilized and supplemented with the additional vehicles proposed in Task 4. These vehicles together will serve as the foundation to create credible sensitivities regarding parameters such as vehicle size and design cruise Mach number. These sensitivities will then be embedded in the airline operating-cost estimation model and used to explore the combined vehicle and airline operational space to identify the most economically feasible type of supersonic vehicle.

In an independent complementary approach to consider the demand and routes for supersonic aircraft, the Purdue team developed a ticket pricing model for possible future supersonic aircraft that relies on the "as-offered" fares before the novel coronavirus (COVID-19) pandemic for business-class and first-class tickets on routes expected to have passenger demand for supersonic aircraft. Via an approach considering the number of passengers potentially demanding fares at business class or above on a city-pair route, the distance of that city-pair route, an adjustment to increase the over-water distance of the route where the aircraft can fly supersonically to allow for the shortest trip time, and the range capability of a low-fidelity modeled medium SST (55-passenger [pax] capacity) to fly that route with the shortest trip time, the Purdue team identified 258 potential routes that could potentially allow for supersonic aircraft service in a network of routes with at least one end (i.e., the origin or destination) in the United States. Of these 258 potential routes, 241 are direct, and 17 would require fuel stops but would still save travel time with respect to a subsonic non-stop flight on the same route. By providing these potential routes as input to the Fleet-Level Environmental Evaluation Tool (FLEET) simulation, the allocation problem in FLEET then determines which routes would be profitable for the airline to offer supersonic transportation and how many supersonic aircraft would operate on these routes, providing a prediction of which routes might have supersonic aircraft use and the number of supersonic flights operated on those routes at dates in the future. The analysis also explored the possible reaction of an airline to losing business-class passengers on subsonic aircraft, by including the allocation of a high-passenger-density aircraft on routes with supersonic service and considering various ticket pricing schema and associated changes in passenger demand. With the onset of the COVID-19 pandemic, the Purdue team updated the demand modeling to reflect the decrease in air travel and provided several scenarios for post-pandemic recovery. Near the end of this reporting period, the Purdue team began an effort to expand the fleet analysis tool, FLEET, from the United States-touching route network to a worldwide network.

One major accomplishment of the project during the performance period is the preliminary results for the design Mach trade study, which encompasses nine SST models developed in FASST. These nine vehicles make up three vehicle classes: business jet, medium, and large vehicle classes. The business jets were modeled to carry eight passengers for 4,240 nmi at Mach 1.4, 1.6, and 1.8. The medium-class SSTs were modeled to carry 55 passengers for 4,500 nmi at Mach 1.8, 2.0, and 2.2. Finally, the large-class SSTs were modeled to carry 100 passengers for 5,000 nmi at Mach 1.6, 1.8, and 2.0. All noise analyses incorporated Variable Noise Reduction System (VNRS), and all associated propulsion systems were of a clean-sheet design.

Georgia Tech and Purdue used their respective fleet analysis tools—Global and Regional Environmental Analysis Tool (GREAT) and the aforementioned FLEET—to produce estimates of the fleet-level impact of a potential fleet of supersonic aircraft operating in the future. The SSTs required for these fleet-level analyses were provided by the vehicle modeling tasks with FASST, a derivative framework from Environmental Design Space (EDS). The outcomes of this study provide a glimpse into the future potential state of supersonic air travel by using physics-based models of supersonic vehicle performance. Future work should build on current estimates to conduct more detailed analyses of vehicle and fleet performance.

Table of Acronyms and Symbols [Someone]

%Nc Fan	percent *corrected fan speed*
α	T/T_{SL}, installed full-throttle thrust lapse
A4A	Airlines for America
A_C	inlet capture area
ADP	aerodynamic design point
AEDT	Aviation Environmental Design Tool
ANP	aircraft noise performance
A_O	reference inlet area
AoA	angle of attack
ASDL	Aerospace System Design Lab
APU	auxiliary power unit
β	multiplier used to capture impacts of both fuel burn and utilization on airline costs
BADA	Base of aircraft data
BFFM	Boeing fuel flow method
BPR	bypass ratio
BTS	Bureau of Transportation Statistics
CAEP	Committee On Aviation Environmental Protection
$C_{all\text{-}other}$	all other costs
CART3D	NASA INVISCID computational fluid dynamics program
CAS	calibrated airspeed
C_{D_O}	profile drag
C_{D_R}	additional drag caused by flaps, ground friction, etc.
C_{fixed}	fixed proportions of airline operating cost
C_{fuel}	fuel cost of airline operating cost
CG	center of gravity
C_L	lift coefficient
CLEEN	continuous lower energy, emissions, and noise
CMPGEN	NASA program for compressor map generation
CO_2	carbon dioxide
d	distance between center of inoperative engine and aircraft longitudinal axis
δ_{amb}	ratio of total pressure
Δt	total segment flight time
ΔT	change in temperature from standard atmospheric temperature
ΔX	distance between CG of vehicle and aerodynamic center of tail
Δz_e	total change in segment energy height
D	drag
DNL	day-night level
DoE	design of experiment
EDS	Environmental Design Space
EEDB	Engine Emissions Databank
eff_{REF}	reference fuel efficiency metric
EI	emissions index
$EINO_X$	NOx emissions index
EIS	entry into service
EPNdB	effective perceived noise in decibels
EPR	engine pressure ratio
EXTR	extraction ratio
ϕ	cooling effectiveness
FAA	Federal Aviation Administration
FAR	Fuel to air ratio
FASST	Framework for Advanced Supersonic Transport
FB_A	fuel penalty to accelerate
$FB_{D\&L}$	fuel penalty to descend from cruising altitude and land

FB_{REF}	reference subsonic fuel burn
FB_{SST}	supersonic fuel burn
$FB_{T\&C}$	fuel penalty to takeoff and climb to cruising altitude
FF	fuel flow
FLEET	Fleet-level Environmental Evaluation Tool
FLOPS	Flight Optimization System
FPR	fan pressure ratio
γ	acquisition multiplier used to scale the proportion of ownership costs
$\gamma_{airline}$	average yield per unit distance for a commercial subsonic airline
GC	great circle
GRA	graduate research assistant
GREAT	Global and Regional Environmental Analysis Tool
HPC	high-pressure compressor
HPCPR	high-pressure-compressor pressure ratio
HPT	high-pressure turbine
ICAO	International Civil Aviation Organization
IDEA	Interactive Dynamic Environmental Analysis
IGV	inlet guide vanes
ISA	international standard atmosphere
K_1	coefficients of parabolic lift-drag polar
K_2	coefficients of parabolic lift-drag polar
KEI	key environmental indicators
JFK	John F. Kennedy International Airport
LAX	Los Angeles International Airport
L/D	lift-to-drag ratio
LE	leading edge
LPC	low-pressure compressor
LPCPR	low-pressure-compressor pressure ratio
LPP MRA	lean pre-mixed pre-vaporized multi radial axial
LPT	low-pressure turbine
LSA	large single aisle
LTA	large twin aisle
LTO	landing and takeoff
M or MN	Mach number
$Mach_{sub}$	subsonic cruise Mach number
$Mach_{super}$	supersonic cruise Mach number
MDP	multi-design point
MFTF	mixed flow turbofan
MTOM	maximum takeoff mass
MTOW	maximum takeoff weight
n	load factor or number of flight segments
n_a	number of accelerations
NASA	National Aeronautics and Space Administration
n_f	number of fuel stops
NOx	nitrogen oxide
NPD	noise power distance
NPR	nozzle pressure ratio
NPSS	Numerical Propulsion System Simulation
nvPM	non-volatile particulate matter
OEI	one engine inoperative
OGV	outlet guide vanes
OpenVSP	open vehicle sketch pad
OPR	overall pressure ratio
PACI	passenger airline cost index
PAX_{REF}	reference subsonic number of passengers
PAX_{SST}	number of passengers of the supersonic aircraft
PCBOOM	NASA PC software for predicting sonic boom on the ground
PDEW	passengers daily each way
PI	principal investigator

PIPSI	Performance Of Installed Propulsion System Interactive
PLdB	sound pressure level in db
P_{t2}	total pressure entering the fan
P_{t21}	total pressure exiting the fan
P_{t3}	total pressure exiting the HPC
P_{t16}	total pressure entering mixer from core side
P_{t56}	total pressure entering the mixer from bypass side
P_S	weight-specific excess power
q	dynamic pressure
ρ	air density
R	rolling resistance force
$R_{C,max}$	maximum cruise range for supersonic vehicles
RJ	regional jet
RQL	rich burn, quick quench, lean burn
S	wing area
SAR	specific air range
SAR_{sub}	specific air range for subsonic aircraft
SAR_{super}	specific air range for supersonic aircraft
S_C	cruise range
SA	single aisle (includes both SSA and LSA classes)
SEL	single event level
SFTF	separate-flow turbofan
SLS	Sea level static
SP	switching percentage
SSA	small single aisle
SST	supersonic transport
STA	small twin aisle
S_{tail}	tail area
θ_{amb}	ratio of total temperature
T	thrust
T_{t3}	compressor exit temperature
T_{t4}	burner exit temperature
T_{t41}	turbine rotor entrance temperature
T_{t41max}	maximum turbine rotor temperature
T_{gas}	gas temperature
T_{metal}	metal temperature
T_{cool}	cooling air temperature
T_{t41SLS}	turbine rotor inlet temperature at sea-level static
t_{cool}	cooled temperature
$t_{C,sub}$	cruise time for subsonic vehicle
$t_{C,sup}$	cruise time for supersonic vehicle
t_{DandL}	time to descent from cruising altitude and land
TE	trailing edge
t_{gas}	gas temperature
TO	takeoff
t_{metal}	metal temperature
TOC	top of climb
t_{REF}	flight times for reference subsonic aircraft
$t_{re\text{-}fuel}$	time delay (90 min) for fuel stops
TSFC	thrust-specific fuel consumption
T_{SL}	thrust at sea level
t_{SST}	flight time for supersonic aircraft
t_{TandC}	time to takeoff and climb to cruising altitude
$t_{total,sub}$	total subsonic flight time
$t_{total,sup}$	total supersonic flight time
U_{REF}	utilization for subsonic aircraft used as reference
U_{SST}	utilization for supersonic aircraft
V	velocity

V_{jet}	nozzle jet velocity
V_C	cruise speed
$V_{C,sub}$	subsonic cruise speed
$V_{C,sup}$	supersonic cruise speed
V_{SR1}	reference stall speed
VT	vertical tail
VTTS	value of travel time savings
WATE	Weight Approximation for Turbine Engines
W_E	empty weight
W_F	fuel weight
W_f	weight of aircraft at the end of a mission segment
W_i	weight of aircraft at the beginning of a mission segment
W_P	payload weight
W_{TO}	takeoff weight
x	percentage of flight over water

Project Introduction

Georgia Tech and Purdue partnered to investigate the effects of supersonic aircraft on the future environmental impacts of aviation. Impacts assessed at the fleet level include direct CO_2 emissions and fuel consumption. The research is conducted as a collaborative effort to leverage capabilities and knowledge available from the multiple entities that make up the ASCENT university partners and advisory committee.

The primary objective of this research project is to support the FAA in modeling and assessing the potential future evolution of the next-generation supersonic aircraft fleet. Research under Task 1 of this project focuses on the development of fleet demand drivers for supersonic transport. This task explores and estimates the potential demand for supersonic travel. Task 2 assesses fleet impact by using the scenarios and vehicle performance metrics developed in Task 1. In Task 3, Georgia Tech will continue to support the development of supersonic aircraft analysis capabilities in AEDT, identify modeling issues, and work with the AEDT development team to identify required modifications. Of note, Task 3 has been combined with Task 5. Task 4 will develop a detailed supersonic aircraft model for the 100-passenger class for three design Mach numbers and will support CAEP supersonic exploratory study. Task 5 involves developing the capability to generate Base of aircraft data (BADA) 4 coefficients to provide additional BADA4 vehicles for AEDT.

Table 1 summarizes the four updated objectives for ASCENT Project 10 with high-level division of responsibilities delineated between Georgia Tech and Purdue.

Table 1. University contributions for year 4.

Objectives		Georgia Tech	Purdue
1	Demand Assessment	Improve airline cost model; improve SST routing tool; improve SST demand estimation Develop assumptions for supersonic scenarios relative to 12 previously developed subsonic focused fleet scenarios	Not applicable
2	Fleet Analysis	Perform fleet analysis with the gradual introduction of SST vehicles into the fleet, including additional SST vehicle types	Develop assumptions for supersonic scenarios relative to 12 previously developed subsonic focused fleet scenarios; perform fleet-level assessments, including additional SST vehicle types; develop FLEET-like tool for supersonic business jet operations; use simple SST sizing to support FLEET development and studies
3	Support CAEP Efforts	FASST vehicle modeling: develop an additional SST class for 100 passengers; perform trade studies to inform CAEP exploratory study	Provide representative supersonic demand scenarios; develop and assess airport noise model to account for supersonic aircraft
4	SST Modeling in AEDT	Develop, implement, and test propulsion and aero coefficient generation algorithms for incorporation within AEDT; identify gaps and challenges in coefficient generation for SSTs; develop an independent method for modeling SST performance by using regression; provide a plan for implementation in AEDT	Not applicable
5	Coordination	Coordinate with entities involved in CAEP supersonic exploratory study Coordinate with clean-sheet supersonic engine design project	Coordinate with entities involved in CAEP MDG/FESG, particularly the SST demand task group; maintain ability to incorporate SST vehicle models that use the engine design from ASCENT project 47 and/or NASA-developed SST models

Georgia Tech is leading the development of a supersonic routing tool to provide basic information about potential time savings and additional costs. This information is then used to develop a demand forecast for commercial supersonic travel.

This work is performed under Objective 1, and the outcome is used to support Objective 2. Under Objective 2, Georgia Tech also produces results for multiple scenarios to assess the fleet-level impacts of supersonic vehicles.
Purdue has applied their FLEET tool under Objective 2, using a subset of the fleet assumptions defined in Objective 1 and preliminary vehicle impact estimates from Objective 4. This activity has demonstrated the capabilities of FLEET for assessing fleet-level environmental impacts as a result of new aircraft technologies and distinct operational scenarios.

Under Objective 4, Georgia Tech is responsible for developing additional aircraft concepts in FASST to support a trade study that will inform the CAEP supersonic exploratory study. For Objective 4, Georgia Tech explores the requirements for modeling supersonic vehicles in AEDT and develops an approach to generate both aerodynamics and propulsion regression coefficients for incorporation into AEDT.

Under Objective 5, Georgia Tech is supporting coordination and meetings with the member entities of the CAEP Modeling and Database Group/Forecasting and Economic Support Group (MDG/FESG), as well as NASA and ASCENT Project 47. This task involves a series of frequent (weekly) meetings as well as ad hoc groups and in-person meetings, or virtual meetings if in-person meetings are not possible.

Milestones

Georgia Tech had four milestones for this year of performance:

1. Fleet assumptions and demand analysis
2. Fleet analysis and demand results
3. FASST SST descriptions and characteristics in Microsoft PowerPoint format

For Purdue, the proposal covering this year of performance included several milestones:

1. Expand the FLEET route network to include global routes
2. Provide updated supersonic demand scenario information in support of CAEP efforts
3. Implement a simultaneous allocation model for FLEET to consider airport capacity and potential airport noise considerations
4. Develop a separate FLEET-like tool to assess supersonic business jet (SSBJ) operations and their subsequent impacts on fleet allocation
5. Assessment of airlines possibly introducing high-passenger-density subsonic aircraft on routes that also have supersonic aircraft service, to provide an estimate of how airlines might respond to high-fare passengers switching to supersonic aircraft (milestone added after additional discussions with our FAA colleagues)

The Purdue team is using its in-house low-fidelity “placeholder” representation of the A10 notional medium SST aircraft to identify the potential supersonic routes based on multiple filters. The team identified 258 potential “supersonic-eligible” routes, comprising 241 nonstop routes and 17 routes with fuel stops. The potential supersonic routes and their associated passenger demand are used in FLEET to determine which of those routes are profitable for the airline and should be served. Early in the project period, the Purdue team used FLEET to indicate which routes had supersonic aircraft service, how many flights per day operated on those routes, and the number of passengers carried on those routes.

The Purdue team has also incorporated the detailed A10 notional medium SST aircraft flown on the detailed supersonic routing path (both provided by Georgia Tech) in FLEET and performed fleet-level assessments for the single “current trends best guess” (CTBG) scenario. The FLEET allocation results indicate routes where supersonic aircraft might be used and might be profitable for the airline, the number of operations performed, along with changes in the utilization of the subsonic aircraft in the fleet. As the Georgia Tech team completes additional supersonic aircraft models with different passenger capacities, ranges, and cruise Mach numbers, the Purdue team will incorporate these aircraft into FLEET.

Because the introduction of SST on certain routes may affect the demand for subsonic travel, the Purdue team developed alternate subsonic aircraft with a higher passenger density (high-passenger-density aircraft) and used them in the FLEET allocation model to provide airlines with an option to use these aircraft to maintain or increase profit on routes using supersonic aircraft. The results show that airlines could maintain or increase existing profit levels by converting existing subsonic aircraft to higher passenger density.

Major Accomplishments

The following major tasks were completed under ASCENT Project 10 during the period of performance:

Fleet-Level Assumptions and Demand Assessment (Task 1)

The Georgia Tech team has developed a parametric airline operating-cost model to allow exploration of the sensitivities of key vehicle, operational, and cost parameters on the required yield that an airline would need to target ticket prices for a potential new supersonic aircraft. This model was integrated with the subsonic forecast to estimate a potential switching percentage on a per-route basis for the estimated cost for an airline to provide commercial SST service. Fuel, a major cost component, was estimated on a per OD pair optimized routing and validated by an aircraft performance model. This procedure resulted in a future-year estimate of the potential demand for SSTs given certain assumptions regarding vehicle performance and cost.

The Purdue team updated FLEET's passenger demand and route network by using historical Bureau of Transportation Statistics (BTS) data for the years 2005–2018, and model-based predictions for the years 2019 and beyond. The team used the previously developed "back of the envelope" representation of the A10 notional medium SST aircraft to identify supersonic-eligible routes including both nonstop routes and routes with one fuel stop. The team also incorporated the detailed A10 notional medium SST aircraft from Georgia Tech into FLEET along with the detailed supersonic routing path (also from Georgia Tech).

Fleet Analysis (Task 2)

One major accomplishment during the period of performance for this task is the capability analyze routes by using the vehicle performance model from Task 4. This allows the detailed evaluation of each route by vehicle capability as well as fuel burn and emissions, which are then fed back to the demand task to refine the demand estimates.

Purdue conducted fleet-level assessments for the updated route network in FLEET by using the detailed A10 notional medium SST aircraft (flown on a detailed supersonic routing path). The outputs included the number of operations and number of passengers served by supersonic aircraft on profitable supersonic-eligible routes, and similar details regarding subsonic aircraft on both supersonic and subsonic routes. In addition, to explore the potential adaptation of an airline that "loses" business-class passengers on its subsonic aircraft, the team developed a high-passenger-density subsonic aircraft model that was used in FLEET to assess the operations of an airline that tries to remain profitable by increasing the number of economy-fare passengers. With these higher-passenger-density aircraft in operation on routes that also have supersonic aircraft service, FLEET can predict the associated impacts on CO_2 emissions.

Because of the continued impact of the COVID-19 pandemic on air travel, the Purdue team updated the historical passenger travel demand to include the reduction in travel in 2019 and 2020, and modified the estimations of future passenger demand to include several recovery scenarios and future demand growth. These adjustments make the FLEET results more relevant and provide a more realistic picture of the potential utilization of supersonic aircraft and associated environmental impacts.

AEDT Supersonic Modeling (Task 3)

The original intent of Task 3 was to develop methods for AEDT to model supersonic transports. At the time of writing of the proposal, AEDT used BADA3 for vehicle modeling; therefore, the proposal focused on BADA3 approaches. Since then, at the time of writing of this report, AEDT is transitioning to BADA4 for new vehicle representation in AEDT, thus rendering the proposed tasks obsolete. On the basis of conversations with FAA technical monitors at Spring of 2019 ASCENT Advisory Board meeting, Georgia Tech has been directed to focus on BADA4 coefficient generation for supersonic transport, which is described in Task 5.

Support of CAEP Supersonic Exploratory Study (Task 4)

Although EDS was originally developed for subsonic vehicles, its structure is still relevant and useful to adapt for the design of supersonic vehicles. One major accomplishment during the previous period of performance was the continual refinement of FASST, specifically the noise assessment for supersonic vehicles, including a variable noise reduction system. Several major modeling accomplishments have been completed during the period of performance by using FASST. The first accomplishment (or more accurately, the first nine accomplishments) is the development of nine closed vehicles ranging from business jets to large SSTs. The second accomplishment is the automation of FASST to generate data for cycle and trajectory optimization. The final accomplishment is the generation of final results of the design Mach trade study for three classes of SSTs.

SST Modeling in AEDT (Task 5)
The Georgia Teach team developed an approach for conducting regression analysis akin to the existing AEDT formulation, and implemented a similar approach for both subsonic and supersonic aircraft. With the current functional form, the accuracy of the regression models has been deemed insufficient. As a result, the team has proposed possible alternative functional forms that are more representative of the underlying physics. The implementation of the proposed approach is under active development and discussion with the FAA.

The Georgia Tech team has developed, and is actively validating and improving, an independent, in-house, physics-informed regression approach that specifically focuses on modeling the propulsive performance and aerodynamic characteristics of supersonic aircraft. The approach has been validated on several GT_SST concepts. The Georgia Tech team has also built a mission simulator to compare the performance of the regressors against truth data across a variety of missions. The mission simulator also provides a framework for implementation of the regression approach within AEDT and has proven to be an effective implementation-related discussion enabler.

Coordination (Task 6)
The Georgia Tech team attended—either in person or virtually after travel became restricted—11 CAEP-related meetings of Working Group 1 (Noise), Working Group 3 (Emissions), and the Modeling and Database Group/Forecasting and Economic Support Group (MDG/FESG) meetings. These meetings included as many as six teleconferences per week, depending on schedules and needs. The Georgia Tech team authored and presented eight papers in these meetings and contributed additional presentations and technical data in support of the CAEP supersonic exploratory study and related progress reports.

The Georgia Tech modeling team provided a medium SST vehicle definition and mission requirement to ASCENT Project 47 Massachusetts Institute of Technology (MIT) researchers for their work on derivative versus clean-sheet propulsion design. In addition, Georgia Tech collaborated with MIT to investigate the impact of a variable noise reduction system on climb-out nitrogen oxide (NO_x) under 3,000 ft for terminal area operations. Finally, Georgia Tech provided detailed results for a Mach 2.2 medium SST in the form of mission-level segment-based results to ASCENT Project 22 and 58. These segment-based results will then be converted to global gridded emissions suitable for global atmospheric analyses,

Task 1 - Demand Assessment

Georgia Institute of Technology

Objective(s)

The primary objective for demand assessment is to first develop a good understanding of the benefits provided by commercial supersonic travel (in terms of time savings) and the increase in ticket cost (proportional to fuel consumption) associated with the faster cruise speed. The model then predicts, for each route, given the corresponding time advantage and ticket cost, the percentage of premium-class passengers expected to switch from existing subsonic service to supersonic offerings.

Demand assessment was conducted on seven SST vehicle models developed at the Aerospace Systems Design Laboratory (ASDL). The SSBJ models were not considered here, because they cater to the business aviation market, and many of the modeling assumptions used for the commercial aviation market no longer hold. The seating capacity and supersonic design cruise Mach number for the seven SST vehicle models are listed in Table 2.

Table 2. ASDL-developed SST vehicle models.

Vehicle Seating Capacity	Supersonic Cruise Mach Number		
55 - Pax	1.8	2.0	2.2
75 - Pax	2.2		
100 - Pax	1.6	1.8	2.0

The flight routing tool optimizes the flight trajectory for each vehicle according to its supersonic and subsonic cruise Mach numbers, as well as the fuel burn characteristics (supersonic specific air range, subsonic specific air range, and transonic acceleration fuel burn). After fuel burn feasibility is verified by flying the optimized flight profile through mission analysis,

viability criteria are then applied to further down-select the final set of routes. This final network differs for each vehicle, because although the demand from premium-class passengers remains constant, different vehicles require different amounts of fuel and provide different time savings.

Research Approach

The demand analysis methodology for commercial SSTs developed by the Georgia Tech team have already been thoroughly described in last year's report. In this year, we have made a slight update to the demand assessment (which changes the estimated switching percentages), because of the use of more accurate trip times obtained from the high-fidelity aircraft mission analysis tool Flight Optimization System (FLOPS). This model capability is described under Task 2.
When performing flight path planning, a more time-optimal setting is first used to calculate all trajectories. If that mission profile cannot be completed by the aircraft because of insufficient fuel capacity, the failed routes are rerun with a more fuel-optimal setting. For a given SST model, all routes that can be flown within the fuel limit are considered feasible. However, whether that route is included in the final network (for that specific SST model) depends on the viability filters.

The criteria for route viability checking are provided below (and are the same as last year's). For a route to be deemed viable, it must meet the following criteria:

1. Time savings relative to the reference subsonic aircraft are more than 20%
2. Time savings relative to the reference subsonic aircraft are more than two hours
3. Number of accelerations are less than four, if no fuel stop is needed
4. Number of accelerations are less than six, if fuel stops are needed
5. Number of flights per day in 2050 are at least one
6. Change in fare per hour saved is less than $1,000

The reasoning for each of these filters is as follows:

- The relative time savings limit is present to enforce a minimum time savings as a percentage of the conventional subsonic trip time, thus allowing for the removal of routes for which the relative time savings might not justify the additional expense for passengers. This filter is similar to but different from the second filter, which is based on a minimum absolute time savings and focuses on removing routes for which the time savings might be less than two hours because passengers may not be able to make use of the small amount of time saved, and therefore their willingness to pay might be low.
- The third and fourth filters are present to eliminate routes that would require too many supersonic accelerations, which, even without detailed performance analysis, would exceed any vehicle performance capability.
- The fifth filter is present to focus on routes that would allow for regular daily service in the highest-demand year in the forecast period. Although more sporadic service (e.g., only several days per week) would also be an option for airlines to offer regular scheduled service, the focus was on the best routes with sufficient demand to enable this service.
- The sixth and final filter is present to limit the maximum fare per hour differential with respect to subsonic service. This filter eliminates routes that meet the other filter criteria but, for various reasons, would require very expensive tickets in order for the service to be offered. The reasons may include excessive circuity (wherein the aircraft, to avoid sonic boom, is forced to fly a long additional distance while still having good relative time savings) or burning large amounts of fuel by maneuvering the aircraft. This final filter removes these routes because passengers willing to pay a very high premium for limited time savings could potentially be served better by business jet service, either subsonic or supersonic.

Results

By analyzing the route data for commercial aviation and forecasting its growth (details were discussed in the previous report), the team identified a set of 1,114 feasible global routes with potential demand from premium-class passengers to support commercial supersonic service in the year 2050. However, routes failing to meet the viability criteria will not be considered in the final network. Several key assumptions are listed below:

1. The forecast year is 2050.
2. The passenger load factor is 70%.
3. Available seat kilometers (ASKs) and revenue passenger kilometers (RPKs) are calculated using great-circle distance and not rerouted distance.

4. The refuel stops last 90 minutes.

Figure 1 shows the relationship between the percentages of feasible routes that are also viable for the seven SST designs, which can be understood as a measure of market-capture capability for different vehicles. It can be seen that the slower Mach numbers (Mach 1.6) have a noticeable impact on the viability of routes, because slower vehicles generally cannot provide as much time savings. Additionally, the larger passenger capacity also adversely affects large SSTs' market capture, because there is a feasibility requirement for the minimum flight frequency, and more passengers are needed to fill a large SST's seats. The 75-Pax Mach 2.2 design performed reasonably well, with very similar market capture compared to that of the Mach 1.8 and the Mach 2.0 variants of the 55-pax SST, although its seating capacity is higher. However, the Mach 2.2 variant of the 55-pax SST still offered the highest market capture. In summary, the general trend is that a higher Mach number and lower seating capacity will lead to greater market capture.

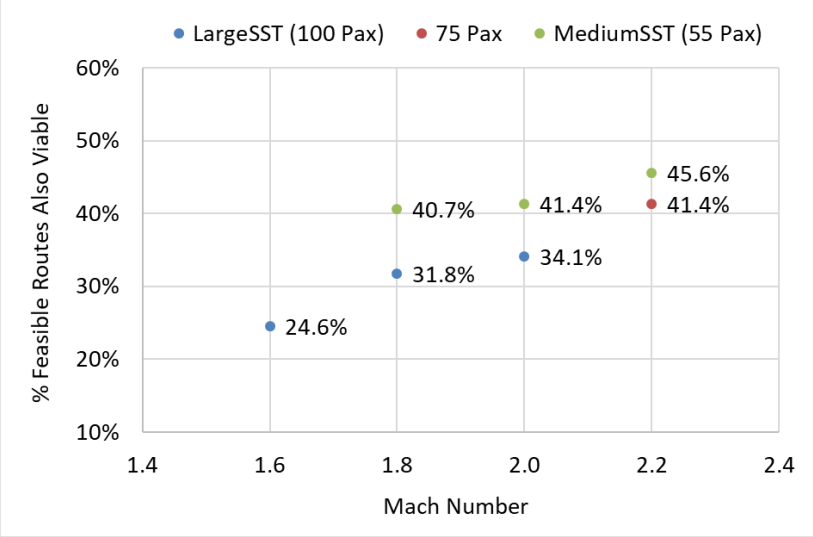

Figure 1. Percentage of feasible routes that are also viable for the seven SST designs.

Figure 2 shows what percentage of viable routes that must be completed with a refuel stop. Because the large SSTs are designed with 5000 nmi of supersonic range, those vehicles are less likely to require refueling. Here, the 75-Pax again shows good performance, considering that it is carrying 20 more passengers but performs on a similar level to that of the Mach 1.8 variant of the medium SST. Moreover, the Mach 2.0 large SST does not require more refuel stops than the Mach 1.8 large SST, because of multiple competing effects, such as the time penalty of refueling against the speed advantage of a higher supersonic cruise Mach number. The overall trend is that SSTs with a higher design Mach number are more likely to require refueling, and the large SST with a supersonic design range of 5000 nmi reduced the need for refueling (approximately 30%–40% reduction) when compared to the medium SST with 4,500 nmi of range.

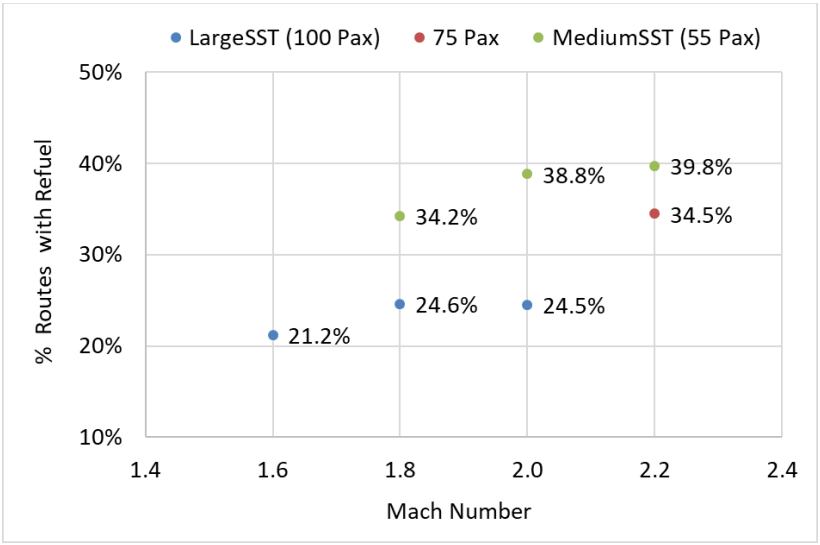

Figure 2. Percentage of viable routes requiring a refuel stop for the seven SST designs.

Table 3 summarizes several key air transportation metrics to aid in understanding the forecasted scale and volume of commercial SST operations for different vehicle designs.

Table 3. Key transportation metrics for the seven SST designs.

SST Type	Mach Number	Sum of Annual Flights (Thousands)	Sum of Annual Passengers (Millions)	Sum of Annual Flight Distance (Billion km)	Sum of Annual Flight Hours (Millions)	Sum of Annual ASK (Billions)	Sum of Annual RPK (Billions)
Large SST (100 Pax)	1.6	211	14.8	1.447	1.226	144.7	101.3
	1.8	281	19.7	1.955	1.600	195.5	136.9
	2.0	308	21.6	2.124	1.666	212.4	148.7
75 -Pax	2.2	469	24.6	3.269	2.536	245.2	171.6
Medium SST (55 Pax)	1.8	616	23.7	4.455	3.748	245.0	171.5
	2.0	631	24.3	4.509	3.662	248.0	173.6
	2.2	690	26.6	4.879	3.837	268.4	187.9

Continuing the same trend observed in market capture, Table 3 shows that smaller, faster designs generally lead to an increased scale of operations (in terms of available seat kilometers). Notably, the 75-Pax (Mach 2.2) design is ranked second in terms of total passengers flown and provides similar total ASKs to the Mach 1.8 medium SST, although the total number of flights and the total flight distance are significantly lower.

Task 2 - GT Fleet Analysis

Georgia Institute of Technology

Objective(s)

The fleet analysis conducted by Georgia Tech mainly focused on the fuel burn, CO_2, and NO_x emissions for the seven aforementioned ASDL-developed SST vehicle models.

Research Approach

The routing algorithm developed by ASDL and described in last year's annual report was updated to accommodate the different performance characteristics of SST vehicle models. Additionally, the flight routing algorithm's output is now merged with aircraft mission analysis output from FLOPS, thus enabling output of the geographic location and the altitude at which the emissions occur. A sample trajectory output is visualized in Figure 3.

In Figure 3, two main types of points are shown on the SST trajectory. The original track points, marked by purple crosses, are the waypoints generated by the flight routing algorithm. The orange dots indicate locations where the discretized FLOPS mission analysis output is available. The mission analysis output is tightly spaced during the acceleration and climb, thus capturing the dynamic behavior of the aircraft during these phases of flight in detail.

The emission species considered and the associated emission indices are listed below:

- NO_x (kg): taken from FLOPS output (details regarding NO_x modeling discussed the Emissions Modeling section of this report)
- CO_2 (kg) based on fuel burn, constant emissions index (EI) of 3.159 kg/kg-fuel (AEDT 3c Tech Manual)
- H_2O (kg) based on fuel burn, constant EI of 1.237 kg/kg-fuel (AEDT 3c Tech Manual)
- Non-volatile particulate matter (nvPM) (g) based on fuel burn, constant EI of 0.05 g/kg-fuel
- Organic particulate matter (PM) (g) based on fuel burn, constant EI of 0.05 g/kg-fuel
- SO_2 (g) and SO_4 (g) based on fuel burn, fuel sulfur concentration (FSC) = 600 mg/kg-fuel
    - E = 2% conversion to SO_4 and estimate the sulfate PM emissions
    - SO_2: FSC/1,000 × [(100% − E)/100%] × fuel × 64/32
    - SO_4: FSC/1,000 × (E/100%) × fuel × 96/32

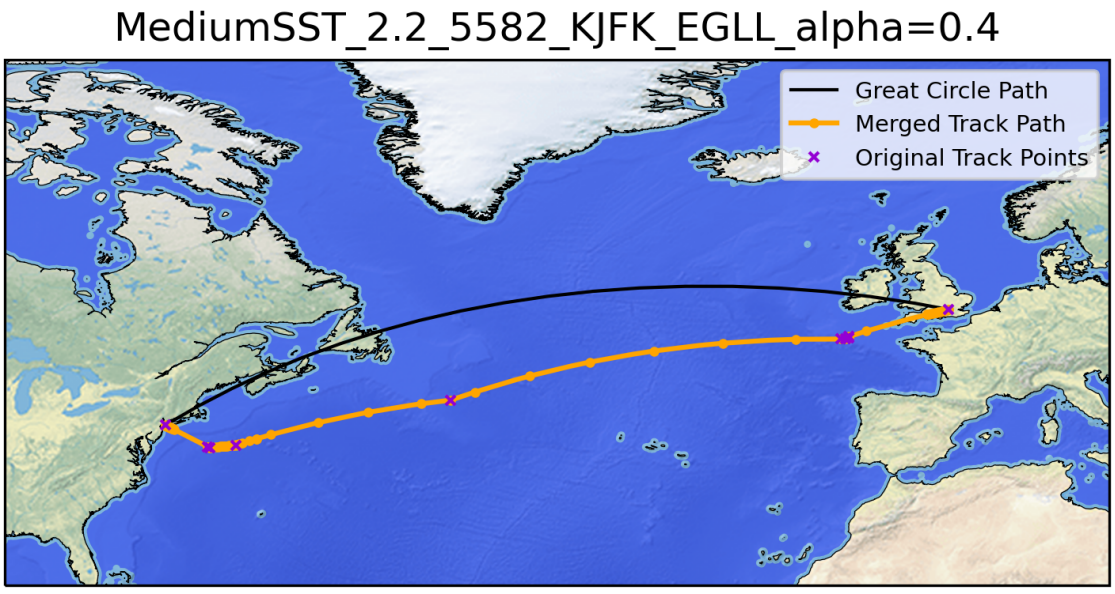

Figure 3. Flight routing tool waypoints and mission analysis data points for KJFK–EGLL.

Results

A jet fuel density of 0.8 kg/L was used. The previously mentioned assumptions regarding passenger load factor and distance measure (great-circle distance [GCD] instead of rerouted distance) still apply.

Table 4. Key emissions metrics for the seven SST designs.

SST Type	Mach Number	Total Annual Fuel Burn (Megatonnes)	Total Annual CO_2 (Megatonnes)	Total Annual NO_x (Kilotonnes)	Fuel Intensity (kg/ASK)	Fuel Efficiency (RPK/L)
Large SST (100 Pax)	1.6	11.52	36.35	150.28	0.080	7.03
	1.8	17.78	56.10	247.60	0.091	6.16
	2.0	22.18	70.01	334.96	0.104	5.36
75-Pax	2.2	33.16	104.65	633.78	0.135	4.14
Medium SST (55 Pax)	1.8	26.80	84.58	391.08	0.109	5.12
	2.0	34.37	108.46	563.81	0.139	4.04
	2.2	43.39	136.95	768.57	0.162	3.46

Of note, the amounts of total fuel consumption, carbon dioxide and nitrogen oxides result from different market capture and scale of operations. To directly compare the fuel efficiency of different vehicles, examining the fuel intensity and fuel efficiency is more reasonable. The general trend is that larger vehicles are more fuel efficient on a per-ASK or per-RPK basis. Additionally, increasing the supersonic design cruise number obviously leads to higher fuel consumption.

Another point that must be emphasized is that the fuel intensity and fuel efficiency values reported here are network-averaged values. If a vehicle were to fly only simple supersonic missions, then the fuel efficiency would be significantly higher. Operating on routes requiring a substantial portion of subsonic overland flight or additional transonic accelerations would have a big impact on the overall network-averaged fuel efficiency.

The detailed results for the Mach 2.2 medium SST were saved as mission-level segment-based results, which were shared with Ascent Project 22 and 58. These segment-based results will be converted to global gridded emissions, which are suitable for global atmospheric analyses,

Task 2 - Purdue Fleet Analysis

Purdue University

Objectives

The Purdue team conducted four sub-tasks as a part of this task. For this year, the Purdue team used a U.S.-touching route network to study the impact of supersonic aircraft operations on subsonic aircraft operations, predict the changes in future supersonic travel demand due to the COVID-19 pandemic, and develop a simultaneous aircraft allocation approach for supersonic and subsonic aircraft. Additionally, the team extended the U.S.-touching route network in FLEET to a worldwide route network; the task is still underway and will be completed next year.

Supersonic Demand and Route Characterization

The ticket fares associated with supersonic aircraft travel will be higher than those of current economy-class tickets, which indicates that there will only be a small segment of passengers who would be willing to pay for the supersonic aircraft service. In addition, the supersonic aircraft characteristics (particularly the restriction from overland supersonic operations and the range of the aircraft) will limit the routes on which the aircraft could operate. Hence, the number of passengers on a given route who would be willing to pay for and use supersonic aircraft must be determined, and the potential routes with supersonic aircraft operations must be identified.

Supersonic Passenger Demand

The Purdue team assumed that the potential supersonic passengers are the current passengers paying fares at business class or above. In FLEET, the travel demand is split such that supersonic demand (business class or above) is a fixed percentage (5%) of the total travel demand on each route, and the remaining demand is from passengers only willing to pay subsonic fares.

Potential Supersonic Routes (U.S.-Touching Route Network)

In this report, the team considered potential airport pairs that are nonstop (direct) or include a fuel stop (indirect) as potential supersonic routes. The potential supersonic routes were identified from FLEET's existing U.S.-touching route network of 1,974 routes in year 2018 (the route network in the year 2018 is the most recent route network in FLEET, and the network stays constant for all years beyond 2018), by using a set of route filters based on the performance characteristics of a placeholder supersonic aircraft (different from the high-resolution supersonic aircraft provided by Georgia Tech). The potential supersonic routes were filtered according to the placeholder supersonic aircraft's maximum design range (thus differentiating between routes that require a fuel stop and those that do not), the aircraft's maximum range capability for different percentages of supersonic and subsonic flight segments, and the block time savings incurred by flying supersonic aircraft rather than subsonic aircraft. To calculate the minimum time flight path for a supersonic route, the Purdue team used a very simple supersonic route path adjustment strategy that outputs the block time, percentage of flight path over water, updated departure heading for the route, and minimum time route distance.

Nonstop Routes (U.S.-Touching Route Network)

The route filters for nonstop routes led to the identification of 241 nonstop potential supersonic routes in the FLEET network. Of these 241 routes, with our simplistic route path adjustment, 191 routes have greater than or equal to 75% of flight overwater, 35 routes have flight segments between 50% and 75% over water, and the remaining 32 routes have flight segments less than 50% over water.

Routes with Fuel Stops (U.S.-Touching Route Network)

Some intercontinental routes exceed the un-refueled range of the supersonic aircraft with sufficiently high passenger demand to suggest the potential for profitable supersonic operations. These routes show total time savings even with the increase in distance flown, and the time required to land, refuel, and take off again, with the assumption that the fuel stops are just technical stops (i.e., there is no boarding of new passengers from the fuel-stop airport into the flight or debarkation of any existing passengers from the flight). Only airports currently in the FLEET network were considered for potential fuel stops. There are two trans-Pacific potential fuel-stop airports (Honolulu, Hawaii (HNL) and Anchorage, Alaska (ANC); and five trans-Atlantic potential fuel-stop airports (Shannon, Ireland (SNN); Keflavik, Iceland (KEF); Oslo, Norway (OSL); Dublin, Ireland (DUB); and San Juan, Puerto Rico (SJU). The fuel stop adds 60 minutes to the block time of the supersonic aircraft flying on the with-fuel-stop route (this is based on the team's judgement, including the time for final descent, landing, taxi, refueling, taxi, takeoff, and climb out).

U.S.-Touching Supersonic-Eligible Route Network in FLEET

The supersonic-eligible route network in FLEET consists of a total of 258 potential supersonic routes, 241 of which are nonstop and 17 of which include a fuel stop. Figure 4 depicts the potential supersonic route network for FLEET on a world map. The route paths for the 258 potential routes plotted in this figure are based on airport minimum time connections and are only illustrative.

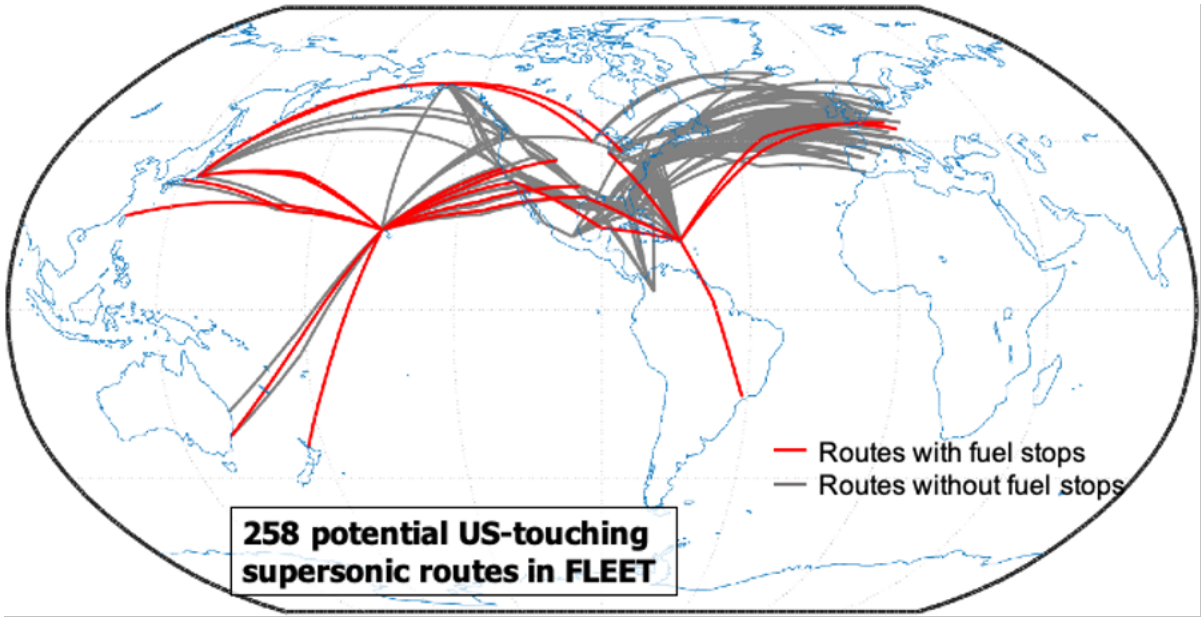

Figure 4. U.S.-touching supersonic-eligible route network in FLEET (airport minimum time connections, not the exact route path flown, are shown).

Impact of Supersonic Aircraft Operations on Subsonic Operations

The Purdue team predicted how commercial supersonic aircraft operations as part of an airline's fleet might alter subsonic operations across the network in an effort to maintain profitability. The current work was based on the assumption that the potential supersonic passengers are the current subsonic passengers who pay "business class or above" fares. Considering current ticket pricing on many over-ocean routes where future supersonic aircraft would operate, the ticket prices for business class or above tend to subsidize the economy-class ticket prices. When the airline loses a portion of its subsonic high-revenue passengers to supersonic service, the airline might want to alter the economy ticket prices to compensate for the loss of business-class seats and associated fares. As these passengers shift from subsonic business class or above to supersonic service, airlines may need to change how they operate their subsonic fleet of aircraft to maintain or increase profit. One possible way to do so is to reconfigure the current subsonic aircraft by removing premium seats and replacing them with a higher number of "economy" seats to limit the impact of the loss of revenue, from business class or above fares, on profits. With changes to the subsonic aircraft seating configuration, the team considered four possibilities for how airlines might adjust ticket pricing to continue to make similar (or even greater) profit. This work simulated those four different ticket pricing possibilities and estimated their potential future effects on airline profits and emissions when high-passenger-density aircraft are introduced alongside supersonic aircraft.

<u>High-Passenger-Density Subsonic Aircraft Modeling Approach</u>

This work considered high-passenger-density versions for the "new-in-class" and "future-in-class" generations of class 3 (SA – single aisle), class 4 (STA – small twin aisle), class 5 (LTA – large twin aisle), and class 6 (VLA – very large aircraft) subsonic aircraft in FLEET. As mentioned above, the concept for modeling a higher-passenger-density subsonic aircraft is that some of the larger premium (business class or first class) seats are removed and replaced with a larger number of smaller economy-class seats. A study of recent multi-class cabin configurations—which vary by aircraft among airlines, and even among sub-models of aircraft within a given airline—has determined the ratio of "small" seats added to "large" seats removed. For modeling in FLEET, the team adjusted the operating load factor of the subsonic aircraft operating on routes where supersonic service is also available, to mimic operating an aircraft with more seats in a higher-passenger-density cabin. The major assumption was that the aircraft operating empty weight remains constant even when a higher number of seats is present in the aircraft; therefore, the weight of the seats in business class or above removed from the aircraft equals the weight of the economy-class seats added to the aircraft. This assumption allowed the team to reuse existing subsonic aircraft FLOPS models. The team acknowledges that a higher-fidelity approach to model the high-density version of the existing subsonic aircraft would be to modify the existing aircraft models in FLOPS by using a different operating empty weight (with the

difference in the operating empty weight resulting from the replacement of some large seats with a larger number of small seats); however, the team believes that the simplistic modeling approach described here is sufficient to demonstrate the fleet-level impacts of introducing high-density subsonic aircraft on routes with supersonic aircraft operations.

High-Passenger-Density Subsonic Aircraft Seat Configuration

This work was based on the assumption that 50% of the passengers in business class or above are the potential supersonic passengers. This assumption is based on observations that approximately 10% of the seats in multi-class cabin aircraft are premium seats, and approximately half the passengers who sit in premium seats pay the premium fare (whereas the remainder use some form of upgrade or reward). The team configured the high-passenger-density subsonic aircraft by replacing half the seats in business class or above (large) with twice the number of economy-class (small) seats. Figure 5 compares the seat areas of various seat configurations for long-haul flights across different airlines, where the seat area is estimated as the product of the seat pitch and seat width. On average, the first-class, business-class, and premium-economy seat areas are 3.2 times, 2.3 times, and 1.3 times larger than the basic economy-class seat areas, respectively, according to data obtained from SeatGuru (by Tripadvisor) in March 2019.

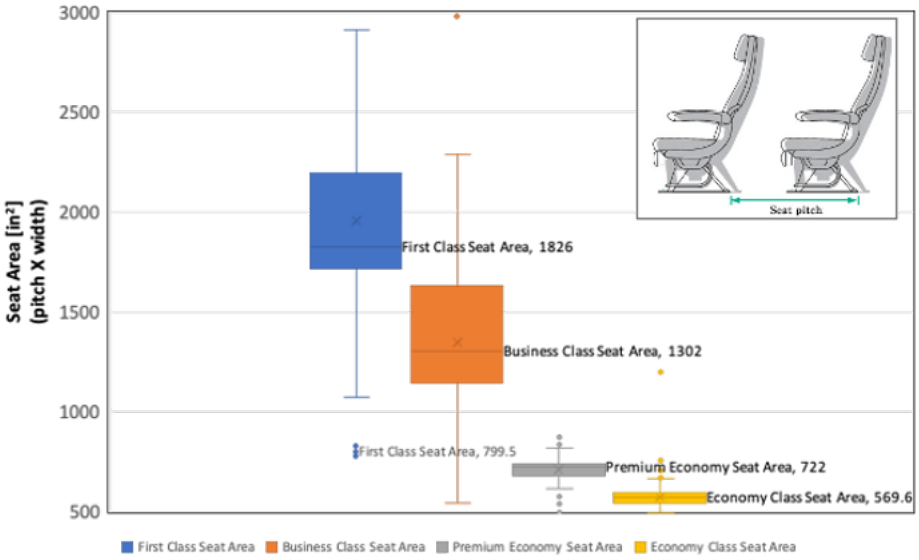

Figure 5. Seat area comparison for aircraft seat configurations for long-haul flights across different airlines.

On the basis of these findings, the team assumed that one large seat is approximately equal to two small seats. For example, a class 3 aircraft in FLEET has 12 large seats and 165 small seats, with a total of 177 seats in its standard configuration. Using the aforementioned approach, the high-passenger-density version of a class 3 aircraft would have (12 – 12/2) = 6 large seats and (165 + 2 × 12/2) = 177 small seats, with a total of 183 seats. Table 5 shows the seat configuration for all four classes of high-passenger-density aircraft. Prior to the study described here, all the subsonic aircraft (referred to as standard configuration in this paper) in FLEET operated at a load factor of 80% for the allocation problem and did not require differentiation between classes of seats. The values for the high passenger density at an 80% load factor provide an estimate of how the seats would be filled in each cabin class.

Table 5. Seat configuration for all four classes of high-passenger-density aircraft (*seat capacity: economy class [small seats] + business class or above [large seats]).

	Single-Aisle, SA (Class 3)		Small Twin-Aisle, STA (Class 4)		Large Twin-Aisle, LTA (Class 5)		Very Large, VLA (Class 6)	
Configuration	Standard	High-pax-density	Standard	High-pax-density	Standard	High-pax-density	Standard	High-pax-density
Max Seat Capacity [pax]	177 (165 + 12)*	**183 (177 + 6)***	261 (237 + 24)*	**273 (261 + 12)***	305 (227 + 78)*	**344 (305 + 39)***	417 (309 + 108)*	**471 (417 + 54)***
Pax capacity w/ 80% load factor	142	**147 (142 + 5)***	209	**219 (209 + 10)***	245	**275 (244 + 31)***	335	**377 (334 + 43)***

Maximum Passenger Capacity of Subsonic Aircraft

For models of the new-in-class and future-in-class aircraft, the smaller class 3 (single aisle) and class 4 (small twin aisle) high-passenger-density aircraft cannot fly most of the popular trans-Atlantic and trans-Pacific routes at an 80% load factor, whereas their counterparts with standard configuration can. The reason for this difference is the highly efficient nature of these notional future subsonic aircraft models. Figure 6 shows modified payload-range diagrams for class 3 and class 4 aircraft in standard configuration, that uses load factor rather than payload on the vertical axis. The new-in-class, class 3 aircraft has an intersection of the maximum takeoff weight limit and the fuel volume limit at a load factor of approximately 90%, whereas that of the future-in-class aircraft is at approximately 50%. For class 4 aircraft, this intersection for both the new- and future-in-class is at approximately 90%. The new-in-class, class 3 aircraft could only complete routes approximately 3,400 nmi or less at an 80% load factor in standard configuration, and the future-in-class aircraft could complete routes of approximately 4,400 nmi or less. Similarly, the class 4 aircraft at an 80% load factor could complete routes of only approximately 6,400 nmi or less for both the new-in-class and future-in-class versions in standard configuration. The aircraft with high-passenger-density configuration would be at a lower load factor for the same payload weight, which would make the maximum range for these aircraft even narrower at an 80% load factor. These findings suggest the need to consider the maximum number of passengers that could be carried by any of the class 3–6 aircraft on the trans-oceanic routes, because those trans-oceanic routes are where the supersonic aircraft might also operate.

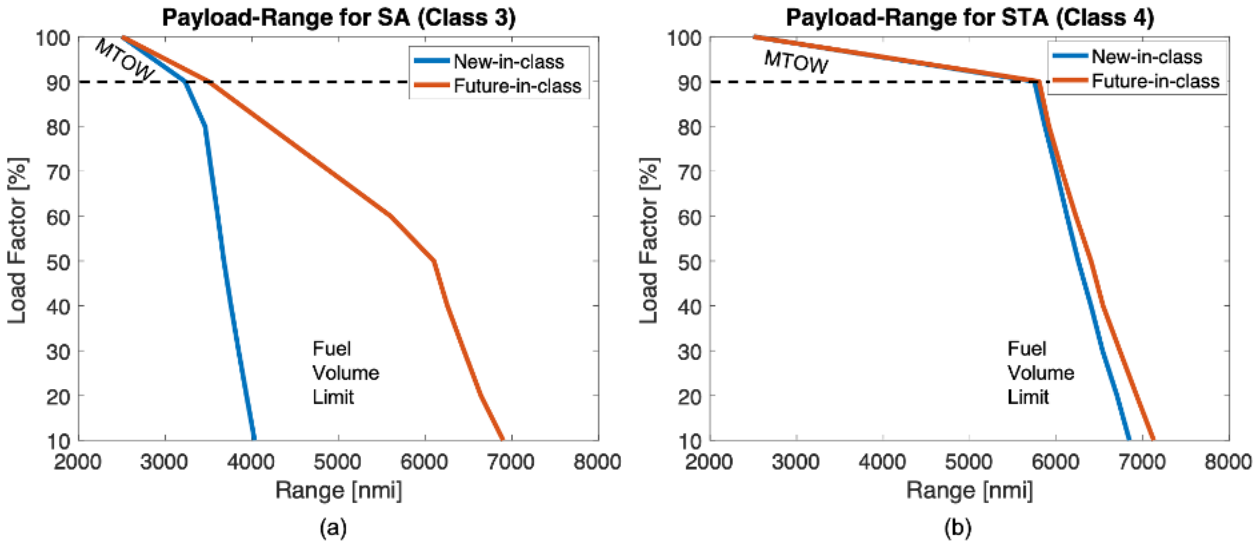

Figure 6. Payload-range charts for (a) class 3 subsonic aircraft, and (b) class 4 subsonic aircraft in FLEET.

The team reran the subsonic aircraft FLOPS models to determine the maximum passenger capacity for a given range. Figure 7 shows how the maximum load factor for the standard configuration varies with route length. As expected, the maximum load factor decreases as the route length increases. Because the high-passenger-density subsonic aircraft are introduced only on routes that see supersonic aircraft operations, the authors only considered the route lengths of the 258 supersonic-

eligible routes in this effort. Consequently, all the high-passenger-density subsonic aircraft (new-in-class and future-in-class aircraft for classes 3, 4, 5, and 6 to have a unique maximum passenger capacity for each of the 258 supersonic-eligible routes.

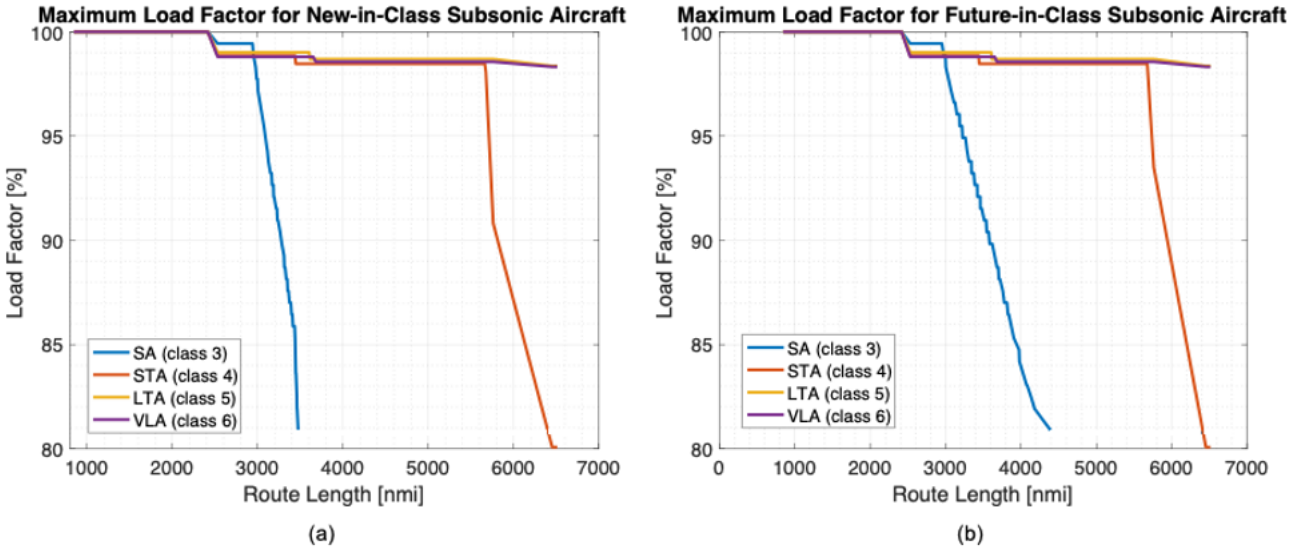

Figure 7. Maximum load factor for the standard configurations, as a function of route length for (a) new-in-class subsonic aircraft and (b) future-in-class subsonic aircraft, in FLEET.

Implementation of High-Passenger-Density Subsonic Aircraft in FLEET

To determine the number of subsonic seats available in FLEET for a specific subsonic aircraft class on a route with supersonic service, the team chose the lower value of the passenger capacity corresponding to an 80% load factor of the high-passenger-density configuration or the maximum number of passengers that the standard configuration aircraft could carry on the route. For example, if the number of seats available using the high-passenger-density configuration class 3 aircraft with an 80% load factor is 147 passengers on a hypothetical route A–B, and the maximum capacity for a class 3 standard configuration aircraft is 135 passengers on that route, then the high-passenger-density aircraft could only carry 135 passengers. Therefore, the payload weight limitation may restrict the high-passenger-density configuration aircraft to carry the same number of passengers as in the standard configuration, and the airline would see no revenue benefit to using this class of aircraft on this route.

To introduce these high-passenger-density subsonic aircraft into FLEET, the team generated the FLEET relevant aircraft performance and cost coefficients for all the high-passenger-density subsonic aircraft (similar to the standard versions of these aircraft) by using the updated load factor for each of the 258 routes. The updated load factor is calculated as the percentage ratio of the available seats for the high-passenger-density aircraft to the maximum number of seats available in the standard configuration.

For a route where the 80% load factor on the high-passenger-density configuration is not restricted by the payload-range diagram, the updated load factor will be greater than 80%. For instance, a high-passenger-density class 5 aircraft at an 80% load factor will carry 275 passengers; the FLEET updated load factor will be (275/305) × 100 = 90%. For the above example of the high-passenger-density class 3 aircraft with a payload-range limitation, the FLEET updated load factor on that route will be (135/177) × 100 = 76%.

Table 6 shows sample aircraft performance and cost coefficients for a new-in-class, class 3 aircraft on the John F. Kennedy International Airport (JFK)–London Heathrow International Airport (LHR) route; this route of approximately 3,000 nmi is not payload-range limited for this aircraft in either the standard or high-passenger-density configuration. As expected, the high-passenger-density configuration of subsonic aircraft burns more fuel (because of the higher payload weight) and has higher crew and indirect operating costs (because of the relationship to the number of passengers carried).

Table 6. Sample aircraft performance and cost coefficients for new-in-class, class 3 aircraft on the JFK–LHR route.

Coefficients for new-in-class 3 aircraft on JFK – LHR route	Standard	High-Pax-Density	Increment
Block time [hrs.]	7.2	7.2	**0.0 %**
Fuel burn [lbs.]	31,663	32,825	**+3.7 %**
Crew cost [$]	5,848	5,872	**+0.4 %**
Indirect operating cost [$]	19,966	20,338	**+1.9 %**
Servicing cost [$]	1,318	1,318	**0.0 %**
Maintenance cost [$]	2,030	2,030	**0.0 %**

The team currently uses a sequential allocation approach for allocating the supersonic and subsonic passengers in FLEET. In the sequential allocation approach, the allocation of the airline's supersonic aircraft occurs before the allocation of the airline's subsonic aircraft. Because the supersonic aircraft are allocated first, introducing high-density subsonic aircraft only on routes with supersonic aircraft allocation is straightforward. Hence, the team was able to implement the high-passenger-density subsonic aircraft in FLEET without modifying the allocation problem itself.

High-Passenger-Density Subsonic Aircraft Ticket Pricing

With the "densification" of the subsonic aircraft, 50% of the passengers in business class or above would switch from subsonic to supersonic aircraft, which could cause the airlines to adjust ticket pricing for the high-passenger-density aircraft operations to continue to make similar (or even higher) profits. The team considered four ticket pricing possibilities for the high-passenger-density aircraft; each possibility affects the profitability of a given aircraft type on a given trip, and the aircraft allocation changes to maximize profit.

Currently, FLEET uses an average ticket price for all its simulations. To capture the ticket price possibilities when the seating configuration changes, business and economy ticket prices must be considered separately. To break down the average ticket price in FLEET into business-class and economy-class prices, the team assumed that a business-class ticket price costs twice as much as the economy-class ticket price. Using the seat configuration information for the existing subsonic aircraft in FLEET and the ratio of business-class to economy-class ticket prices, the team determined the business and economy ticket prices for each aircraft type on every route in FLEET (using Equations 1 and 2). Equations 3 and 4 depict the relationship between average ticket price, ticket price margin, and trip margin in the existing subsonic ticket pricing model in FLEET.

Equation 1 $$\mathbf{avg_{ticketprice}} = \frac{\mathbf{ticketprice_{business} * seats_{business} + ticketprice_{economy} * seats_{economy}}}{\mathbf{seats_{total}}}$$

Equation 2 $$\mathbf{ticketprice_{business}} = \mathbf{2} \times \mathbf{ticketprice_{economy}}$$

Equation 3 $$\mathbf{avg_{ticketprice}} = \frac{\mathbf{cost_{trip}}}{\mathbf{seats_{total}}} + \mathbf{ticketprice_{margin}}$$

Equation 4 $$\mathbf{trip_{margin}} = \mathbf{avg_{ticketprice}} \times \mathbf{seats_{total}} - \mathbf{cost_{trip}}$$

There are four possible high-passenger-density ticket price modeling approaches in FLEET:

Case 1: Constant Average Ticket Price

In this case, the average ticket price for the high-passenger-density aircraft is set to be the same as the average ticket price for the standard subsonic aircraft. The higher number of seats with the high-passenger-density version causes both the business and economy ticket prices to increase, thus leading to a higher ticket price margin and trip margin (Table 7). The airline is expected to earn a higher profit when this approach is implemented in FLEET.

Case 2: Constant Ticket Price (Business and Economy)
In this case, the business and economy ticket prices for the high-passenger-density aircraft are set to be equal to the business and economy ticket prices for the standard subsonic aircraft. Because of the increased number of seats in the high-passenger-density version, the ticket price margin and trip margin increase slightly (but remain lower than those in case 1), while the average ticket price decreases (Table 7). The airline is expected to earn a slightly higher profit when this approach is implemented in FLEET (but lower than that in case 1).

Case 3: Constant Trip Margin
In this case, the trip margin for the high-passenger-density aircraft is set to be the same as the trip margin for the standard subsonic aircraft. With the constant trip margin spread out over more seats for the high-passenger-density version, the business and economy ticket prices are slightly lower, along with the average ticket price. However, the ticket price margin remains higher than that the standard subsonic aircraft case (Table 7). The airline is expected to earn a slightly lower profit when this approach is implemented in FLEET, because the passengers end up paying less for the business-class and economy-class tickets.

Case 4: Constant Ticket Price Margin
In this case, the ticket price margin for the high-passenger-density aircraft is set to be the same as the ticket price margin for the standard subsonic aircraft. The economy-class tickets have a much lower margin than business-class tickets. With a smaller number of business-class seats available in the high-passenger-density version, the trip margin, prices of business and economy tickets, and average ticket price decrease (Table 7). This case indicates that the airline is unable to compensate for the loss of business-class seats, and the airline's profit is expected to be lowest.

Table 7 summarizes the four possible airline actions with respect to ticket pricing for high-passenger-density subsonic aircraft and their required FLEET inputs. Table 8 considers the JFK–LHR route as an example to provide ticket price values for a new-in-class, class 3 subsonic aircraft; the numbers in this example help demonstrate the actual changes in trip and ticket price margins as different ticket pricing strategies are adopted.

Table 7. Possible airline actions with respect to ticket pricing for high-passenger-density subsonic aircraft and their required FLEET inputs.

Possible airline actions	Inputs				
	Average Ticket Price	Economy Ticket Price	Business Ticket Price	Trip Margin	Ticket Price Margin
No high-pax-density	–	–	–	–	–
Case 1: Constant average ticket price	–	↑	↑	↑	↑
Case 2: Constant ticket price	↓	–	–	↑ (slightly)	↑ (slightly)
Case 3: Constant trip margin	↓	↓ (slightly)	↓ (slightly)	–	↑ (slightly)
Case 4: Constant ticket price margin	↓	↓	↓	↓	–

Impact of COVID-19 on Passenger Demand and Fleet-Level Assessments
The novel coronavirus (COVID-19) pandemic has caused severe disruptions in the aviation industry by inducing one of the sharpest declines in air travel demand in aviation history. The full-year global passenger traffic results from both the International Air Transport Association (IATA) and the International Civil Aviation Organization (ICAO) indicate that 2020 was the worst year in history for air travel demand (IATA Press Release, 2021; ICAO, 2021). According to IATA, the global passenger demand in 2020 fell by 65.9% with respect to the pre-COVID-19 levels of 2019 (IATA Press Release, 2021; IATA Economic Reports, 2020). ICAO has provided similar estimates for the decrease in travel demand in 2020 (ICAO, 2021), with an overall reduction of 50% of seats offered by airlines, which translates to approximately 2,699 million fewer passengers

worldwide compared to the pre-COVID-19 levels (2019). In 2021, IATA estimates indicate that the demand may recover to between 38% to 52% of pre-COVID-19 levels (2019), and complete recovery to 2019 levels may be possible by 2023 or 2024 (IATA Press Release No: 33, 2021; Pearce, 2021), depending on the continuation of travel restrictions imposed worldwide because of the spread of more contagious COVID-19 variants.

Table 8. Ticket pricing example for new-in-class, class 3 aircraft on the JFK–LHR route (*based on the assumption that a business-class ticket costs twice as much as an economy ticket).

JFK-LHR route / Class 3 aircraft	Possible airline actions	Average Ticket Price [$]	Economy Ticket Price [$]*	Business Ticket Price [$]*	Trip Margin [$]	Economy Ticket Margin [$]*	Business Ticket Margin [$]*
Standard (132 + 10)	Existing	342.8	320.2	640.4	1759.3	-10.2	310.1
High-pax-density (142 + 5)	Case 1: Constant average ticket price	342.8	331.5	663.0	3587.6	13.1	344.6
	Case 2: Constant ticket price	331.1	320.2	640.4	1873.8	1.9	322.1
	Case 3: Constant trip margin	330.3	319.5	638.9	1759.3	1.1	320.6
	Case 4: Constant ticket price margin	319.1	308.2	628.4	107.3	-10.2	310.1

Future Demand Scenarios

For this report, the Purdue team considered two different scenarios for airline operations recovery after the current decrease in operations due to COVID-19-related travel restrictions imposed worldwide. The team also considered three GDP growth scenarios from the year of passenger demand recovery to pre-COVID-19 levels (2019) to the year 2030; the GDP growth rate directly impacts the inherent passenger demand in FLEET. Thus, a total of six scenarios for future demand projections are examined. The total passenger demand in 2020 for all six scenarios is set to 34% of the passenger demand levels in 2019, signifying a 66% decrease in total passenger demand (IATA Press Release No: 33, 2021).

The first three scenarios consider that the passenger demand returns to pre-COVID-19 levels (2019) by the year 2023. The total passenger demand is set to recover to 52% of pre-COVID-19 levels by 2021, 88% of pre-COVID-19 levels by 2022, and 100% of pre-COVID-19 levels by 2023 (IATA Press Release No: 33, 2021). These three scenarios are distinguished by the inherent passenger demand growth rate, which is based on the GDP growth rate assumed in the FLEET simulation. The first scenario, 2023 recovery, assumes that the passenger demand continues to grow based on the GDP growth rate in FLEET beyond 2023. This scenario does not consider the long-term economic impacts of the COVID-19 pandemic and assumes that the GDP will continue to grow in a manner unaffected by the pandemic after 2023. The second scenario, 2023 recovery + GDP slowdown to 75% until 2030, considers that the passenger demand grows corresponding to 75% of the GDP growth assumptions in FLEET from the years 2023–2030. This scenario considers the long-term economic impacts of the COVID-19 pandemic and assumes that the GDP will grow at a slower rate until the year 2030. The third scenario, 2023 recovery + GDP inflation to 125% until 2030, assumes that the passenger demand grows at 125% of the inherent demand and GDP growth assumptions in FLEET from the years 2023–2030. This scenario assumes that the GDP will rebound and become stronger in the longer term and grow at a faster rate until the year 2030.

The remaining three scenarios consider that the passenger demand returns to pre-COVID-19 levels (2019) by the year 2024 (1 year later than in the previous three scenarios). The total passenger demand is set to recover to 38% of pre-COVID-19 levels by 2021, considering the possibility that the severe travel restrictions in response to new COVID-19 variants might persist (IATA Press Release, 2021). The passenger demand is then assumed to recover to 50% of pre-COVID-19 levels by 2022, 75% of pre-COVID-19 levels by 2023, and pre-COVID-19 levels by 2024. Similarly to the previous three scenarios, the fourth scenario, 2024 recovery, assumes that the GDP will continue to grow in a manner unaffected by the pandemic after 2024; the fifth scenario, 2024 recovery + GDP slowdown to 75% until 2030, assumes that the passenger demand will grow corresponding to 75% of the GDP growth assumptions in FLEET until the year 2030; and the sixth scenario, 2024 recovery +

GDP inflation to 125% until 2030, assumes that the passenger demand will grow at 125% of the GDP growth assumptions in FLEET until the year 2030.

Table 9 summarizes the future demand scenarios considered; passenger demand for different years is listed as a percentage of pre-COVID-19 levels (2019), and the GDP growth rate is listed as a percentage of the "nominal" GDP growth rate in FLEET (Mavris et al., 2017).

Table 9. Future demand scenarios.

Scenario #	Description	Passenger Demand (% of pre-COVID-19 levels)					GDP Growth Rate (as % of 'Nominal')
		2020	2021	2022	2023	2024	
1	2023 recovery	34%	52%	88%	100%	--	No change
2	2023 recovery + GDP slowdown to 75% until 2030	34%	52%	88%	100%	--	75% (- 25%)
3	2023 recovery + GDP inflation to 125% until 2030	34%	52%	88%	100%	--	125% (+25%)
4	2024 recovery	34%	38%	50%	75%	100%	No change
5	2024 recovery + GDP slowdown to 75% until 2030	34%	38%	50%	75%	100%	75% (- 25%)
6	2024 recovery + GDP inflation to 125% until 2030	34%	38%	50%	75%	100%	125% (+25%)

Extending the Airline Network to a Global Network

As part of the efforts in previous years, FLEET adopts a semi-dynamic route network that changes according to Bureau of Transportation Statistics (BTS) (Airline Origin and Destination Survey – DB1B) data from 2005 to 2018, followed by a static route network from the year 2019 onward. The final route network consists of 1,974 different routes defined by a subset of the list of 257 airports from the Worldwide Logistics Management Institute Network (WWLMINET). The motivation for using 2005 as the baseline year for FLEET came from numerous stated CO_2 emissions goals that also use 2005 as their baseline year. With the BTS-reported data providing the basis for most of the initial airline fleet and yearly route demand up to 2018, FLEET is limited to modeling U.S.-touching routes (those with at least one airport of the origin-destination pair in the United States) and only flights operated by U.S. flag carrier airlines.

To extend FLEET's capability to provide supersonic and subsonic aircraft allocation data on global international routes (in addition to those already present in the FLEET network), the Purdue team is updating FLEET's U.S.-touching route network to a worldwide route network. This task is currently underway and will be fully completed as part of the next year's work.

To model the behavior of an aggregate global airline, the Purdue team purchased global fleet demand data from the Official Aviation Guide (OAG) Traffic Analyzer. The data were extracted from the OAG Traffic Analyzer for the years 2011–2020; OAG did not have relevant global fleet demand data available for any year earlier than 2011. On the basis of global data availability, the team decided to change the initial year of the FLEET simulation from 2005 to 2011, and update the initial network, passenger demand, and fleet composition accordingly.

Passenger Demand

The team accessed the raw passenger demand data from OAG for the years 2011–2020. The raw data contained information irrelevant to FLEET and therefore required filtering before being used to generate the route network in FLEET. The application of the filters numbered from 0 to 5 in Table 10 trims the raw data from OAG to relevant data that can be used as an input for further processing in FLEET. After these filters are applied to the raw data in the order listed in Table 10, the final demand data contain information on the number of passengers per year on directional routes by all global carriers combined. For example, to capture regularly scheduled airline traffic, the team considered only routes with a passenger demand of at least 7,800 passengers per year (i.e., 150 passengers per flight, one flight per week, and 52 weeks per year) among the 257

WWLMINET airports (257 most popular airports around the world according to Institute Network Queuing Model (WWLMINET). The resulting filtered OAG data have 364,672 segments (routes) over the 10-year time window from 2011 to 2020.

Table 10. List of filters for extracting and processing OAG data.

ID	Step	Purpose	Data
0	Initial worldwide routes and passenger demand data for 2011using OAG Traffic Analyzer		Yearly records of numbers of passengers who traveled on directional routes by all carriers
1	All origin and destination airports are in the WWLMINET network of 257 airports	Keep entries for routes with origin and destination within only the WWLMINET 257 airport network	Same as above
2	Filter out routes with the same origin and destination	Remove entries with same origin and destination for directional routes only	Same as above
3	Filter out all routes that have less than 7,800 passenger counts	Keep only entries for routes with regular operations (at least 150 passengers per flight for at least one flight per week or 52 flights per year, performed on directional routes)	Yearly record numbers of passengers who traveled on directional routes with regular operations via all carriers
4	Turn each subset into a 257 × 257 matrix	Prepare for input to FLEET	Same as above, in matrix form
5	Process in FLEET	Filter for minimum passengers per day, minimum runway length, etc. Convert yearly demand to daily demand	Daily demand on bidirectional routes by one large “aggregate” airline representing all carriers

To conduct a sanity test of the filtered OAG data, the team compared the U.S.-touching demand from the BTS data with the OAG demand on the existing U.S.-touching route network in FLEET from 2011 to 2020. Figure 8 shows a coefficient of determination for the OAG and BTS data of 0.9918, indicating that the passenger demand for at least the U.S.-touching route network is highly similar between BTS and OAG data. This finding allowed the team to verify that the filtered OAG data make sense.

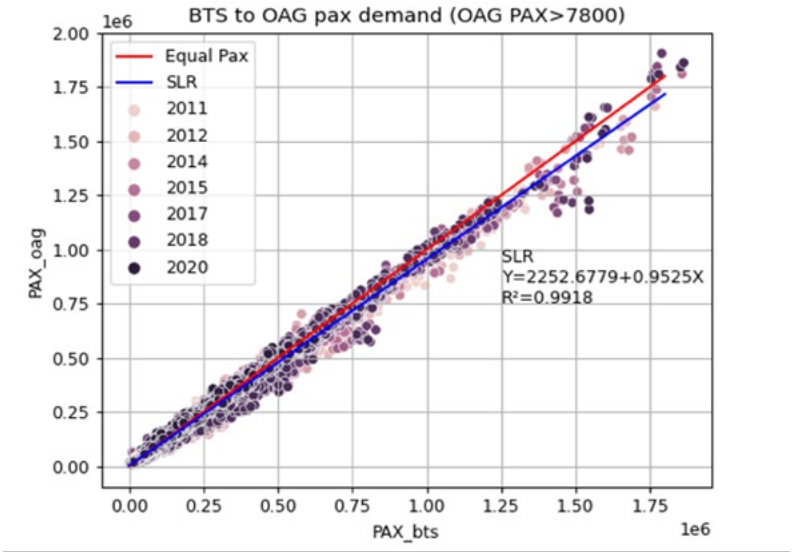

Figure 8. Comparison of U.S.-touching network demand in OAG and BTS data by using a simple linear regression (SLR) model.

Figure 9 compares the passenger demand for the existing U.S.-touching route network (according to the BTS database) with the passenger demand for the worldwide network (according to the OAG database) for the years 2011–2020. The passenger demand for the worldwide route network is significantly higher than that for the U.S.-touching network, and the demand growth rate for the worldwide route network is also higher than that of the U.S.-touching route network.

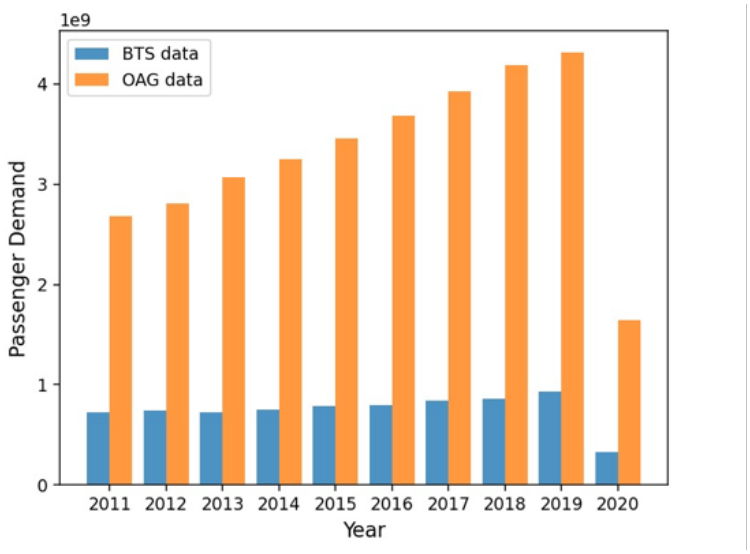

Figure 9. Comparison of passenger demand for the existing U.S.-touching route network and the updated worldwide route network.

Worldwide Route Network

The updated worldwide route network builds upon passenger demand data from OAG for the years 2011–2019; the team did not use the data for the year 2020 because of the pandemic-related decrease in demand. FLEET uses a semi-dynamic route network that follows how worldwide airlines updated their route networks from 2005 to 2019, as reported in the OAG

data, followed by a static route network from 2019 and beyond (i.e., FLEET does not predict the addition or deletion of routes in the future). In 2019 (and all subsequent years), there were 5,317 routes in the FLEET network that connect a subset of WWLMINET 257 airports. Comparison with the previous U.S.-touching route network in FLEET indicates a 170% increase in the number of routes, from 1,974 routes (U.S.-touching only) to 5,317 routes (worldwide). Figure 10 compares the worldwide route network with the U.S.-touching network, visually highlighting the increased routes in the new network.

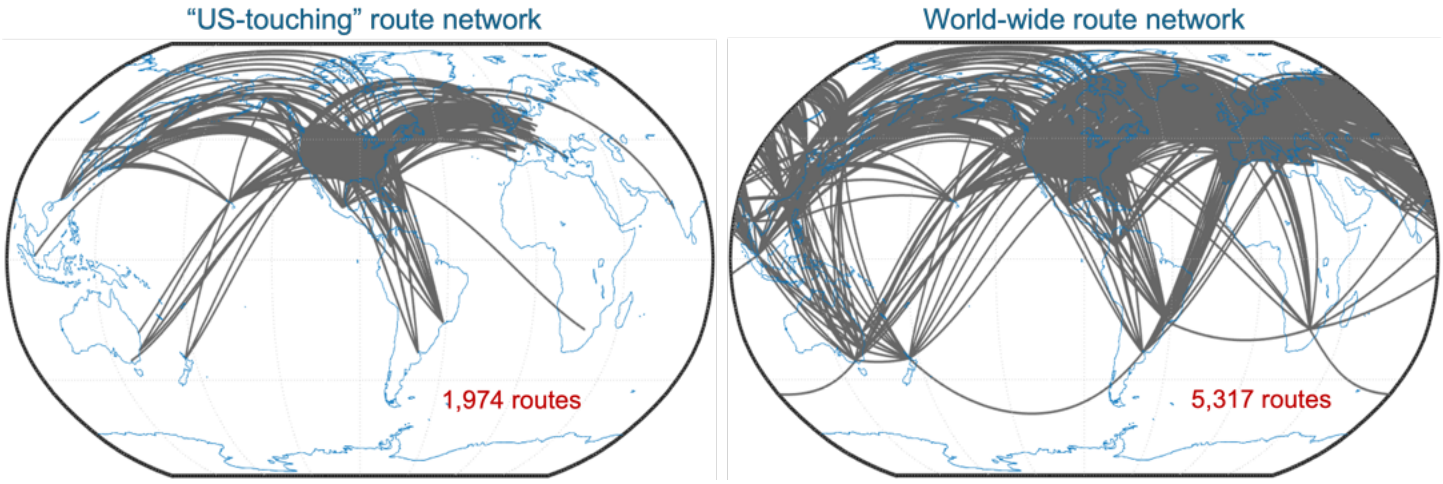

Figure 10. Comparison of the worldwide route network with the existing U.S.-touching route network in FLEET.

Aircraft Classification

The team used the 2011 BTS data of the U.S.-fleet composition to determine the classification method and the representative models of aircraft operating in the new FLEET network. The new worldwide network of FLEET is represented by 14 aircraft models, divided into six classes based on seat capacity, and then grouped into representative-in-class, best-in-class, new-in-class, and future-in-class. The representative-in-class and best-in-class models have the most aircraft within an average age group; representative-in-class models usually have an average age of approximately 15–20 years, and best-in-class models have an average age of approximately 5–10 years. The new-in-class category includes the models that entered service around the years 2015–2020, and the future-in-class category includes the models that will enter service in a future year (around 2030, depending on the seat class) and will have substantial technology improvements over the new-in-class models. The initial fleet (in 2011, the starting year of the worldwide network FLEET simulation) consists of representative-in-class and best-in-class models only. New-in-class and future-in-class models enter the fleet as the simulation proceeds to later years. The resulting representative models of each class are shown in Table 11. Class 1 and 2 are not available for the new-in-class and future-in-class technology classes, because the team determined that the demand for class 1 and 2 aircraft will be low, and these aircraft are not expected to be a significant part of the future global fleet.

Table 11. Aircraft classifications used in FLEET with the worldwide network; FLEET now uses 2011 as the baseline year.

Class	Seats	Representative-in-class	Best-in-class	New-in-class	Future-in-Class
Class 1	20-50	Saab 340B	Canadair RJ200	-	-
Class 2	51-99	ATR 72	Canadair RJ700	-	-
Class 3	100-149	McDonnel Douglas MD-80	Boeing 737-700	Airbus A220	Aircraft X3
Class 4	150-199	Boeing 757-200	Airbus A320-200	Airbus A320 neo	Aircraft X4
Class 5	200-279	Boeing 767-200	Airbus A330-200	Boeing 787	Aircraft X5
Class 6	280+	Boeing 747-400	Boeing 777-200ER	Airbus A350 XWB	Aircraft X6

Global Fleet Composition

The Purdue team used Boeing's 2012–2031 Current Market Outlook (CMO) Report (Boeing Market Outlook, 2012) and Oliver Wyman's 2017 Global Fleet & MRO Market Forecast Summary (Wyman, 2017) as primary sources to determine the size of the 2011 global fleet. Both Boeing and OW provide only "high-level" global fleet size numbers. The current work relies on the U.S. fleet's BTS data for further details, such as dividing the global fleets into different classes. The initial fleet in FLEET's worldwide network is set up by decomposing the fleet into six seat classes and taking an average of the Boeing and Oliver Wyman 2011 global fleet, followed by rounding to the nearest 10, as shown in Table 12. The composition of representative-in-class/best-in-class and age distributions was also determined with the 2011 BTS U.S.-fleet data.

Table 12. Global fleet composition in FLEET (for worldwide route network) for 2011.

	Africa	Middle East	APAC	Latin America	North America	CIS	Europe	World
Class 1	250	40	410	240	1510	210	530	3190
Class 2	150	20	250	150	920	130	320	1940
Class 3	240	230	1760	570	2150	410	1650	7010
Class 4	160	150	1140	360	1380	270	1050	4510
Class 5	70	290	670	40	510	70	400	2050
Class 6	40	170	360	10	250	40	190	1060
Total	910	900	4590	1370	6720	1130	4140	19760

Aircraft Production

At present, the aircraft production and delivery curves as well as the entry-into-service dates of the new-in-class aircraft and future-in-class aircraft for FLEET with the worldwide route network remain unchanged with respect to the previous U.S.-touching version of FLEET. However, only 40% of the total aircraft produced were previously available for purchase by the U.S. flag carrier airline in FLEET. With the update to the worldwide network, all the produced aircraft are eligible to be purchased by the global airlines in FLEET.

As mentioned before, the FLEET update to a worldwide network is still underway and will be completed in the next phase of the project. Current progress has allowed us to visualize the updated worldwide route network and updates to the passenger demand in FLEET. Figure 11 shows the normalized passenger demand in FLEET for the years 2011–2040, considering the worldwide network.

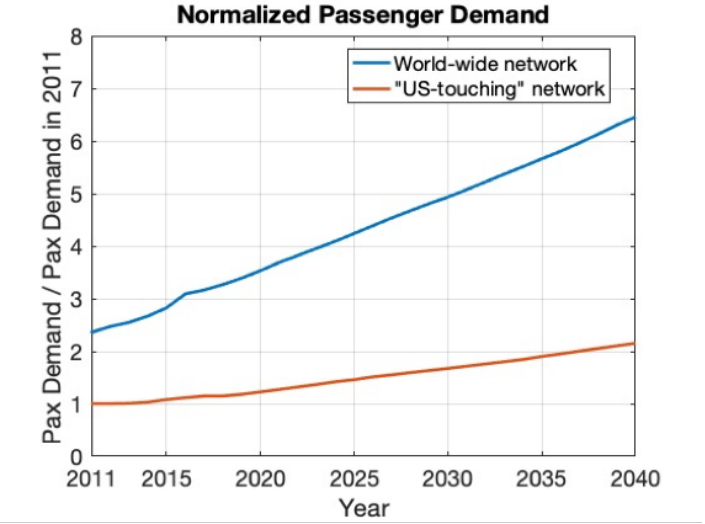

Figure 11. Normalized passenger demand in FLEET for the years 2011–2040.

Simultaneous Aircraft Allocation Approach

Currently, the Purdue team uses a sequential aircraft allocation approach for allocating the supersonic and subsonic passengers, i.e., FLEET accommodates the premium passengers first. The sequential allocation problem satisfies as much of the available supersonic demand on a set of supersonic eligible routes using the supersonic aircraft in the airline fleet. Any remaining, unsatisfied supersonic demand is then added to the subsonic travel demand, and a second allocation problem satisfies this demand by using the subsonic aircraft in the airline fleet. However, the sequential allocation approach does not allow FLEET to incorporate noise and/or airport capacity constraints and is inherently based on the assumption that airlines will always satisfy supersonic passenger demand.

To mitigate these limitations of the sequential allocation approach, the Purdue team developed another approach for allocating supersonic and subsonic aircraft at the same time in FLEET: simultaneous aircraft allocation. The simultaneous aircraft allocation treats the supersonic aircraft as options for allocation on supersonic-eligible routes alongside subsonic aircraft in the same problem. All FLEET simulations conducted to date use sequential aircraft allocation.

In the simultaneous allocation problem, the FLEET airline has the ability to use both supersonic and subsonic aircraft in any combination that yields the most profit. The problem restricts supersonic aircraft to the routes identified as supersonic eligible, similarly to how the problem limits subsonic aircraft to routes based on aircraft range capability. As with the current sequential version of the allocation problem, the simultaneous allocation approach also treats the passengers desiring SST as if they are business class or above, whereas subsonic passengers are treated as a homogenous class of passengers most closely reflecting economy-class passengers. Currently, the model still uses 5% of the total passenger demand in FLEET as the demand that exists for supersonic travel; the simultaneous allocation problem reflects both the supersonic and subsonic demand as separate types of demand, while constraints ensure that the allocation meets all demand.

The simultaneous supersonic and subsonic allocation approach has several useful advantages over the sequential aircraft allocation approach. This approach provides insights into passengers' travel preferences via supersonic and subsonic aircraft while allowing for the enforcement of noise and/or airport capacity constraints in FLEET; therefore, it is pertinent to conducting the noise-related FLEET work.

The Purdue team has completed the development of the sequential allocation approach and plans to use this allocation approach for all upcoming FLEET runs. The team has conducted several test runs by using some of the previous-year supersonic aircraft models operating on the U.S.-touching FLEET. The team will conduct runs for the updated FLEET with a worldwide route network by using simultaneous allocation in the upcoming year.

Results

Impact of Supersonic Aircraft Operations on Subsonic Operations

The FLEET simulation is run from years 2005 to 2050, with a first-generation supersonic aircraft introduced in 2025 and a second-generation supersonic aircraft introduced in 2038; the second-generation supersonic aircraft has the same block time on routes but consumes less fuel for the mission, assuming incremental improvements in empty weight, aerodynamics, and propulsive efficiency. In FLEET simulations, the aircraft are available for the airline to use 1 year after the entry into service (EIS) date (i.e., the aircraft was first available during the EIS year, but the representative day when that aircraft was part of regular service is the year following the EIS). Hence, the first-generation supersonic aircraft becomes available for allocation by the airline for a representative day in 2026. Similarly, the second-generation supersonic aircraft becomes available for allocation in 2039.

The high-passenger-density subsonic aircraft (for new-in-class and future-in-class, (classes 3, 4, 5, and 6) are made available only on routes with supersonic aircraft allocation; FLEET allocates the standard subsonic aircraft on all other routes. For simplicity in implementation, the team assumed that the airline can quickly "convert" a standard configuration subsonic aircraft to a high-passenger-density configuration, thus allowing for use of the existing subsonic aircraft acquisition and retirement models.

The simulation results presented here use the sequential aircraft allocation approach for allocating the supersonic and subsonic passengers, i.e., FLEET accommodates premium passengers first. The FLEET run presented here is based on the U.S.-touching route network and has no constraints on the number of airport operations. In addition, this work considered only the Current Trends Best Guess (CTBG) scenario from previous work (Mavris et al., 2017), which comprises nominal aircraft technology development, nominal economic growth, and nominal energy price evolution. The previously obtained

subsonic-only CTBG results were used for comparing and analyzing the supersonic with high-passenger-density FLEET CTBG allocation and fleet fuel burn results.

With the current modeling, the possible airline response to the introduction of high-passenger-density subsonic aircraft on routes with supersonic service impacts fleet-wide subsonic aircraft utilization and total fuel burn. The different ticket price approaches lead to differences in subsonic aircraft allocation, fleet-level fuel burn, and overall airline profit. The supersonic aircraft allocation and emissions remain the same for all the ticket price approaches, because supersonic aircraft are allocated first. Considering the fleet-wide fuel burn, case 1 (constant average ticket price) leads to the maximum overall fuel burn, case 2 (constant ticket price) leads to the maximum fuel burn in 2050, and case 4 (constant ticket price margin) leads to the lowest overall fuel burn among the four ticket price cases discussed. The fleet-wide fuel burn from all four cases with high-passenger-density aircraft (along with supersonic aircraft) and the case with supersonic aircraft but no high-passenger-density aircraft are higher than the fuel burn from the subsonic-only case. Figure 12 shows the fleet-wide normalized fuel burn for all cases considered. Figure 13 shows the aircraft flown miles, the passenger flown, and fuel burn from the whole subsonic fleet. The class-wise contributions (from classes 3, 4, 5, and 6 subsonic aircraft) to aircraft flown miles, the passenger flown, and fuel burn are depicted in Figures 14–16.

Case 1: Constant Average Ticket Price

Analysis of case 1 indicates a slight change in the passenger demand combined with a significant change in the subsonic aircraft allocation, as compared with the case with no high-passenger-density aircraft. The constant average ticket price approach causes the profit per trip for the high-passenger-density configuration to be higher than the standard configuration. The airline maximizes its profit by flying as many passengers as possible per trip, favoring larger aircraft to earn more profit. The airline ultimately flies more trips with class 5 and class 6 aircraft instead of the smaller class 3 aircraft, thus increasing the overall fuel burn. Figures 14c and 14d show that the aircraft flown miles (and subsequently the passenger flown) for class 5 and class 6 aircraft are much higher than those in other cases, depicting that the airline tends to fly more larger aircraft to earn a higher profit, thereby leading to higher emissions (visible in Figures 13c, and Figures 16c & d, depicted by red dotted lines).

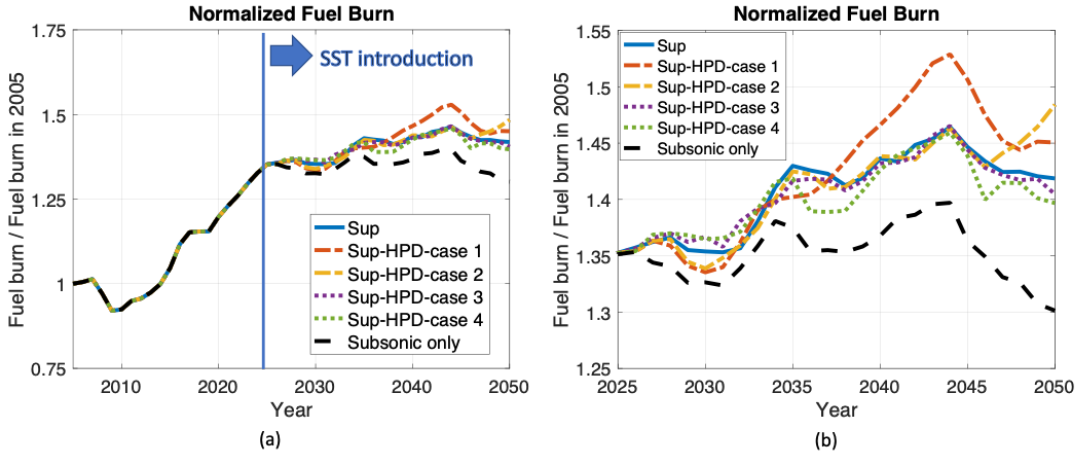

Figure 12. (a) Normalized fuel burn from FLEET simulation. (b) Zoomed-in view of normalized fuel burn starting from the year 2025.

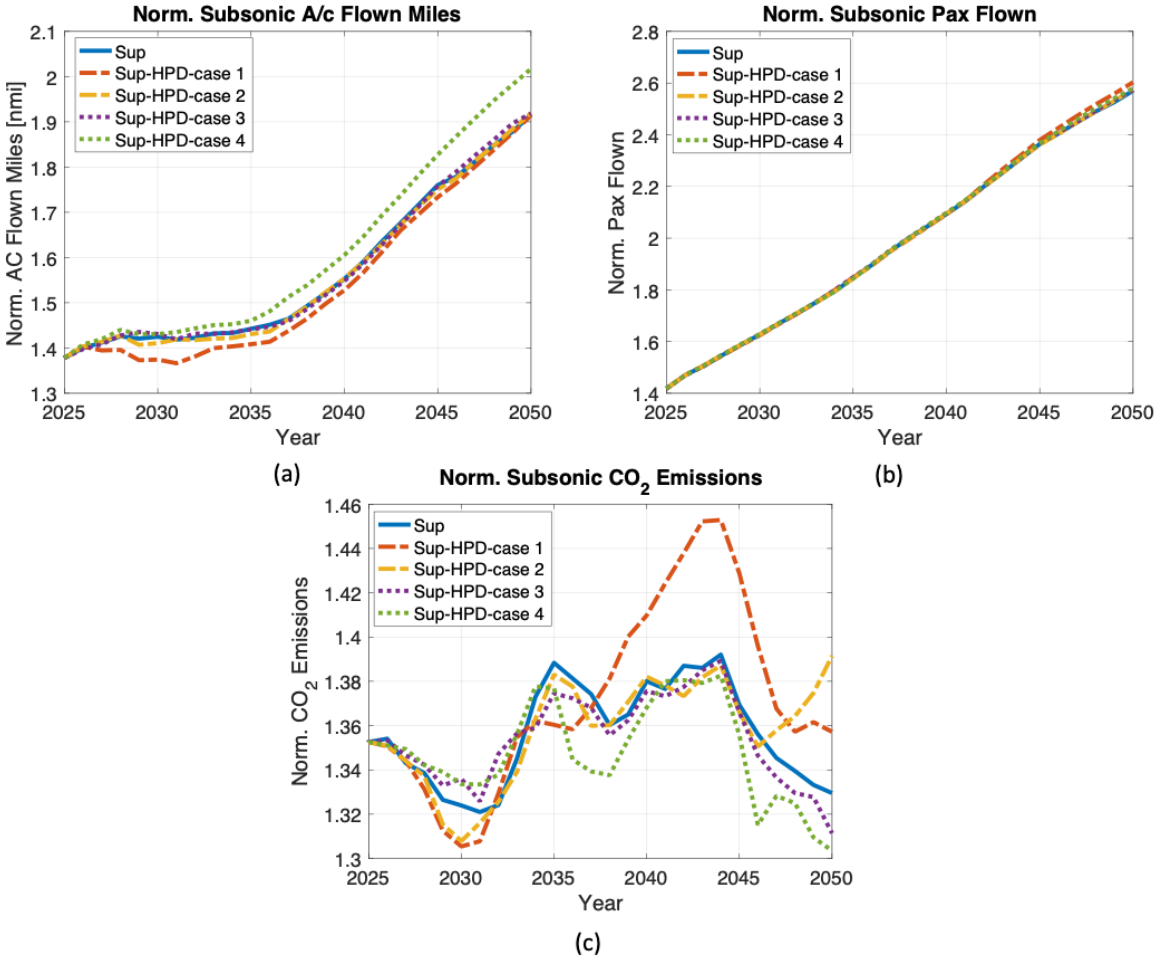

Figure 13. (a) Aircraft flown miles for subsonic fleet. (b) Passengers flown for subsonic fleet. (c) Fuel burn from a subsonic fleet. All data are normalized to respective 2005 values.

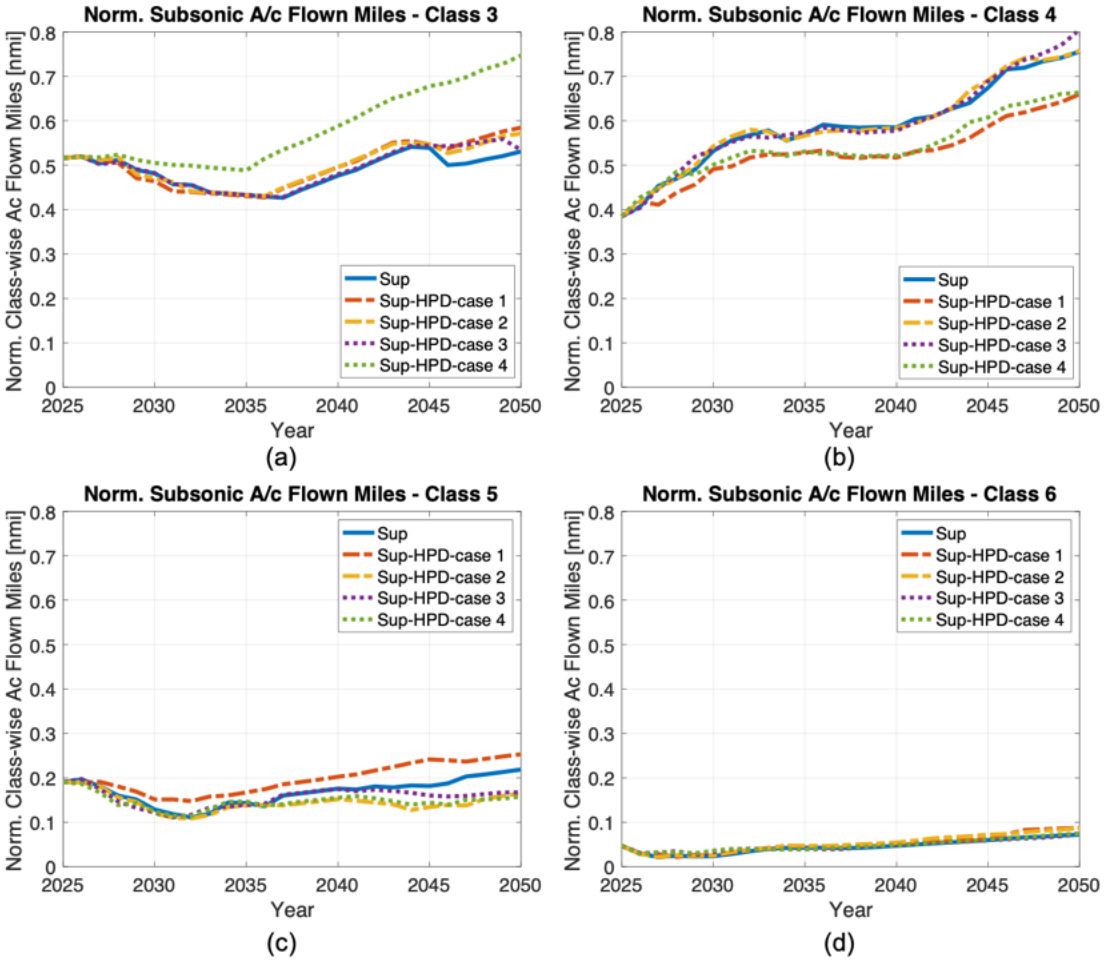

Figure 14. Normalized class-wise aircraft flown miles for subsonic fleet: (a) class 3, (b) class 4, (c) class 5, and (d) class 6. All data are normalized to 2005 total subsonic aircraft flown miles.

Case 2: Constant Ticket Price

For case 2, there is almost no change in passenger demand; the subsonic aircraft allocation changes slightly with respect to the case with no high-passenger-density aircraft. The constant business-class and economy-class ticket prices approach causes the total trip profit to increase (ticket prices remain constant, but the increase in the number of seats results in an increased trip profit). The airline maximizes its profit by flying more trips, favoring smaller aircraft to minimize the loss of business-class revenue. The airline ultimately flies more trips using class 3 aircraft and fewer trips using class 5 aircraft; after 2046, utilization of newer technology aircraft (classes 3 and 4) further increases because of higher trip margins for these aircraft. This shift in allocation after 2046 shows that the profit margin difference between differently sized aircraft plays a role in prioritizing more trips vs. carrying more economy passengers. In this case, the airline makes more profit by prioritizing more trips using smaller aircraft. The overall fuel burn is similar to that in the case with no high-passenger-density aircraft until the year 2046 (yellow dotted line in Figure 13c). Figures 16a and 16b show increased fuel burn from class 3 and class 4 aircraft after the year 2046 (depicted by yellow dotted lines).

Case 3: Constant Trip Margin

For case 3, there is a slight change in passenger demand and subsonic aircraft allocation compared to the case with no high-passenger-density aircraft. The constant trip margin approach causes the profit per trip for the high-passenger-density configuration to be same as that of the standard configuration. As in case 2, the airline maximizes its profit by flying more trips using smaller aircraft, flying more trips using class 3 aircraft and fewer trips using class 5 aircraft. Figure 14a–c (purple dotted lines) shows an increase in the aircraft flown miles for class 3 and class 4 aircraft, and a decrease in aircraft flown

miles for class 5 aircraft. The overall fuel burn is similar to that in the case with no high-passenger-density aircraft (purple dotted line in Figure 13c).

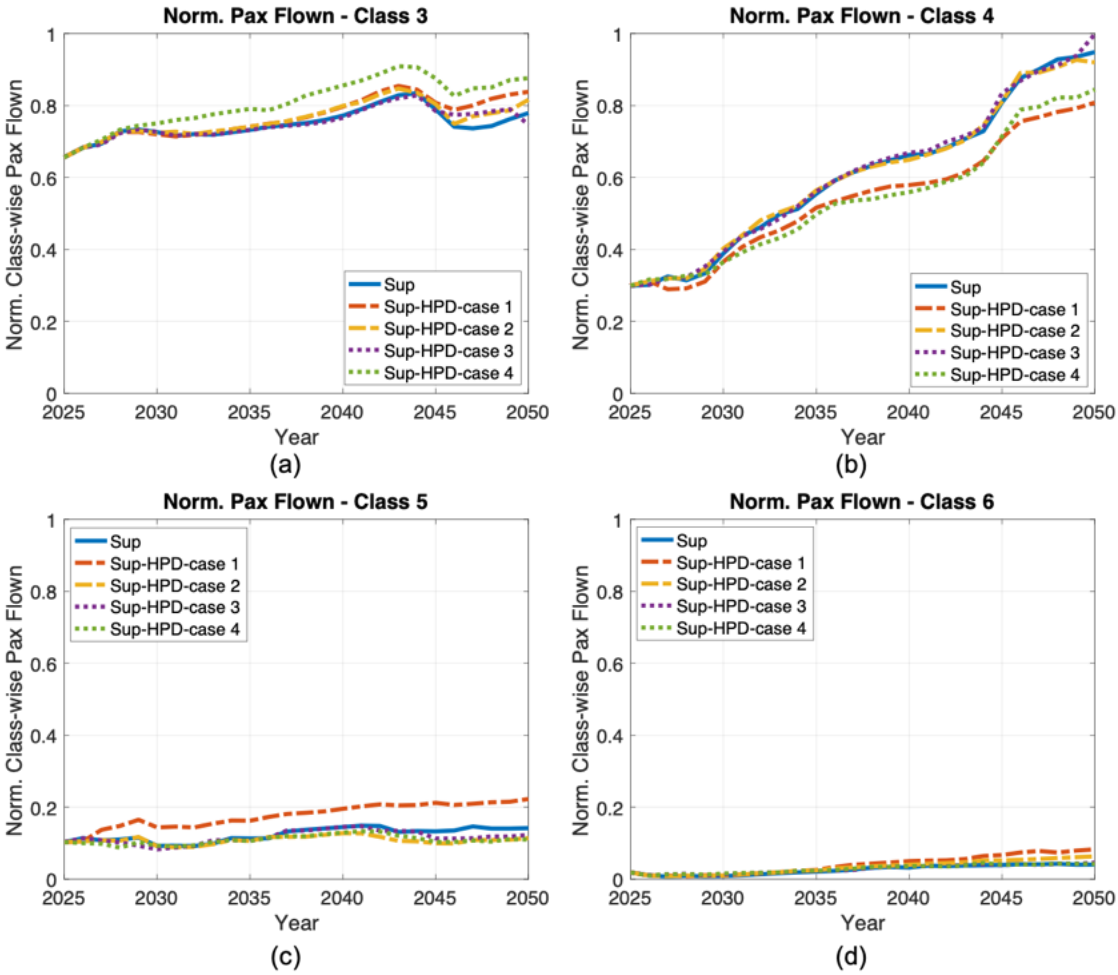

Figure 15. Normalized class-wise passengers flown for subsonic fleet: (a) class 3, (b) class 4, (c) class 5, and (d) class 6. Data are normalized to 2005 total subsonic passengers flown.

Case 4: Constant Ticket Price Margin

For case 4 (constant ticket price margin), there is a slight change in demand, but the subsonic aircraft allocation changes significantly compared to the case with no high-passenger-density aircraft. Because the airline does not alter profit margins from economy ticket prices to compensate for the loss of business-class seats, this approach causes the total trip profit to decrease as business seats are reduced by 50%. The airline maximizes its profit by flying more trips using the smaller aircraft, which allow more trips to be flown. Interestingly, the airline ultimately flies many more trips with class 3 aircraft, and fewer trips with class 4 and class 5 aircraft. Figure 13a and b show that the subsonic aircraft flown miles are highest for case 4, although the number of passengers flown remains relatively unchanged. The increase in trips on smaller aircraft (green dotted line in Figure 14a), with a decrease in the use of larger aircraft, results in a net reduction in the fleet-wide fuel burn (visible in Figures 16 and 13c, depicted by green dotted lines).

The plots in Figures 14–16 show that changes in the utilization of class 3, 4, 5, and 6 subsonic aircraft drive the changes in fuel burn for the four different ticket price approaches. Hence, the changes in fuel burn are a function of changes in passenger demand and subsonic aircraft allocation due to ticket price variations.

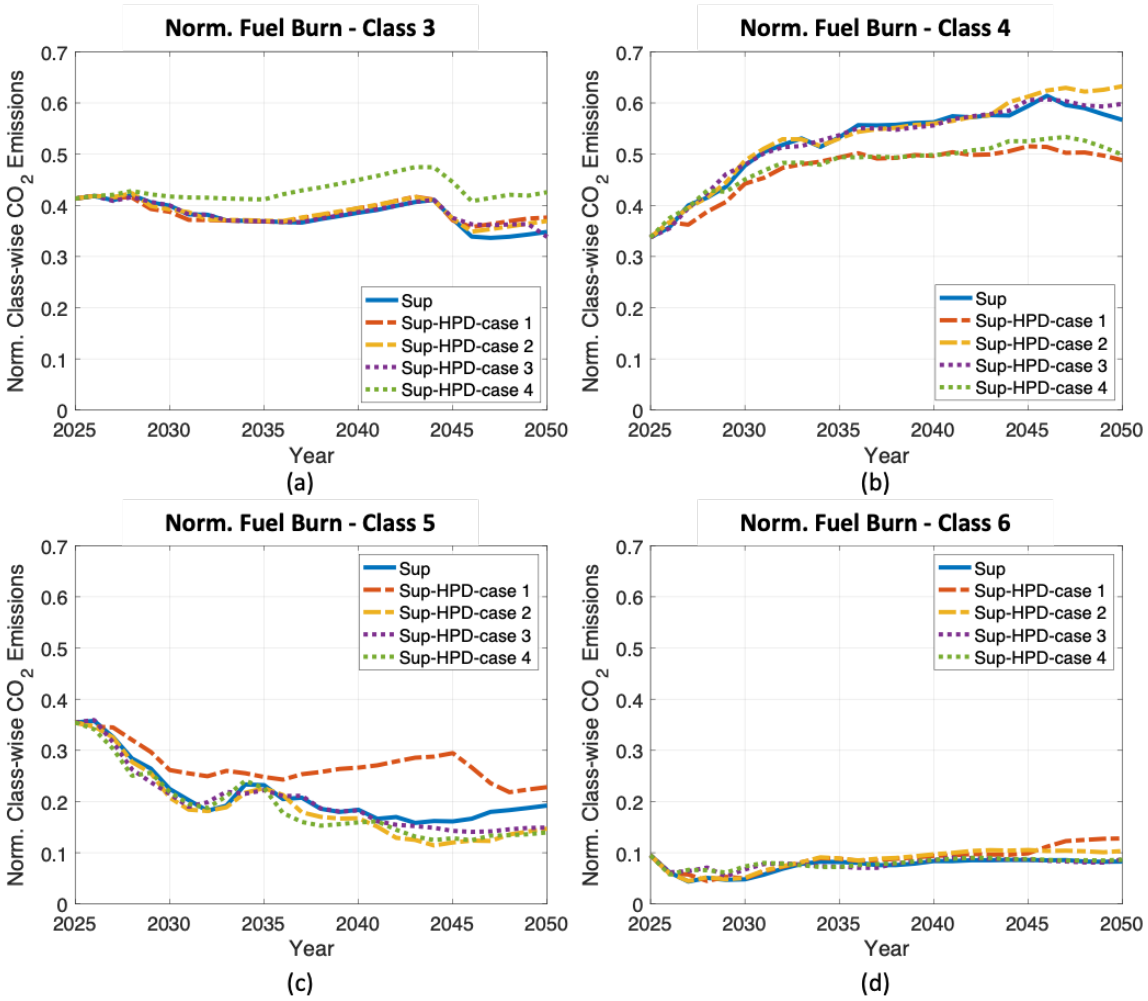

Figure 16. Normalized class-wise fuel burn for a subsonic fleet: (a) class 3, (b) class 4, (b) class 5, and (d) class 6. Data are normalized to 2005 total subsonic fuel burn.

Most Likely and Least Likely Cases

Given the current modeling assumptions, the team estimated the likelihood of occurrence of the four high-passenger-density cases in the future based on airline profit and impact on passengers, i.e., changes in ticket price. The likelihood estimation process led to the identification of a most likely case and a least likely case.

The team identified case 2, maintaining a constant ticket price, as the most likely case. In this case, the airline makes high profit, and there is no cost that is transferred to the passengers as the subsonic ticket prices stay constant. The least likely case would be maintaining a constant ticket price margin, i.e., case 4. The airline makes the lowest profit in this case, because it does not change the ticket price margins to compensate for the loss of business-class passengers—a profit-seeking airline will not follow this approach. Table 13 provides an overview of the outcomes with respect to the case with no high-passenger-density aircraft; the table also includes the team's judgement regarding the likelihood of occurrence of the four cases considered.

Impact of COVID-19 on Passenger Demand and Fleet-Level Assessments

The FLEET simulation was run from years 2005 to 2050 with a first-generation supersonic aircraft introduced in 2025 and a second-generation supersonic aircraft introduced in 2038. The simulation results presented here utilize the sequential aircraft allocation approach for allocating the supersonic and subsonic passengers, i.e., FLEET accommodates the premium

passengers first. The FLEET run presented here is based on the U.S.-touching route network and has no constraints on the number of airport operations. In addition, this work considered only the CTBG scenario from previous work (Mavris et al., 2017), utilizing the previously obtained subsonic-only CTBG results for comparing and analyzing the supersonic FLEET CTBG results, and considering the 2020 decrease in passenger demand and the possible demand recovery paths due to the COVID-19 pandemic.

Table 13. Overview of outcomes with respect to predictions when no high-passenger-density aircraft are available in FLEET (considering sequential aircraft allocation on a U.S.-touching route network).

Possible Airline Actions	Preference (Likelihood of Occurrence)	Impact on Passengers (Ticket Pricing)			Impact on Fleet-Level Fuel Burn	Impact on Airline (Profit)
		Average Ticket Price	Economy Ticket Price	Business Ticket Price		
Case 1: Constant average ticket price	2	–	↑	↑	↑	↑
Case 2: Constant ticket price	1 (most likely)	↓	–	–	↑ (slightly after 2046)	↑ (slightly)
Case 3: Constant trip margin	3	↓	↓ (slightly)	↓ (slightly)	~ (similar)	↓ (slightly)
Case 4: Constant ticket price margin	4 (least likely)	↓	↓	↓	↓ (slightly)	↓

Figure 17 shows the normalized passenger demand for the projected demand scenarios along with the baseline scenario. There is a maximum 16.8% reduction in the 2050 total passenger demand (for scenario 5) and a minimum 11.2% reduction in the 2050 total passenger demand (for scenario 3) when compared to the baseline scenario. Figure 17 also shows the normalized fuel burn for the projected demand scenarios along with the baseline scenario (depicted by a black solid line) in FLEET; the fuel burn for all six scenarios is always lower than the pre-COVID baseline scenario. There is a maximum reduction of 17.3% (for scenario 4) and a minimum reduction of 11.7% (for scenario 3) in the 2050 fleet-level fuel burn when compared to the baseline scenario. The differences between COVID-19 scenarios and the pre-COVID baseline are a combination of two factors: 1) the lower passenger demand leads to a smaller number of flights, and 2) lower passenger demand initiates early retirement of less profitable aircraft and the introduction of more profitable (more fuel-efficient) aircraft during passenger demand recovery.

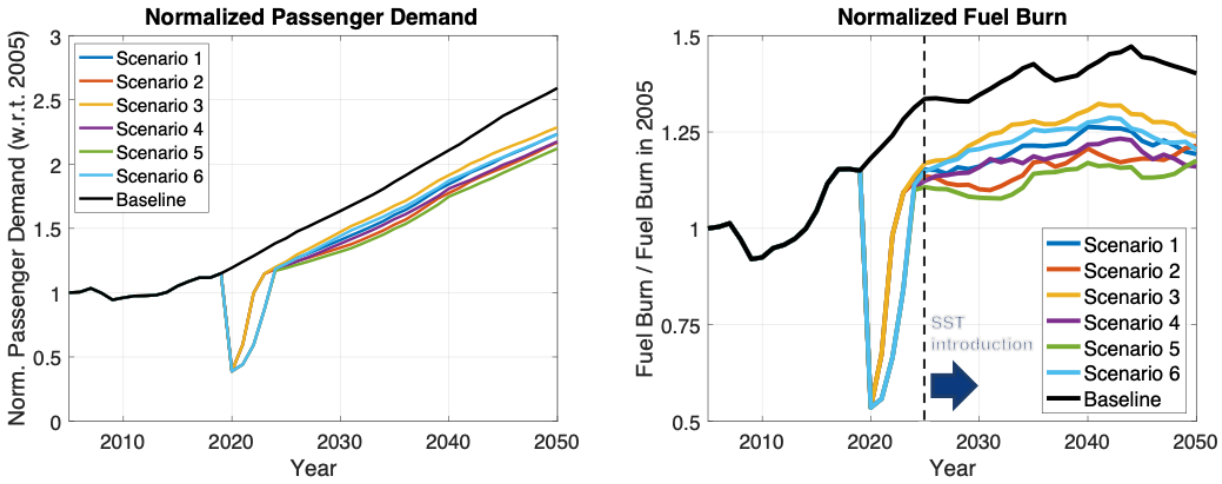

Figure 17. Normalized passenger demand and fleet-level fuel burn for different passenger demand recovery scenarios (based on a U.S.-touching route network).

Considering the year 2038, the FLEET simulation results using the projected demand scenarios show a maximum 42% reduction in supersonic passenger demand (for COVID-19 recovery scenario 6) compared with the pre-COVID baseline scenario. Analysis of COVID-19 recovery scenario 6 indicates that the 42% reduction in supersonic passenger demand leads to a 39% reduction in the number of supersonic routes allocated, from 57 routes to 37 routes, and a 43% reduction in supersonic roundtrips flown per nominal day, from 79 round trips to 45 round trips. Figure 18 shows the normalized supersonic passenger demand, number of supersonic routes allocated, and supersonic round trips flown for all six COVID-19 demand recovery scenarios and the pre-COVID baseline scenario.

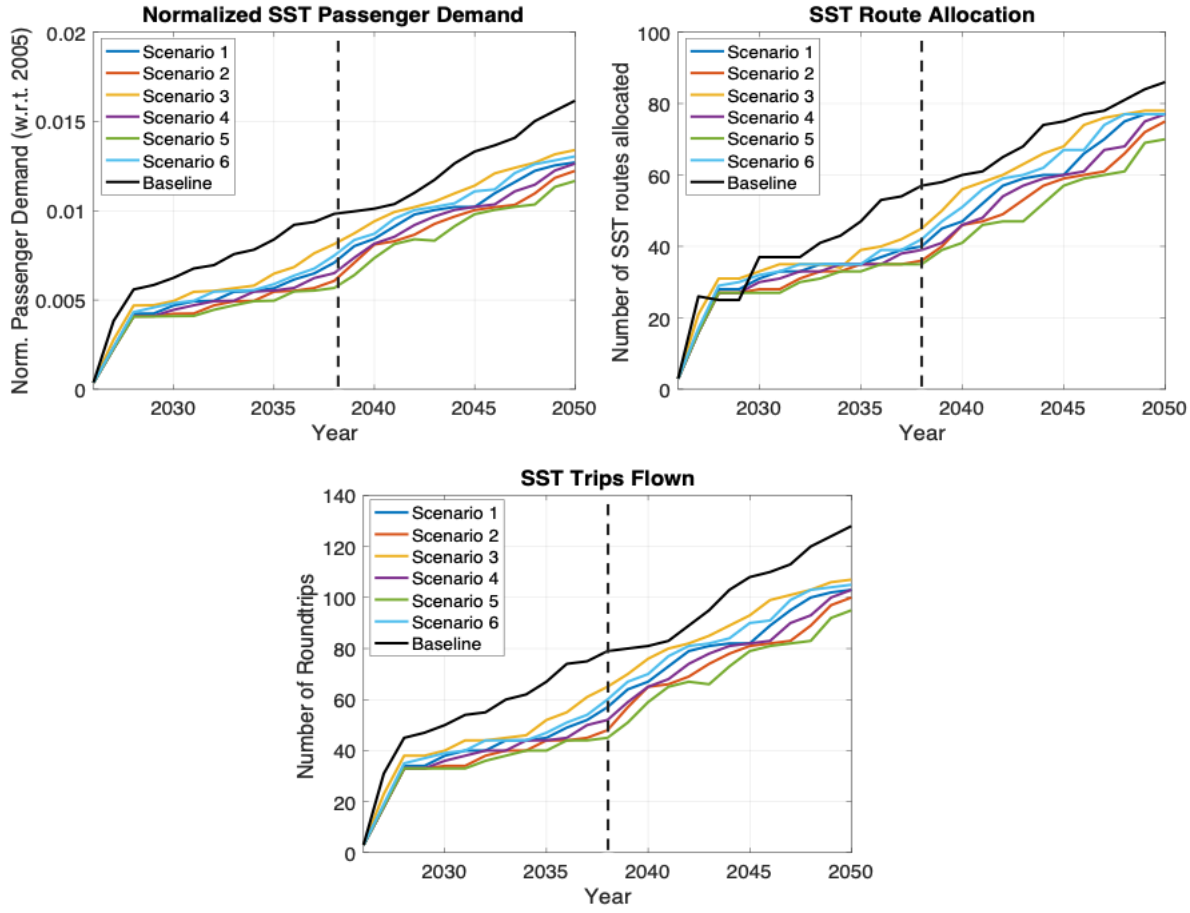

Figure 18. Normalized passenger demand, number of supersonic routes allocated, and number of supersonic trips flown for different passenger demand recovery scenarios in the year 2038.

Task 3 - AEDT Supersonic Modeling

Georgia Institute of Technology

The original intent of Task 3 was to develop methods for AEDT to model SST. At the time of writing of the proposal, AEDT utilized BADA3 for vehicle modeling; therefore, the proposal focused on BADA3 approaches. Since then, and at the time of writing of this report, AEDT is transitioning to BADA4 for new vehicle representation in AEDT, thus rendering the proposed tasks obsolete. Based on conversations with FAA technical monitors at the Spring 2019 ASCENT Advisory Board meeting, Georgia Tech was directed to focus on BADA4 coefficient generation for SST, which is described in Task 5.

Task 4 - Support CAEP Supersonic Exploratory Study

Georgia Institute of Technology

Objectives

In support of the CAEP supersonic exploratory study, or E-Study, Georgia Tech engaged in two major activities. One activity was attending CAEP meetings and authoring or contributing to numerous working papers and information papers at the working-group meetings. Specifically, Georgia Tech supported Working Group 1 (Noise), Working Group 3 (Emissions), and the CAEP Forecast and Economic Analysis Support Group. Specific results and products from this activity are discussed in

the Results section of this task. The second major activity was supersonic vehicle modeling. The Research Approach section for this task describes the methodology used to model major disciplines, such as aerodynamics, propulsion, noise, and mission analysis. Finally, the Results section discuss the results of the Design Mach Trade Study using the nine vehicles modeled.

Research Approach

As with previous work, the Georgia Tech researchers leveraged the Framework for Advanced Supersonic Transports (FASST) M&S environment to model the supersonic vehicles for this task. This framework is based on the Environmental Design Space (EDS) [,]. The goals of EDS and FASST are the same: to provide a modeling and simulation environment that enables tradeoffs and interdependencies among aircraft system-level metrics. The difference is that EDS was designed for subsonic aircraft; therefore, modifications were implemented to enable the modeling and simulation of supersonic aircraft. In the case of FASST, the system-level metrics of highest interest are the vehicle weight, design mission fuel burn, and landing and takeoff (LTO) or certification noise. The flow diagram for the FASST environment (Figure 19) shows the inputs, outputs, and interconnections between each discipline's analysis module in the modeling and simulation environment.

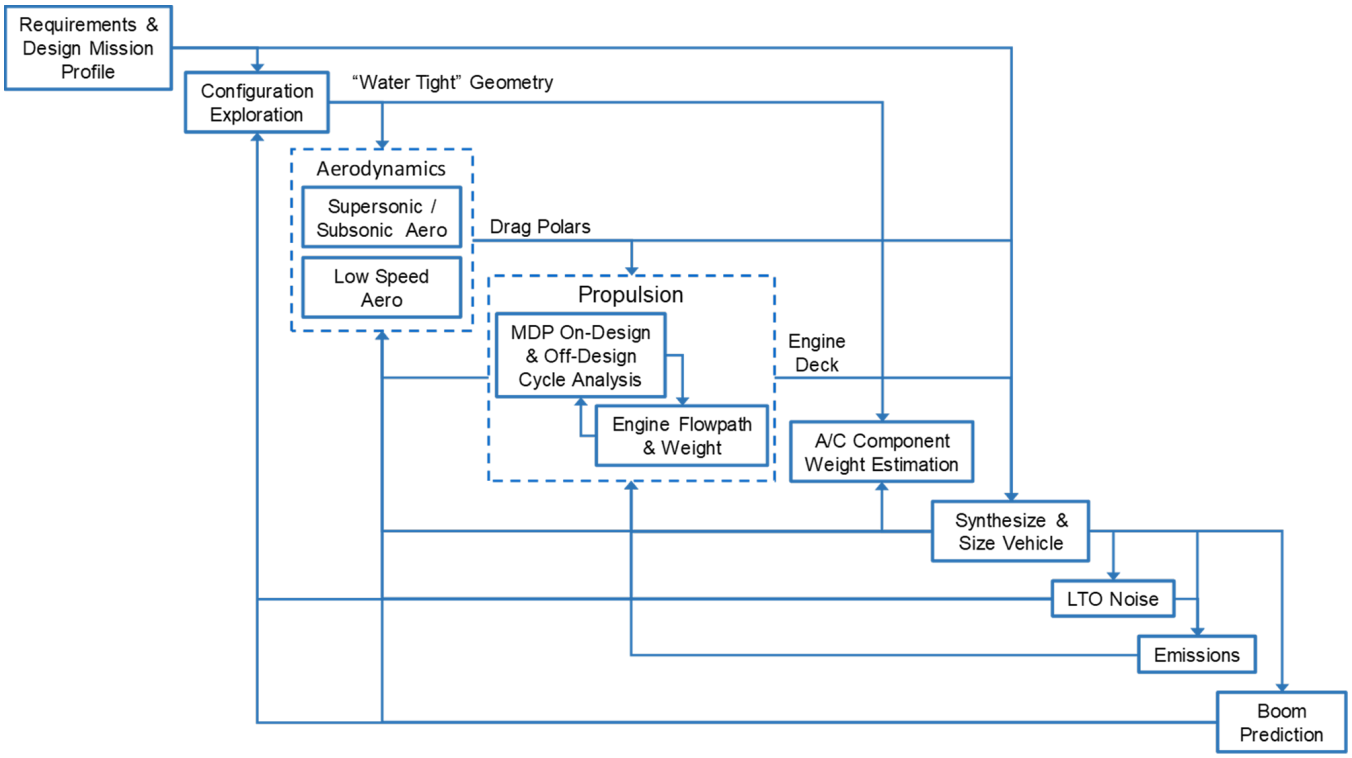

Figure 19. FASST flow diagram.

The requirements and design mission are specified by the research team and are outlined in the following sections. Some of the high-level requirements are the number of passengers, the design Mach number, and the design mission range.

The configuration exploration and aerodynamics drag polar generation are performed in a local setting, outside of FASST. This process involves parametrically generating a 3D model of the airplane in Engineering Sketch Pad (ESP). From this model, a CFD mesh is generated that can then be run through CART3D to analyze the vehicle's supersonic aerodynamic performance. For this task, a design of experiments (DoE) was conducted to properly shape the planform, keeping the fuselage, engine, and tail geometry fixed. From the data collected from executing FASST for this DoE, a set of surrogates are generated, and the cruise lift-to-drag ratio (L/D) is used to select the best vehicle. After a design is selected, the complete high-speed drag polar is developed with CART3D and a takeoff and landing drag polar is generated in NASA's Vehicle Sketch Pad, AERO2S, and WINGDES. Both sets of drag polars are fed into the mission analysis and vehicle sizing module. More details on the aerodynamic module are included in the Aerodynamics Modeling section.

The engine cycle modeling is performed in Numerical Propulsion System Simulation (NPSS), and flowpath and weight estimation is conducted with Weight Approximation for Turbine Engines (WATE). This process provides an engine deck and engine weight to the mission analysis and vehicle sizing module. The propulsion analysis is detailed further in the Propulsion Modeling section. For the vehicle mission analysis and sizing, NASA's FLOPS is used. FLOPS uses the inputs of engine deck, drag polar and other vehicle configuration parameters to estimate the weight, and it then iterates on the vehicle gross weight to complete the mission prescribed by the designer. FLOPS scales the engine and wing as required to achieve the required thrust and wing area based on a specified wing loading and thrust-to-weight ratio. If the engine is scaled in FLOPS, it is subsequently rescaled in the engine analysis to obtain an updated engine performance and weight. This iteration continues until the engine no longer requires scaling. After sizing, the vehicle is analyzed through a series of design missions. Specifically, the takeoff and climb-out trajectory is of interest because of its importance to LTO emissions and noise. The modeling assumptions for emissions and noise are also included below.

Propulsion Modeling

Cycle Architecture Selection

A mixed-flow turbofan (MFTF) engine cycle was selected for this work. Most modern subsonic aircraft use a high-bypass-ratio separate-flow turbofan (SFTF). This type of engine allows for high overall efficiency by moving a greater amount of air for high propulsive efficiency while being able to maintain a high overall pressure ratio (OPR) for high thermal efficiency. As a result of the higher mass flow rate, high bypass SFTF have lower jet velocities for the same thrust, an aspect also beneficial for from a noise perspective. However, moving more air comes at the cost of larger engine diameters and greater thrust lapse due to altitude as density decreases. Supersonic aircraft face high drag in transonic acceleration and cruise at higher altitudes than subsonic aircraft; therefore, the greater thrust lapse of engines with a high bypass ratio (BPR) is not ideal. Additionally, supersonic engines have longer inlets and nozzles than subsonic engines, to efficiently decelerate and accelerate the flow. Therefore, higher airflow and fan diameter result in very large and heavy inlets and nozzles. An MFTF is a simple modification of the SFTF accomplished by mixing the bypass and core flow before the stream exits through a single exhaust nozzle. The mixing of the two streams offers some efficiency gains and higher specific thrust, which in turn reduces the thrust lapse problem [3]. MFTFs have been shown to offer a good compromise of thrust-specific fuel consumption (TSFC), jet velocities (i.e., specific thrust), weight, complexity, and fuel burn relative to other cycles, such as the turbojet, turbine-bypass engine, and variable-cycle engines [5].

Cycle Modeling

A schematic is included in Figure 20, depicting the components in the engine model and their connectivity. The inlet, fan, high-pressure compressor (HPC), both turbines, and the nozzle are modeled with parametric performance maps. Each vehicle uses a different inlet map from the Performance of Installed Propulsion System Interactive (PIPSI)/INSTAL maps [8]. The inlet chosen (Table 14) for each vehicle class was based on the range of Mach numbers and the inlet type. The nozzle map used in all configurations is the plug nozzle map from the PIPSI/INSTAL library [**Error! Bookmark not defined.**]. The fan and HPC maps are generated with the NASA tool CMPGEN within the FASST environment to avoid the need for map scaling. The turbine maps are notional maps that are scaled, because the FASST environment does not currently include a routine to parametrically generate turbine maps. The design point performance of all turbomachinery was estimated using a simple mean-line approximation. In addition to performance, the mean line calculation also estimates the gross dimensions, number of stages, and RPM, which are required inputs for the engine flowpath and weight analysis.

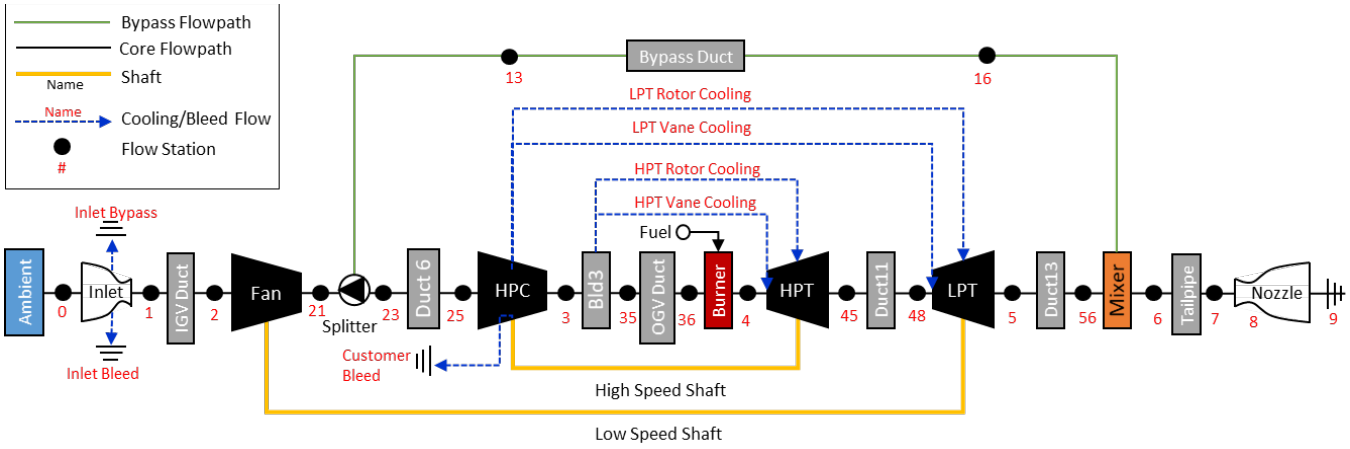

Figure 20. Engine schematic of a clean-sheet design for a medium SST.

Turbine cooling flows are determined from the NASA-developed CoolIt model [10], which computes the required cooling flow as a function of metal temperature and the cooling effectiveness parameter $\phi = (T_{gas} - T_{metal})/(T_{gas} - T_{cool})$. An advanced impingement and film cooling technology is assumed to cool the turbine blades [11]. The rotor blades were assumed to be made of an advanced single-crystal nickel superalloy, and the vanes were assumed to be made of a ceramic matrix composite material. The mixer, combustors, and ducts were all modeled with constant nominal loss metrics. Estimates for horsepower extraction, and customer bleed were based on the passenger class of the aircraft.

Table 14. Inlet selection for each vehicle class.

Vehicle	Inlet Name	Description
GT_SSBJ	NVSTOL	Axisymmetric, 3-ramp, expanding centerbody, external compression
GT_MediumSST	R2DSST	2D, 4-ramp, variable geometry, mixed compression
GT_LargeSST	ATS2	2D, 4-ramp, variable geometry, external compression

Cycle Design Methodology

A clean-sheet engine design was conducted rather than a fixed-core refan design. In a clean-sheet engine design, the entire engine is a brand-new design with all of its components sized as required. In contrast, a fixed-core refan design involves selecting a fixed core from an existing engine and designing a new low-pressure spool (fan and low-pressure turbine), inlet, and exhaust system. A simultaneous, multi-design-point (MDP) approach was used in this work to size the engine. Classical single-point analysis sizes the engine at single flight condition and subsequently iterates to ensure that requirements are met under other flight conditions. The MDP method enables simultaneously meeting design requirements and sizing components under multiple flight conditions [12]. The flight conditions considered in this work are listed in Table 15. The aerodynamic design point (ADP) is the sizing point of the engine and a reference point for defining the turbomachinery component performance. The ADP selected in this study was the transonic acceleration point at which having enough thrust is critical to overcome the high drag. The top of climb (TOC) point is typically a critical point at which adequate thrust for a minimum specific excess power is needed. Additionally, this point is part of the supersonic cruise segment, and thus efficiency is a critical concern. The takeoff point is critical to ensure sufficient thrust at rotation and for one engine inoperative. The cooling flow sizing point sizes the turbine cooling flows for the condition of maximum gas temperature and maximum cooling flow temperature.

The NPSS solver is then used to determine a set of independent parameters (fuel flow, airflow, BPR, etc.) that would meet specified target values of certain dependent parameters. An MFTF engine cycle is defined by the following five parameters: fan pressure ratio (FPR) = P_{t21}/P_{t2}, OPR = P_{t3}/P_{t2}, throttle ratio (TTR) = T_{t41max}/T_{t41SLS}, maximum turbine rotor inlet temperature (T_{t41max}), and extraction ratio □(EXTR) = P_{t16}/P_{t56} [13]. The selection of the throttle ratio is the same as the selection of the design turbine inlet temperature and in turn the Mach number at which the engine reaches T_{t41max}. In this study, an assumed technology limit for T_{t41max} is set at 3300 $°R$. Bypass ratio is another key metric but will be a fallout of

selecting the above five cycle variables. For this study, the extraction ratio is set to 1.1 to increase the bypass ratio without significant mixing losses. The ADP airflow is set to meet a TOC thrust requirement subject to constraints on thrust requirements at other points. The thrust requirements are scaled as the vehicle is run through mission analysis. The inlet capture area is sized to ensure that the inlet and engine are perfectly matched at the TOC.

Table 15. Cycle design points for a medium SST engine.

Design Point	Mach	Altitude (ft)	ΔISA ($°F$)	Purpose
Aerodynamic Design Point (ADP)	1.2	39,000	0	Size turbomachinery and engine
Top of Climb (ToC)	Design Mach	55,000	0	Match thrust requirements for top of climb/cruise
Takeoff	0.3	0	18	Match thrust requirements for takeoff
Cooling-Flow Sizing	Design Mach	45,000	0	Size cooling flows

Off-Design Power Management

This section describes how the engine operates in off-design mode through the entire flight envelope. Full power at any flight condition is defined as running the fuel control to target 100% corrected fan speed, constrained by maximum temperature limits on the compressor discharge ($T_{t3max} = 1790\,°R$) and turbine rotor entrance ($T_{t41} = 3300\,°R$). In addition, the nozzle throat is variable and set to hold the design stall margin. At part power, the fuel flow and fan speed are reduced to hit the thrust target, and the nozzle throat is varied to maintain a high fan efficiency. For noise analysis only, a different power management logic is used wherein part power is achieved by initially moving along the 100% speed line of the fan map, thereby decreasing the pressure ratio and increasing the stall margin. This is less efficient but results in a greater reduction of jet velocity for the same reduction in thrust by holding the airflow. This is constrained by a maximum stall margin, to avoid adverse choking effects, at which point the fan speed is reduced to further reduce thrust.

Flowpath and Weight Model

The flowpath and weight of the engine are estimated using a model developed with WATE++ and inherited from a previous supersonic study in which Georgia Tech was involved [**Error! Bookmark not defined.**]. The model is modified for a 2D supersonic inlet and an axisymmetric plug nozzle, and changes were made to some turbomachinery parameters based on a preliminary analysis method developed for this study. The inlet weight is modeled by using the regressions from PIPSI [**Error! Bookmark not defined.**]. The nozzle model is modified for an axisymmetric plug nozzle by extending the internal plug outside the nozzle with a 15° half-angle and setting the external convergent flap to match the plug half-angle. A custom module for calculating the weights of variable geometry actuators was also developed. A preliminary analysis code based on constant-meanline assumptions was developed to estimate the number of stages of turbomachinery required, and parameters such as the hub-tip ratio, area, radii, and blade speeds. This preliminary turbomachinery code is run in conjunction with cycle analysis to set the component efficiency and the geometric parameters, and the results are then passed to the WATE++ input to ensure consistency in the geometry used to compute both final component efficiency and component weight.

Emissions Modeling

One important issue in the development of any aircraft is environmental acceptability [14] particularly for SSTs, which consume more fuel than their subsonic counterparts. To predict the NO_x emissions, a NASA High Speed Civil Transport rich burn, quick quench, lean burn (RQL) combustor technology correlation is assumed [15] and is shown below. This equation is used to predict the NO_x emissions index ($EINO_x$), which determines the number of grams of NO_x produced per kg of fuel used at each of the NO_x certification points. The $EINO_x$ in turn is used to estimate the total NO_x emitted through the entire mission and for assessing CAEP certification limits in terms of grams of NO_x per kN of thrust.

$$\mathrm{EINO_x} = 23.8\,(\frac{P_3}{432.7})^{0.4}\exp\,[\frac{(T_3 - 1{,}027.6)}{349.9} + 0.014]$$

The nvPM emissions for several supersonic engine candidates were also estimated in this study through a procedure based on the Döpelheuer–Lecht equation, as described in CAEP11-WG3-PMTG09-IP06, with a suitable reference engine selected for each case. The Döpelheuer–Lecht equation is:

$$\mathrm{EI} = \mathrm{EI}_{\mathrm{ref}} * \left(\frac{\mathrm{FAR4}}{\mathrm{FAR4}_{\mathrm{ref}}}\right)^{2.5} * \left(\frac{\mathrm{P3}}{\mathrm{P3}_{\mathrm{ref}}}\right)^{1.35} * \frac{\exp(-20000/T_{fl})}{\exp(-20000/T_{fl,ref})}$$

where FAR is the fuel-to-air ratio, and the flame temperature is given by:

$$T_{fl} = 2281 * \{\mathrm{P3}^{0.009375} + [0.000178 * \mathrm{P3}^{0.055} * (\mathrm{T3} - 298)]\}$$

Note that the units of P3 are bars, and the units of T3 are degrees Kelvin.

Issue 28 of the ICAO Emissions Databank (issued December 23, 2020) reported, for the first time, measured mass and number EI nvPM data for the subsonic LTO cycle. In the present study, these new data were used for the reference engines, along with updated estimates of the supersonic engine cycles.

Three supersonic engine candidates were considered in this study: the NASA STCA engine, the Boom study engine, and the Gulfstream study engine. For both the NASA STCA and Boom engines, the reference engine was selected to be the CFM56-7B. Two different estimates of the Gulfstream engine cycle were considered, but in both cases, the reference engine was the BR700-725A1-12 engine. Both of the CFM56 and BR700 reference engines have reported mass and number EI nvPM values in issue 28 of the ICAO Emissions Databank. Only the mass EI nvPM was considered in this study.

For use of the Döpelheuer–Lecht equation, reference engine values for P3 and FAR4 are required as a function of T3. The reference engine data were generated using the ASDL EDS estimates of the CFM56 and BR700 engines. In each case, a sea-level static standard day power hook was run, and the resulting P3 and FAR4 values were curve fit (polynomial) vs. T3. The accuracy of the P3 and FAR4 estimates was evaluated indirectly by comparison of the thrust-SFC curves predicted by the EDS models to the fuel flow data available in the ICAO Emissions Databank.

The supersonic engine cycle data consist of P3, T3, and FAR4 for both the subsonic LTO cycle (four power settings) and the supersonic LTO cycle (five power settings). For each value of T3 given, reference engine values of P3 and FAR4 were read from the EDS data curve fits. The reference EI nvPM was interpolated (linear) from the ICAO data as a function of T3. Then the Döpelheuer–Lecht equation was used to estimate the mass EI nvPM for the supersonic engine. The normalized results are tabulated in the Propulsion Results section.

Aerodynamic Modeling

Analysis Workflow

A general analysis process was developed, as illustrated in Figure 21, to obtain the aerodynamic performance of multiple aircraft designs. This process was then automated with Python and implemented by using Georgia Tech's high-performance computing (HPC) facilities. Because the analysis workflow was automated and easily parallelizable, many designs could be analyzed at once. Thousands of aerodynamic analyses could be completed in a matter of hours, thus allowing for rapid evaluation of designs and generation of drag polars.

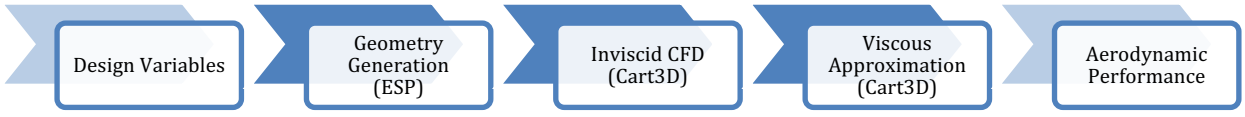

Figure 21. Analysis workflow for aerodynamic performance predictions.

Starting from a set of design variables, the first step was to generate a CAD representation of the aircraft geometry. This process was done using Engineering Sketch Pad (ESP), a lightweight, open-source CAD tool developed by MIT. ESP allows users to easily script generation of complex geometries and to expose design parameters. Therefore, changing global parameters, such as the sweep angle or taper ratio, would automatically and seamlessly scale and reposition the different sections of the wing. After a new geometry was defined, it was then saved to a generic CAD file (the EGADS format in the current workflow) and tessellated for later use in CFD analysis.

With the tessellated geometry, the aerodynamic performance of the aircraft was then obtained by using CFD. These simulations were performed with CART3D, an INVISCID CFD code with immersed boundaries that was developed by NASA. The reason for using CART3D in the current process was its rapid execution with reasonable accuracy. In fact, a single design could be evaluated in approximately 15 min on the Georgia Tech Phoenix cluster, thus allowing us to quickly assess many designs within a relatively short time frame. The code also provides a viscous drag estimation tool that uses the computed surface pressure distribution together with boundary layer equations. Although the viscous drag estimated in this manner is reasonable, it should not be perceived as having the same accuracy as RANS results. However, for initial design analysis, the costs of a RANS based analysis were deemed too high, and consequently the viscous drag module was used instead.

Design Selection Process

The objective of the design selection process was to select the best design for each SST vehicle class, i.e., the vehicle configuration that maximized L/D at its design Mach number; therefore, a purely supersonic aerodynamic design effort. Although this exercise could have been conducted by directly linking CART3D to an optimization algorithm, such an approach would have had substantial drawbacks. First, because of the lack of an adjoint solution for the viscous component of drag, any gradient-based optimization would have required finite differencing, which is wasteful. Gradient-free approaches, in contrast, would not have been efficient either, owing to the number of design variables considered. Additionally, optimization is a sequential process in which designs are evaluated one after the other. This approach fails to take advantage of the parallelization afforded by the high-performance computing clusters available to Georgia Tech. As such, a surrogate-based design optimization (SBO) strategy was selected. SBO approaches are robust, thus eliminating the risk of premature termination from CART3D crashing. Surrogates also typically tend to smooth out the impacts of noisy data and outliers on the responses, making it easier for the optimization algorithm to converge. The design space can be visualized easily with the surrogates, especially with the help of profiler plots in the statistical software JMP, thereby providing valuable diagnostic information and qualitative checks on expected trends. Finally, with surrogates of key responses, the optimization problem can be modified quite easily, such as by adding constraints or changing the objective function, without a need to rerun CFD from the beginning.

The first step in the SBO approach is the formulation of a sampling plan. In this case, the goal was to create a globally accurate surrogate model for L/D, and thus a DoE with 1,000 samples was created for each of the SST vehicle classes. These designs were obtained using a Latin Hyper Cube sampling plan to ensure that the samples were spread across the design space. For a given SST vehicle class, each of the 1,000 designs was evaluated in CART3D at the design Mach number, and then at the off-design Mach numbers where appropriate. For C_D, the INVISCID and viscous components were computed separately. The solutions from the CART3D viscous module were noisy, with respect to variations in some design parameters, as shown in Figure 22 for an aspect-ratio variation, for example. Of note, the INVISCID L/D trends are smooth, indicating no issues with the primary CART3D solver. However, the noise introduced by the viscous component of drag affects the viscous L/D trends with AR to a point where the viscous and INVISCID L/D optima with respect to the aspect ratio are different. Given that no justifiable physical explanation could be provided for the C_D^{visc} trends, we took steps to address this issue.

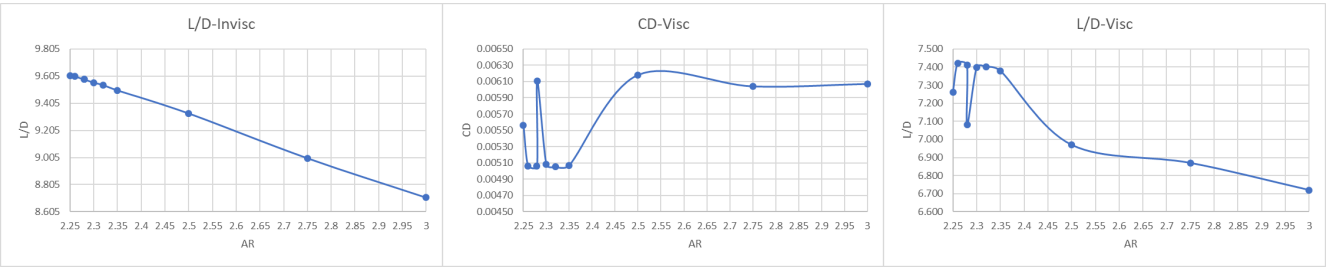

Figure 22. INVISCID and viscous trends with aspect ratio for a generic SST.

To minimize the adverse impacts of such noise in the selection of the optimum designs, we averaged out the viscous component of C_D over the 1,000 samples in each DOE to obtain one representative value of C_D^{visc} for each Mach and altitude combination at which the optimization exercise was conducted. This average value was then added to each individual value of C_D^{inv} to obtain an estimate for the viscous L/D for each of the 1,000 designs in the DOE. Surrogate models were then fit to this response.

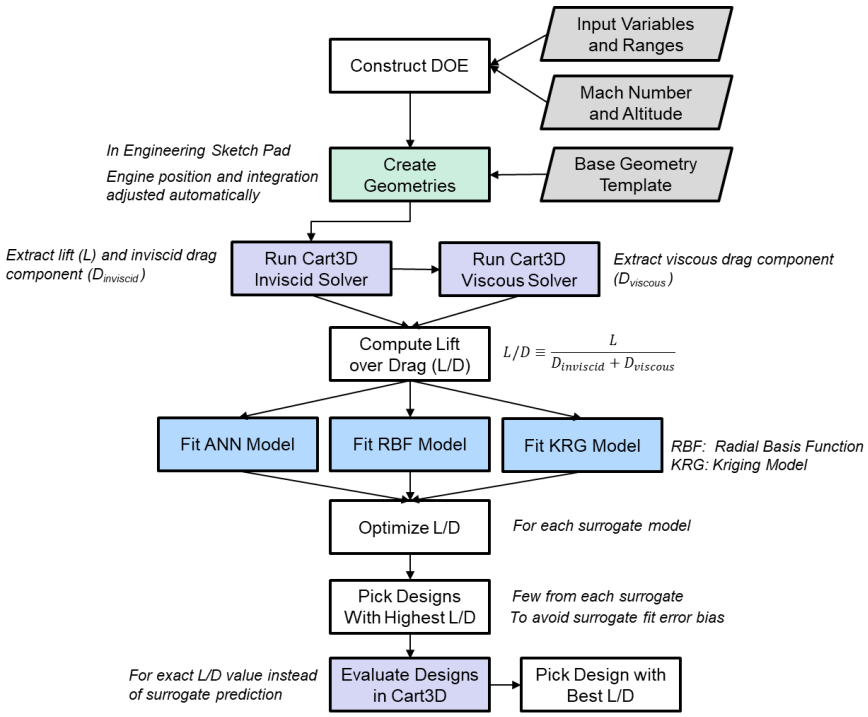

Figure 23. Aerodynamic optimization process.

The main outcomes of this exercise were a triplet of vehicle designs for a given SST passenger class, each optimized at a different Mach number. These vehicles were then evaluated at different Mach–altitude points to generate a series of drag polars encompassing the entire mission. For the polars, the values of C_D^{visc} directly predicted by CART3D were used, because a geometry-averaged, or a flight-condition-averaged C_D^{visc} value does not make sense in this context. Ideally, each vehicle in the triplet should have the highest L/D at the Mach number at which it was optimized, with the other two optimized vehicles showing a lower L/D at the same conditions. This condition is necessary for the vehicle to be "optimal" at a given Mach number. However, given the noisy nature of the C_D^{visc} trends discussed above, this expected behavior was not observed in some instances. As such, the vehicle designs were manually perturbed in this scenario to ensure that the resulting L/D was indeed the highest at the chosen Mach number.

Geometry Parametrization

A major modeling challenge has been defining a parametric representation of the nacelle in the ESP model. To simplify this task, because both the airframe and engine cycle were undergoing constant updates, unpowered flow through nacelles was used to represent the engines. Inlet ramps, exhaust nozzles, and any internal components were neglected at this stage to further reduce the complexity of parameterizing this model. Although greatly simplified, modeling the nacelle installation parametrically remained a difficult task. The primary issue was parametrically shaping the nacelle to the curvature of the wing to remove any gaps between the nacelle and the forward and aft sections of the wing. If the parametric definition of the nacelle resulted in any gaps, high- or low-pressure pockets would build up in the gaps that would adversely affect the aerodynamic efficiency of the aircraft. Because the parametric model needed to be able to handle thousands of DoE cases,

designing custom integration and cowling for any gaps with the wing, as would probably be the case in detailed design, was not an option. Figure 24 shows how a gap between the leading edge of the nacelle and the wing results in a high-pressure zone (of note, between the early and final nacelle model, the nacelle inlet had also undergone significant modeling changes, but forces on the interior the nacelle were neglected from aero analysis and bookkept in propulsion). The presence or lack of these gaps effectively created noise when trying to determine the aerodynamic efficiency of a design, because some designs generated by the DoE would have gaps, whereas others would not. A method that consistently integrated the nacelle into the wing without any gaps was needed to effectively explore the aeroshaping of these concepts. The solution that wimplemented involved taking a rectangular slice of the bottom surface and using it as the top and bottom surface of the nacelle; the rest of the nacelle geometry was built by lofting between these two faces and making the appropriate cuts for the flow through. Consequently, the intersection of the bottom of the wing and the top surface featured two identical faces, thus eliminating the possibility of any gaps.

Figure 24. Comparison between the initial nacelle-wing integration (left) and Improved nacelle-wing integration (right).

Table 16. Range of DoE variables used in geometry selection.

Variable	LB	UB
REFAREA	Fixed based on an initial estimate for each vehicle	
TAPER_RATIO_I	0.25	0.5
TAPER_RATIO_O	0.25	0.5
TWIST_R	0	1.5
TWIST_M	−3	3
TWIST_T	−6	6
SWEEP_TE_I	−5	5
SWEEP_TE_O	−5	5
AR	2.2	3.0
REL_Y_M	0.4	0.6
DIHEDRAL_I	−5	5
DIHEDRAL_O	−5	5
ANGLE OF ATTACK	1	4

The SSBJ required some special considerations for its geometry compared to the other vehicle classes. Instead of using a clean sheet-of-paper design for the aeroshaping for the SSBJ, the GT_SSBJ utilized the fuselage, nacelles, and vertical tail design from the NASA STCA, with only the wing planform being parametrized. NASA's VSP model of the STCA was used to export an IGS file that could be imported into traditional CAD software. This initial segmentation of the bodies did leave the

inner core of the nacelle free floating, which would have caused issues in the triangulation of the model for CART3DTherefore, we added a small cylindrical tube to the internal section of the engine, which connected the inner core and nacelle. The fuselage, nacelles, vertical tail, and nacelle pylons were then isolated as individual components and exported as STEP files that could individually be imported into ESP. The ESP model then unions these fixed components and a parametrically defined wing. Because the SSBJ model was a derivative of the STCA, utilizing the STCA planform as a baseline rather than enforcing the design constraints present on the other vehicle classes in this study was determined to be more appropriate. From the baseline variable ranges, the minimum trailing edge sweep needed to be substantially decreased, and the outboard taper ratio minimum needed to be slightly decreased, to ensure that the STCA baseline planform was captured in the design space.

Table 17. Cabin layout for the 55- Pax and 100- Pax aircraft.

	Cabin Layout
100 PAX	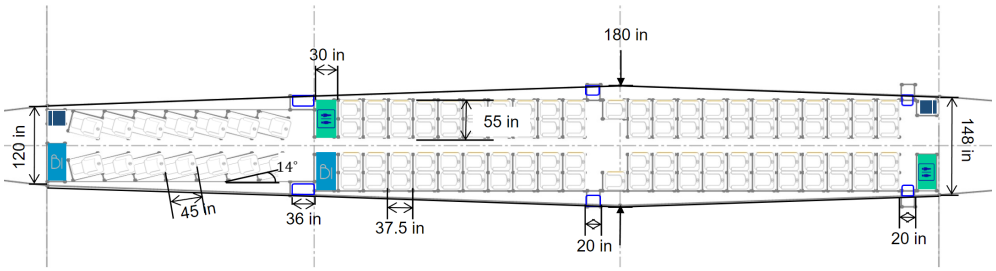 Cabin Length: 111.6 ft (1340.0 in) Cabin Diameter: 10-15 ft (120-180 in)
55 PAX	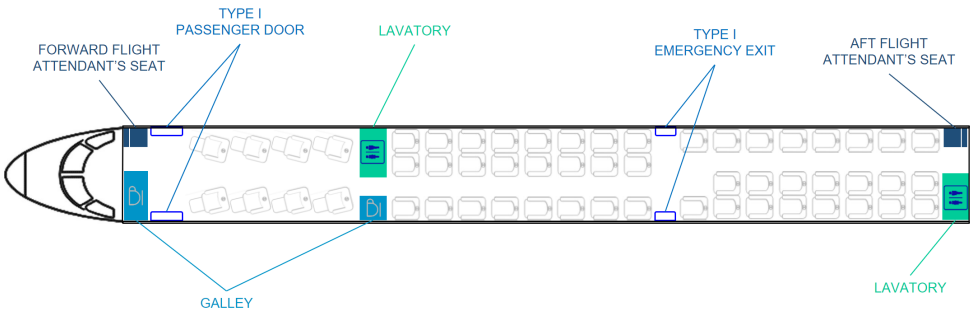 Cabin Length: 80 ft (1340.0 in) Cabin Diameter: 10 ft (120-180 in)

Mission Analysis

The mission analysis was performed by using NASA's FLOPS. For FLOPS to size and synthesize the SST, a geometry definition from the ESP is required, i.e., the L/D optimized configuration from aerodynamics, the engine deck generated from NPSS, and both the high-speed and low-speed aerodynamic drag polars. The aircraft component weights were predicted by using internal FLOPS empirical weight equations based on the vehicle gross weight and geometric information provided. A certain amount of composites were assumed in the wing, fuselage, and empennage. Two major vehicle scaling parameters, wing loading (W/S) and the thrust-to-weight ratio (T/W), were varied with each mission analysis execution to satisfy balanced field length and approach speed constraints while minimizing takeoff gross weight.

Noise Modeling

The noise assessment for each aircraft configuration was performed with NASA's Aircraft Noise Prediction Program (ANOPP). In performing these assessments, several assumptions were made in selecting and using different ANOPP modules. Table 18 lists the components of the ANOPP input file structure along with a rationale applicable to each particular module or section.

Table 18. Modules used in aeroacoustics analysis.

Component	ANOPP Module	Acronym	Rationale
Trajectory	Source Flyover Module	SFO	Considered separate trajectories (prescribed by FLOPS) for the sideline and the cutback/approach noise assessments – the difference being that the sideline trajectory did not include a cutback section after the second segment acceleration – and both cases used a VNRS takeoff trajectory
Airframe	Fink's Airframe Noise Module	FNKAFM	Standard module to predict the broadband noise from the dominant components of the airframe and based on a method developed by Fink for the FAA
Jet	Single Stream Circular Jet Noise Module	SGLJET	The single stream jet mixing noise is calculated with a methodology based on SAE ARP 876, because it is known to be the best representation of the current nozzle type.
Fan	Heidmann Fan Noise Module	HDNFAN	The fan inlet and discharge noises were assessed separately for their tone and broadband contributions using a methodology based on correlations to model and full-scale test data.
Treatment	Fan Noise Treatment Module	TREAT	Given that the chosen fan module assumes that the inlet and discharge ducts are without acoustic treatment, the attenuation spectra are applied to separate predictions of the inlet and aft radiated source noise produced by the source noise module, and a total attenuated fan noise prediction is produced.
Combustor	Combustion Noise Module	GECOR	The combustor noise was predicted with a methodology developed by General Electric and later adopted by the SAE A-21 Committee.
Shielding	Wing Module	WING	Used to compute the geometric effects of wing shielding or reflection on the propagation of engine noise (depending on the engine placement/configuration).

The VNRS previously mentioned consisted, for the purpose of the present study, of automatic (i.e., no pilot control) changes to the engine and airframe configurations during a takeoff run to help reduce noise. The following were included:

- Programmed high-lift devices (PHLD): flap deflections are controlled by the flight management system to optimize the aerodynamic efficiency for the required lift at each point in the takeoff trajectory.
- Programmed thrust lapse rate (PLR): automatic thrust reduction is controlled by FADEC and implemented immediately after the aircraft clears the obstacle during takeoff.
- Second segment acceleration (2SA): an acceleration during the second segment of the takeoff procedure (i.e., between the obstacle and the cutback point). The acceleration takes place at a fixed flight path angle and thrust until the final climb-out speed is reached. The aircraft then holds airspeed and thrust, varying the flight path angle, until the cutback altitude is reached.

The takeoff trajectory thus follows the following general procedure:

1. Takeoff at full power
2. After obstacle: reduce power to specified PLR level, pitch to specified flight path angle and climb and accelerate to final climb-out speed
3. At final climb-out speed: adjust flight path angle to hold final climb-out speed at constant thrust
4. At cutback altitude: reduce thrust to cutback level and hold constant thrust and speed; continue climbing

Table 19 shows how the takeoff trajectory (VNRS) used for all aircraft in this study differs from other common takeoff trajectories. Figure 25 shows how the trajectory and throttle settings vary for each of these options.

Table 19. Differences between trajectory types.

	Cutback	Programed Lapse Rate	Programed High-Lift Device
No Cutback Trajectory	No	No	No
Standard Trajectory	Yes	No	No
Advanced Trajectory	Yes	Yes	No
VNRS Trajectory	Yes	Yes	Yes

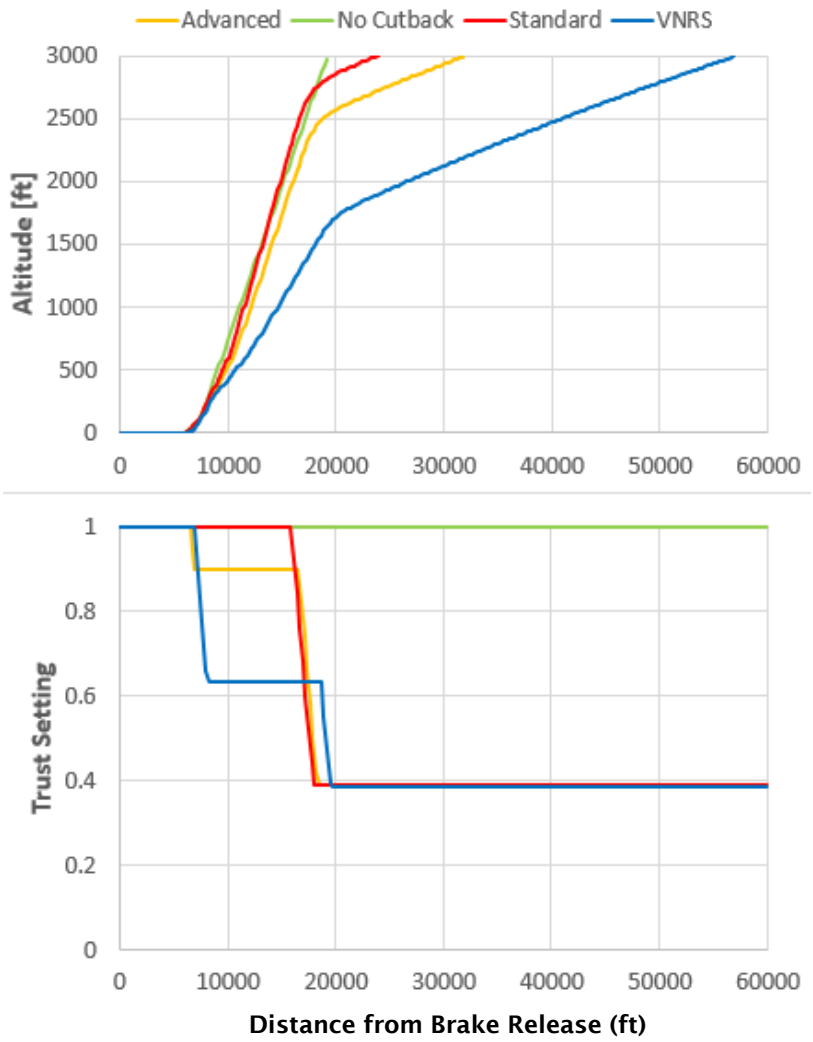

Figure 25. Altitude (top) and thrust setting (bottom) vs. distance from brake release for GT_MediumSST.

Design Mach Number Trade Study

Introduction

No explicit LTO noise standards currently exist for commercial supersonic aircraft. Related regulations are currently being discussed in ICAO WG1, with a focus on two primary questions. First, should LTO noise certification trajectory requirements remain the same as subsonic requirements? Second, what should the stringency level be for commercial supersonic aircraft? At the request of the FAA Office of Aviation Environment and Energy (AEE), technology trade studies were added to the work scope to examine the interdependencies between design fuel burn, LTO NO_x, and LTO noise as a function of design Mach number for several classes of vehicles, as listed in Table 20. To aid in answering the previous two questions, this work posed several additional questions:

- What is the rate of change in fuel burn per effective perceived noise in dB (EPNdB) reduction in LTO noise and noise margin?
- How does that rate of change vary with Mach number and vehicle class?
- Can a commercial supersonic vehicle with moderate noise technology meet current subsonic Chapter 14 rules?

Table 20. Design Mach number trade study for different vehicles.

Passenger Class	Baseline Design Mach Number	Design Mach Number Range for Trades	Design Range (nm)	Number of Engines and Location
8	1.4	1.4, 1.6, 1.8	4,240	2 fuselage & 1 empennage
55	2.2	1.8, 2.0, 2.2	4,500	4 under-wing
100	1.8	1.6, 1.8, 2.0	5,000	4 under-wing

Approach

To establish the interdependencies a set of vehicle and operational design variables were explored for each vehicle. The variables used in this study are shown in Table 21. Ranges for each of these variables were established, and a DoE was created to explore the design space. The design process for each discipline was as detailed in the previous sections. After all the simulations were run for each vehicle and Mach number over their respective design spaces, the data were filtered to ensure that all requirements and constraints were met, and the set of nondominated solutions composing the Pareto frontier were obtained with JMP. An illustration of the Pareto front for fuel burn and noise is shown in Figure 26. Results of this study are presented below in the Results section.

Table 21. Design variables for establishing interdependencies.

Airframe Geometry	Engine Cycle	Vehicle Sizing	Takeoff Trajectory
• Trailing edge sweep (inboard and outboard) • Twist (root, mid, and tip) • Taper ratio (inboard and outboard) • Dihedral (inboard and outboard) • Wing break location	• Fan pressure ratio • HPC pressure ratio • Turbine inlet temperature (i.e., throttle ratio)	• Thrust loading (thrust-to-weight ratio) • Wing loading (weight-to-wing area ratio)	• % Programmed lapse rate • Initial climb angle • Constant speed transition altitude • Cutback altitude

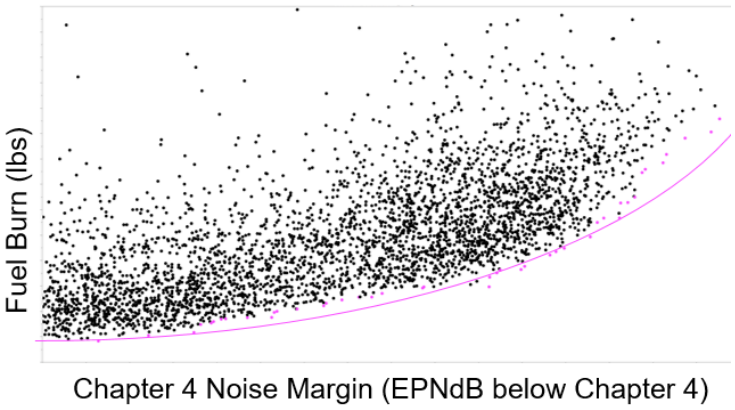

Figure 26. Example scatter plot of fuel burn vs. noise margin for all designs simulated with the Pareto frontier (pink).

Results

Design Mach Number Trade Study

The results in this section demonstrate that the LTO noise of an SST is a strong function of passenger class (i.e., maximum takeoff mass [MTOM]), Mach number, and engine placement. More specifically, several key findings were as follows.

1. Fuel burn and fuel burn vs. noise margin slope increases with:
   - Mach number (Figures 27 and 28),

  - Noise margin (Figures 27 and 28), and
  - Vehicle class (Figures 27 and 28).
2. A tradeoff (V-shape) exists in the effects of a quieter engine cycle (lower jet velocity) and fuel burn (heavier/louder vehicle; Figure 29).
3. LTO noise increases:
  - Mach number (Figure 29) and
  - Vehicle class (Figure 29).
4. Minimum noise does not necessarily meet the current subsonic Chapter 14 noise rules (Figures 29 and 30).
5. Relatively smaller SSTs are less sensitive to supersonic/subsonic cruise split (Figures 35–37).
6. LTO NO_x increases as fuel burn decreases, owing to increasing FPR and OPR (Figure 31).
7. LTO NO_x also exhibits a tradeoff (V-shape; Figure 32):
  - OPR and FPR increase from the minimum, the vehicle becomes smaller, and the noise decreases, but NO_x increases (Pareto optimal points).
  - At a certain point, the OPR and FPR increase past the minimum noise optimum, and both NO_x and noise increase.
8. LTO NO_x vs. Mach as the OPR increases for the selected designs (Figures 33 and 34).

The data points shown in Figures 27–29 are the series of non-dominated designs composing the Pareto front of design mission block fuel and certification noise margin. Figures 27 and 28 were plotted separately for ease of visibility due to the differences in the scale of block fuel between the large SST, medium SST, and SSBJ. The figures show that larger vehicle classes consume more fuel for designs with the same noise margin. In addition, within a vehicle class, a higher Mach number increases fuel requirements, as can be seen by the vertical position of each curve. Similarly, moving to the right along the noise margin axis shows that a design with a greater noise margin results in increased block fuel. The same conclusions hold for the slope of block fuel with respect to noise margin. That is, the increase in block fuel per dB of increase in noise margin increases with vehicle class, Mach number, and noise margin. Figure 29 swaps the axes of Figures 27 and 28, and replaces fuel burn with MTOM, and noise margin with absolute cumulative LTO noise level, to provide a typical plot of noise limits. The same results seen in Figures 27 and 28 can also be seen in Figure 29, but several additional conclusions can be drawn. The first is the tradeoff or V-shape of the curves. To the left of the minimum are the designs for which the noise is dominated by the jet velocity, and to the right are designs dominated by vehicle size effects on noise. That is, at a certain point, design changes that further reduce jet velocity are outweighed by the adverse effects on vehicle and engine size, partly because of the higher fuel burn requirements. Another conclusion is that, for the choice of architecture and technologies, the minimum noise design may not meet Chapter 14 requirements. A design to the right of the Chapter 14 limit line could be chosen but this design would not only have worse fuel burn but also would be louder in terms of absolute noise. This can be seen more clearly in Figure 30, where the final selected designs for the MediumSST and LargeSST do not meet Chapter 14 requirements. Figure 29 shows the raw data, whereas the designs in Figure 30 were based on subsequent optimization. This was done by first constructing a surrogate model and attempting to minimize fuel burn within 1dB of the raw data minimum noise design. A subsequent DoE on just the LTO operational variables was conducted to assess whether any further reductions in noise might be possible for the same fuel burn and to ensure that the trajectory met all requirements. This essentially shifted the design to the left, such that it was no longer compliant with Chapter 14 but had a better fuel burn for approximately the same noise. The SSBJ designs differ significantly partly because the differences in requirements were in a lower range and involved much fewer passengers, but also because of the choice of three over-wing engines. As such, the region of the design space sampled did not yield the right side of the tradeoff seen in Figure 29 for the MediumSST and LargeSST. The SSBJ was also a three-engine over-wing design so it is likely that fewer engine and engine placement, in addition to the vehicle class, played a role in its sensitivity relative to the larger vehicles.

The data in Figures 31 and 32 show the Pareto front on LTO NO_x (subsonic rules) vs. block fuel and LTO noise, respectively. Both plots show that as fuel and noise decrease, the LTO NO_x increase. This effect is caused by an increase in the OPR, which drives the increase in NO_x. However, this result is somewhat misleading, because lower fuel burn is generally observed to be the result of higher OPR and higher FPR, but noise generally has an inverse relationship with fuel burn. This aspect is explained in Figure 29, although the data sets between the plots are different. To the left of the minimum in Figure 29, the fuel burn (i.e., MTOM) decreases as a result of the increased FPR and OPR, and this drives an increase in LTO NO_x as well as LTO noise, because of the lower BPR and higher jet velocities. To the right of the minimum in Figure 29, the fuel burn continues to increase as a result of lower FPR and OPR. This results in higher LTO noise due to the size of the vehicle dominating the effect of a lower jet velocity engine. However, because LTO NO_x is normalized by thrust, it is only a function of OPR, and thus it continues to decrease as fuel burn increases, as seen in Figure 31. If it were not normalized by thrust, the amount of NO_x would also show a tradeoff (V-shape) similar to that in Figure 29. As the OPR further decreases, the growth

in vehicle size and fuel burn will dominate, and the non-normalized amount of LTO NO_x will begin to increase as the OPR decreases and fuel burn increases. In Figure 32, only the design space to the left of the minimum in Figure 29 is shown. Moving from right to left in Figure 29, the noise reduces as a result of increasing FPR and OPR, which reduce the vehicle size and thereby reduce the noise, which in turn increases the LTO NO_x. However, to the left of the minimum, as FPR and OPR continue to increase, both LTO noise and LTO NO_x increase and are therefore not included on the Pareto front. In essence, LTO NO_x vs. LTO noise (Figure 32) has a similar V-shape to that in Figure 29, in which the area to the right of the minimum is not Pareto optimal, except that the points where both NO_x and noise increase are not shown. The only reason why they are shown in Figure 29 is that those points were obtained on the Pareto front of block fuel vs. noise margin. Figures 33 and 34 plot the LTO NO_x for each selected vehicle design, as described above, as a function of OPR. Because the chosen designs were selected primarily with consideration for noise and fuel burn, these plots show the expected trend in which that as Mach number decreases the optimal OPR increases resulting in an increase in LTO NO_x.

Figures 35–37 plot the results of fuel fraction for a fixed-range off-design mission with varying amounts of subsonic cruise. As the Mach number increases, the fuel burn increases more steeply for a greater amount of subsonic cruise. An observation from this analysis was that as the Mach number decreases, a Mach number exists at which the design is always more efficient in subsonic flight despite being optimized for supersonic flight. That is not to say it is better than a vehicle optimized for subsonic flight; instead, it may just be more optimal in subsonic flight than supersonic flight. Additionally, larger vehicle classes tend to have a steeper slope for the same Mach number, as shown in Figure 36. Finally, the rightmost point, the 100% subsonic cruise, deviates below the trend line of the preceding points, because it does not ever go supersonic and saves fuel by avoiding the transonic acceleration segment. These results are only initial observations and warrant further investigation to provide a comprehensive understanding of the behavior or supersonic vehicles when operated subsonic at some percentage.

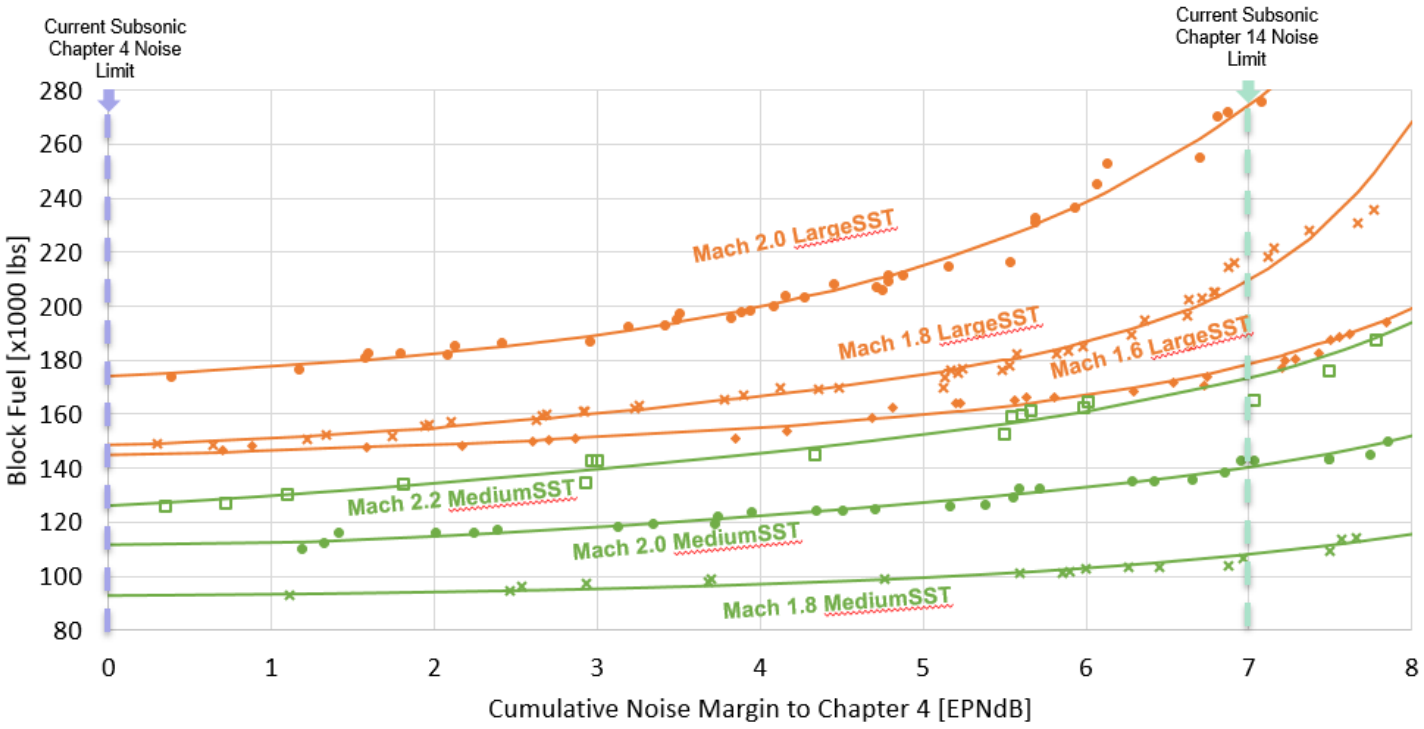

Figure 27. Design mission block fuel vs. cumulative LTO noise margin for large SST and medium SST.

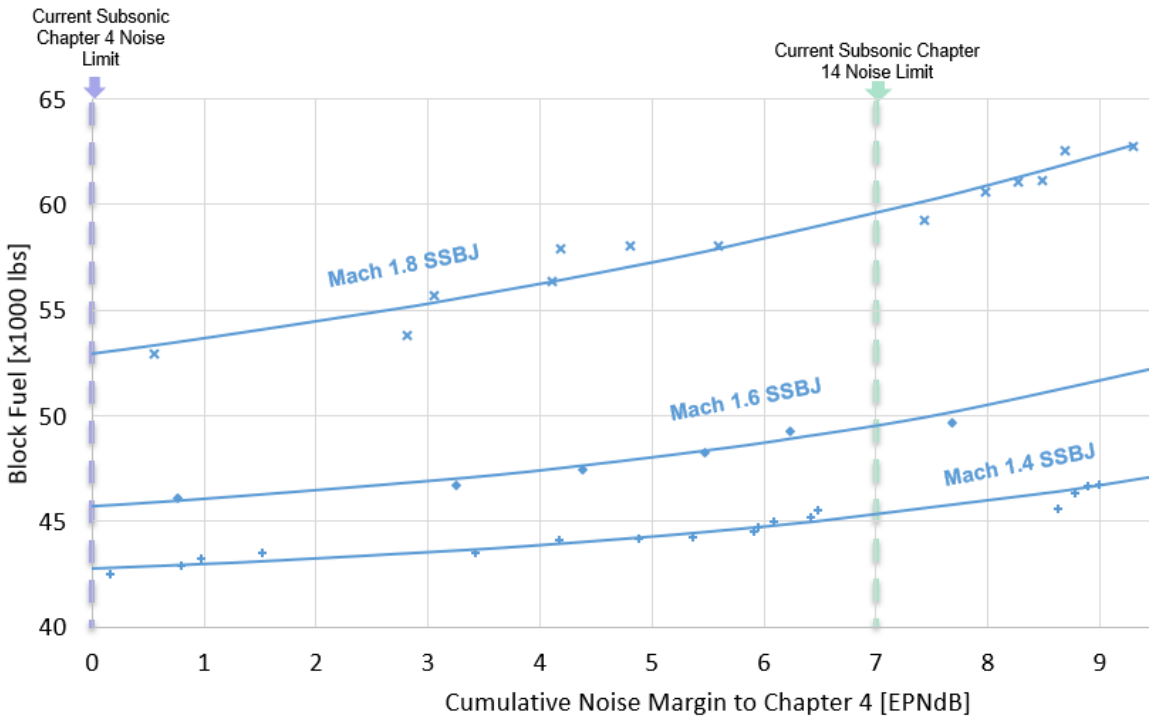

Figure 28. Design mission block fuel vs. cumulative LTO noise margin for SSBJ.

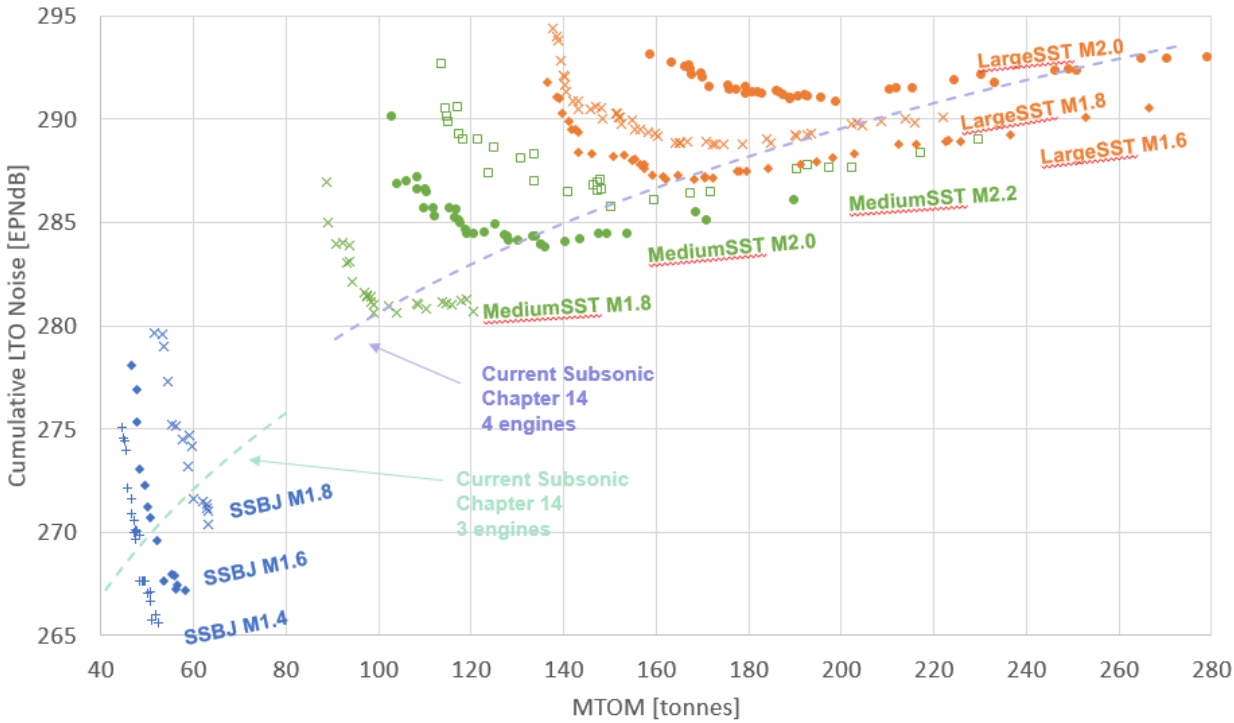

Figure 29. Cumulative LTO noise vs. maximum takeoff mass.

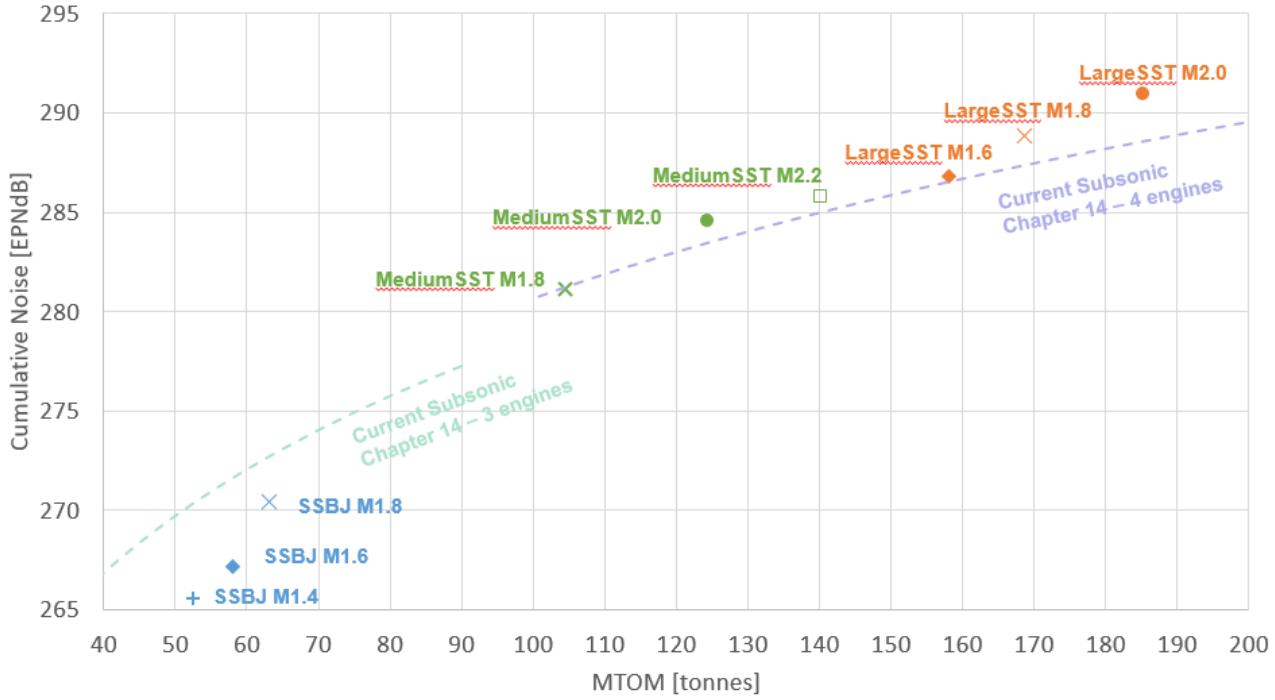

Figure 30. Final designs selected.

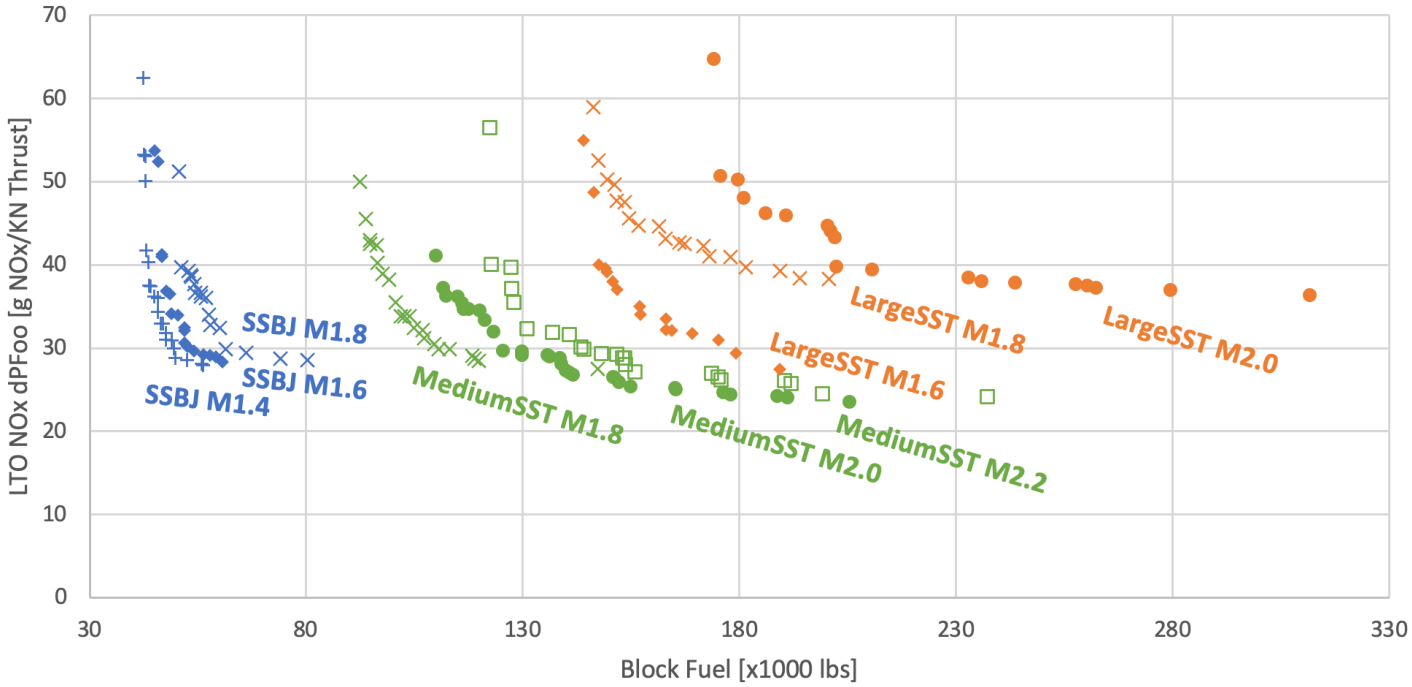

Figure 31. LTO NO_x dPFoo vs. design mission block fuel.

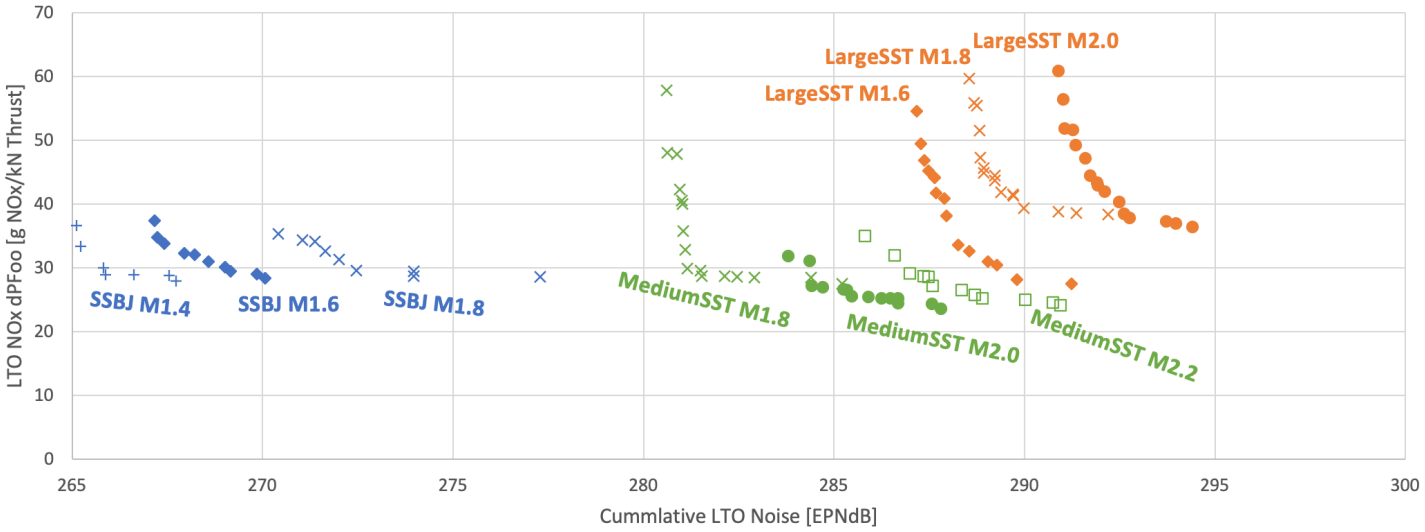

Figure 32. LTO NO_x dpFoo vs. cumulative LTO noise.

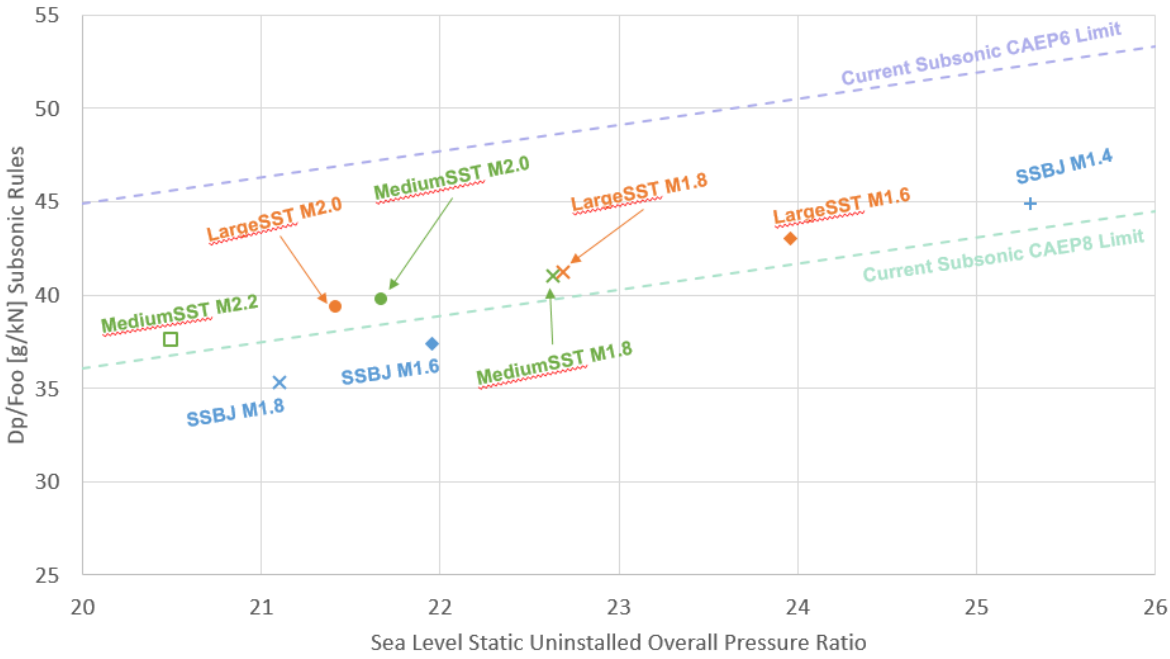

Figure 33. LTO NO_x subsonic rules vs. OPR for selected vehicle designs.

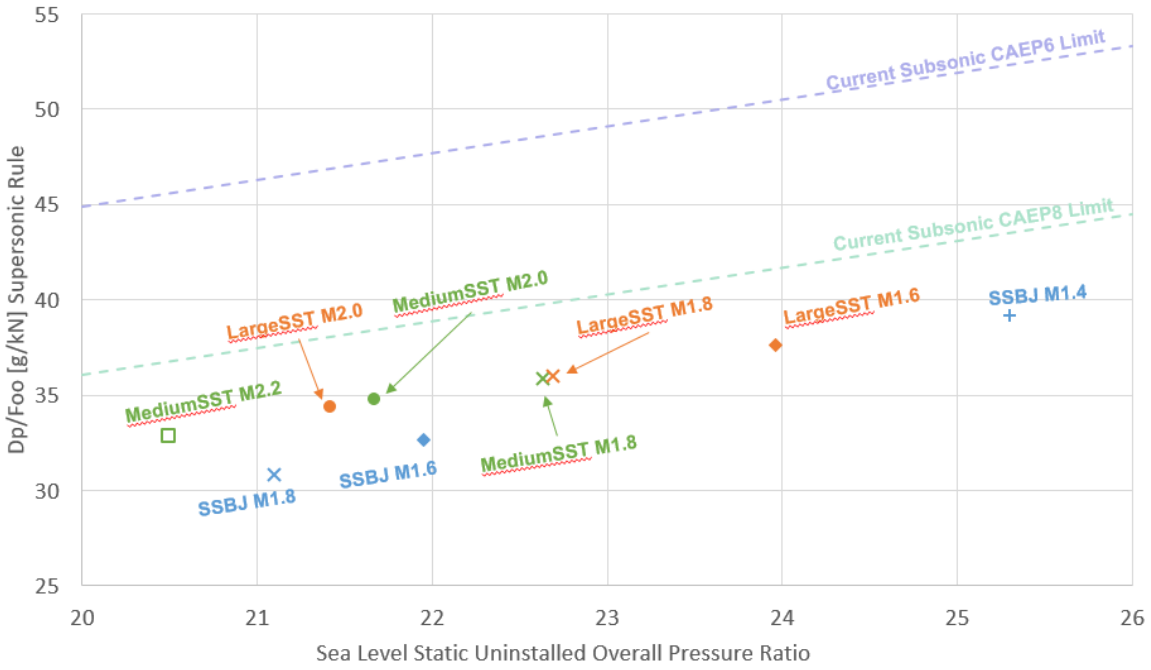

Figure 34. LTO NO_x supersonic rules vs. OPR for selected vehicle designs.

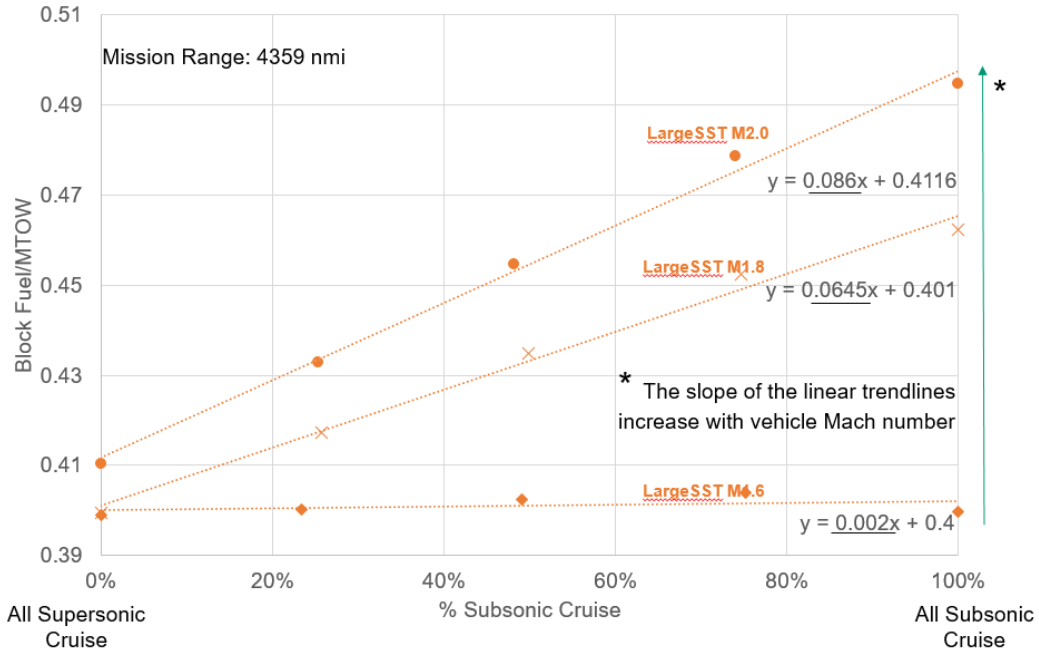

Figure 35. Large SST fuel fraction vs. percentage of cruise subsonic.

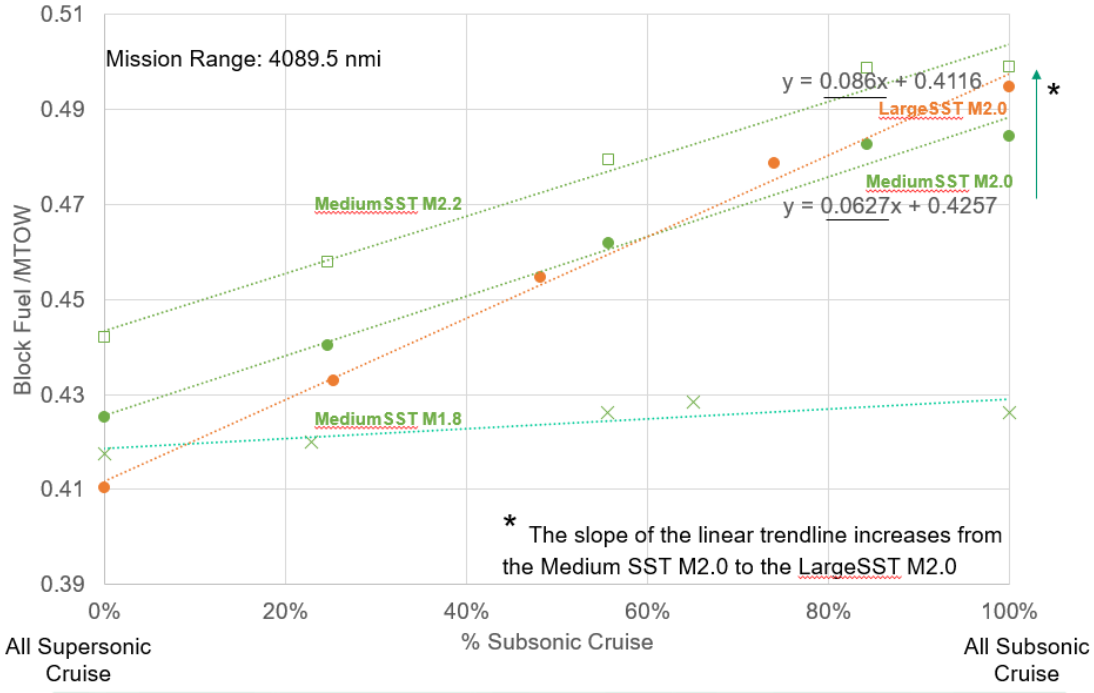

Figure 36. Medium SST fuel fraction vs. percentage of cruise subsonic.

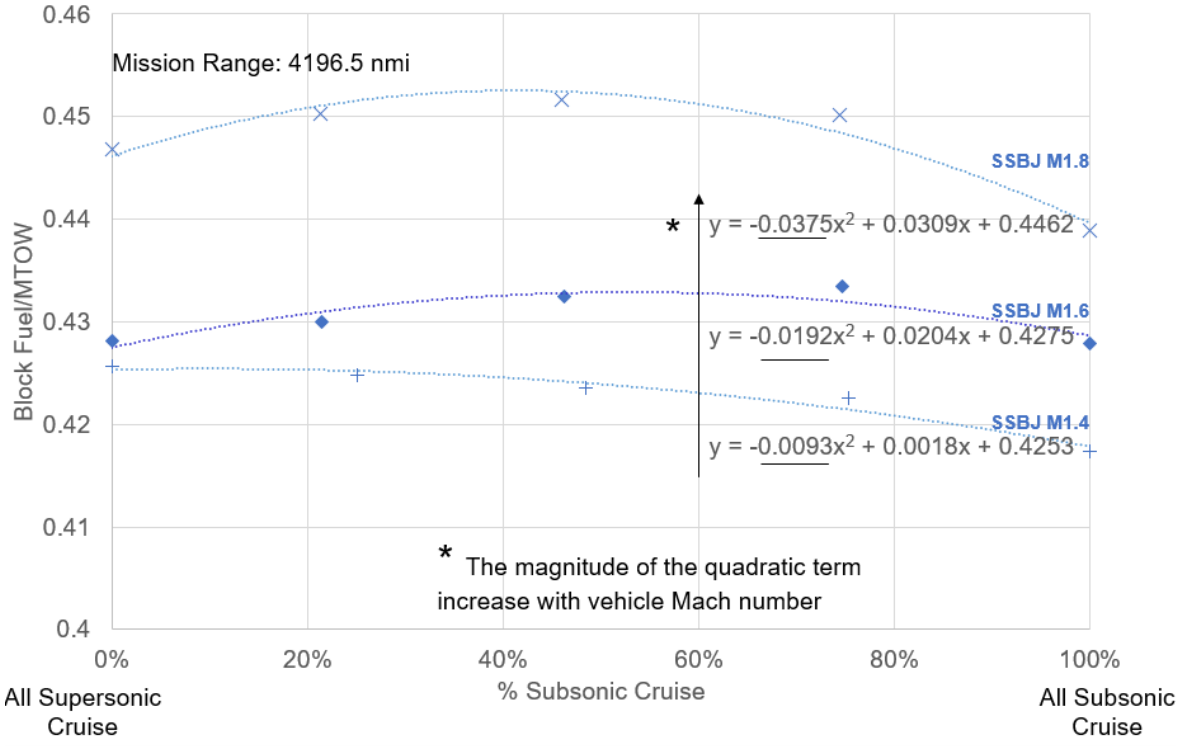

Figure 37. SSBJ fuel fraction vs. percentage of cruise subsonic.

Propulsion Results

Since the last report, the propulsion design has changed because of the inclusion of noise analysis and optimizing primarily for LTO noise. In the previous report, Georgia Tech optimized for fuel burn, constrained by a jet velocity constraint. The results below show the engine performance, dimensions, and weight for the selected vehicle designs, as described in the results of the Design Mach Number Trade Study section. As a result of optimizing primarily for noise, the FPR is much lower than that in the last report to increase the BPR and decrease the jet velocity. Similarly, the throttle ratio is much lower (design turbine inlet temperature higher) to further improve the BPR and low-speed performance. However, specific thrust is sacrificed, thus resulting in a greater loss of thrust with altitude. Consequently, the engine must be oversized at takeoff to have sufficient thrust during the transonic acceleration. Supersonic performance is also sacrificed, because the higher design turbine inlet temperature results in the engine being more severely constrained by the maximum turbine inlet temperature during cruise. The result is an engine that is much heavier and less efficient than is optimal for fuel burn when optimizing primarily for takeoff noise. In addition, as with the whole vehicle, the engine size increases with the Mach number. Furthermore, the OPR tends to decrease with the Mach number, and the FPR tends to increase with the Mach number. The following pages contain a table for each vehicle with metrics grouped by flight condition and then design Mach number. Tables 23–25 show the selected engine designs for the SSBJ, medium SST (55 pax), and large SST (100 pax), respectively. Some metrics do not change with flight conditions for a given design Mach number and may be repeated across flight conditions. The metrics shown in the subsequent tables are defined in Table 22.

Table 22. Propulsion metric description.

Metric	Description
FPR	Fan pressure ratio
BPR	Bypass ratio
OPR	Overall pressure ratio
T3 [R]	High-pressure compressor/combustor entrance total temperature
T4 [R]	Combustor exit total temperature
T41 [R]	High pressure turbine 1st rotor inlet temperature
%Nc Fan	Percentage corrected fan speed
TSFC $\left[\frac{\text{lbm}}{\text{lbf}\cdot\text{h}}\right]$	Thrust-specific fuel consumption
EPR	Engine pressure ratio
NPR	Nozzle pressure ratio
Vjet [ft/s]	Nozzle exit fully expanded jet velocity
LTO NO_x [g/kN] subsonic	Certification LTO NO_x in grams per kN of thrust according to subsonic rules
LTO NO_x [g/kN] supersonic	Certification LTO NO_x in grams per kN of thrust according to supersonic rules
Thrust [lbf]	Installed net thrust
Wc Fan [lbm/s]	Corrected airflow entering the fan
Nozzle Throat Area [in^2]	Flow area of the nozzle throat
Inlet Capture Area [in^2]	Forward projected area of the inlet
Fan Diameter [in]	Diameter of the fan
Engine Length [in]	Length of the installed engine pod
Engine Weight [lbf]	Installed engine weight

Table 23. Eight-PAX engine cycle, performance, dimensions, and weight.

	ADP Mach 1.2/39 kft/ISA			TOC Design Mach/50 kft/ISA			TKO M 0.3/SL/ISA + 18F		
Design Mach	**1.4**	**1.6**	**1.8**	**1.4**	**1.6**	**1.8**	**1.4**	**1.6**	**1.8**
FPR	2.03	2.02	2.03	2.03	1.98	1.70	2.03	2.02	2.03
BPR	3.67	3.44	3.65	3.65	3.49	4.30	3.68	3.45	3.66
OPR	25.16	21.85	20.98	25.07	21.14	15.33	25.17	21.84	20.99
T3 [R]	1371	1314	1298	1480	1512	1482	1474	1414	1397
T4 [R]	2989	2947	3081	3271	3379	3381	3130	3090	3233
T41 [R]	2930	2877	3004	3206	3300	3300	3071	3019	3156
%Nc Fan	100	100	100	100	99	91	100	100	100
TSFC $\left[\frac{\text{lbm}}{\text{lbf·h}}\right]$	0.86	0.89	0.86	0.92	0.97	1.06	0.60	0.61	0.61
EPR	1.82	1.82	1.85	1.82	1.78	1.53	1.82	1.81	1.86
NPR	4.20	4.19	4.28	5.50	7.15	8.23	1.86	1.85	1.90
Vjet [ft/s]	1880	1885	1913	2112	2312	2358	1352	1354	1390
LTO NO_x [g/kN] subsonic	44.87	37.37	35.30	44.87	37.37	35.30	44.87	37.37	35.30
LTO NO_x [g/kN] supersonic	39.17	32.67	30.83	39.17	32.67	30.83	39.17	32.67	30.83
Thrust [lbf]	4621	4905	5658	3583	4989	4857	15504	16985	18760
Wc Fan [lbm/s]	494	540	576	490	532	517	500	547	583
Nozzle Throat Area [in^2]	1084	1192	1257	1081	1199	1289	1087	1196	1264
Inlet Capture Area [in^2]	1966	2240	2297	1966	2240	2297	1966	2240	2297
Fan Diameter [in]	50.7	53.0	54.7	50.7	53.0	54.7	50.7	53.0	54.7
Engine Length [in]	293	313	328	293	313	328	293	313	328
Engine Weight [lbf]	5304	6228	6721	5304	6228	6721	5304	6228	6721

Table 24. Medium SST engine cycle, performance, dimensions, and weight.

	ADP Mach 1.2/39 kft/ISA			TOC Design Mach/55 kft/ISA			TKO M 0.3/SL/ISA + 18F		
Design Mach	**1.8**	**2.0**	**2.2**	**1.8**	**2.0**	**2.2**	**1.8**	**2.0**	**2.2**
FPR	2.02	2.1	2.20	1.73	1.66	1.58	2.02	2.1	2.20
BPR	3.38	2.93	2.59	3.91	3.63	3.44	3.38	2.93	2.58
OPR	22.66	21.70	20.53	17.29	14.41	11.47	22.59	21.64	20.47
T3 [R]	1331	1317	1294	1544	1584	1604	1433	1418	1395
T4 [R]	2994	2957	2954	3382	3384	3385	3173	3138	3137
T41 [R]	2918	2879	2874	3300	3300	3300	3094	3057	3054
%Nc Fan	100	100	100	92	88	83	100	100	100
TSFC $\left[\frac{\text{lbm}}{\text{lbf·h}}\right]$	0.84	0.87	0.90	1.04	1.13	1.25	0.62	0.63	0.64
EPR	1.84	1.93	2.03	1.56	1.50	1.42	1.84	1.93	2.03
NPR	4.35	4.58	4.84	8.36	10.80	13.93	1.89	1.98	2.09
Vjet [ft/s]	1926	1988	2060	2397	2580	2757	1394	1465	1547
LTO NO_x [g/kN] subsonic	41.00	39.76	37.60	41.00	39.76	37.60	41.00	39.76	37.60
LTO NO_x [g/kN] supersonic	35.85	34.79	32.90	35.85	34.79	32.90	35.85	34.79	32.90
Thrust [lbf]	7208	8565	9504	5079	6615	9504	22862	27419	30828
Wc Fan [lbm/s]	695	780	817	629	670	817	703	789	826
Nozzle Throat Area [in^2]	1533	1678	1705	1565	1722	1737	1541	1694	1724
Inlet Capture Area [in^2]	2993	3598	4001	2993	3598	4001	2993	3598	4001
Fan Diameter [in]	60.1	63.7	65.2	60.1	63.7	65.2	60.1	63.7	65.2
Engine Length [in]	538	578	601	538	578	601	538	578	601
Engine Weight [lbf]	9671	11706	13106	9671	11706	13106	9671	11706	13106

Table 25. Large SST engine cycle, performance, dimensions, and weight.

	ADP Mach 1.2/39 kft/ISA			TOC Design Mach/50 kft/ISA			TKO M 0.3/SL/ISA + 18 F		
Design Mach	**1.6**	**1.8**	**2.0**	**1.6**	**1.8**	**2.0**	**1.6**	**1.8**	**2.0**
FPR	2.07	2.08	2.20	1.86	1.75	1.68	2.07	2.08	2.2
BPR	3.74	3.38	2.87	4.14	3.97	3.63	3.73	3.37	2.87
OPR	23.98	22.71	21.45	19.93	16.76	13.57	23.91	22.65	21.39
T3 [R]	1354	1332	1312	1487	1524	1552	1458	1434	1413
T4 [R]	3127	3062	3037	3379	3380	3381	3310	3245	3221
T41 [R]	3052	2987	2959	3300	3300	3300	3233	3167	3141
%Nc Fan	100	100	100	95	92	87	100	100	100
TSFC $\left[\frac{\text{lbm}}{\text{lbf·h}}\right]$	0.82	0.85	0.88	0.96	1.06	1.17	0.61	0.63	0.64
EPR	1.88	1.90	2.02	1.67	1.57	1.52	1.88	1.90	2.02
NPR	4.39	4.45	4.75	6.63	8.30	10.92	1.92	1.94	2.06
Vjet [ft/s]	1931	1960	2043	2229	2397	2594	1406	1434	1530
LTO NO_x [g/kN] subsonic	43.05	41.19	39.36	43.05	41.19	39.36	43.05	41.19	39.36
LTO NO_x [g/kN] supersonic	37.61	36.00	34.41	37.61	36.00	34.41	37.61	36.00	34.41
Thrust [lbf]	9649	10684	11766	7200	8922	10592	30275	33814	37532
Inlet Capture Area [in^2]	3350	3871	4250	3350	3871	4250	3350	3871	4250
Fan Diameter [in]	69.0	72.0	72.7	69.0	72.0	72.7	69.0	72.0	72.7
Wc Fan [lbm/s]	917	998	1017	859	897	859	928	1010	1029
Nozzle Throat Area [in^2]	1983	2162	2124	2024	2221	2188	1997	2179	2147
Engine Length	546	579	595	546	579	5955	546	579	595
Engine Weight	12470	13979	15293	12470	13979	15293	12470	13979	15293

NASA STCA Engine Emissions Results

The supersonic engine data for the NASA STCA engine was provided by Mr. Jeff Berton at NASA Glenn Research Center. The normalized results are presented in the following tables.

Table 26. NASA STCA nvPM, subsonic LTO cycle.

	TO (100%)	C_L (85%)	AP (30%)	ID (7%)
Normalized EI Mass	1.0000	0.5942	0.0223	0.0197

Table 27. NASA STCA nvPM, Supersonic LTO cycle.

	TO (100%)	C_L (65%)	DE (15%)	AP (34%)	ID (5.8%)
Normalized EI Mass	1.0000	0.2318	0.0205	0.0285	0.0197

Boom Engine Emissions Results

The supersonic engine data for the Boom engine were generated from the Boom engine NPSS model run by Georgia Tech. The normalized results are presented in the following tables.

Table 28. Boom nvPM, subsonic LTO cycle.

	TO (100%)	C_L (85%)	AP (30%)	ID (7%)
Normalized EI Mass	1.0000	0.4503	0.1205	0.1472

Table 29. Boom nvPM, supersonic LTO cycle.

	TO (100%)	C_L (65%)	DE (15%)	AP (34%)	ID (5.8%)
Normalized EI Mass	1.0000	0.1769	0.1487	0.1185	0.1528

Gulfstream Engine Emissions Results

Two different estimates for the Gulfstream engine were available, generated from NPSS models developed by ASDL. The second model had lower thrust but higher T3 and P3 than the first model. The normalized results are presented in the following tables.

Table 30. Gulfstream nvPM, subsonic LTO cycle No. 1.

	TO (100%)	C_L (85%)	AP (30%)	ID (7%)
Normalized EI Mass	1.0000	0.7310	0.3457	0.1447

Table 31. Gulfstream nvPM, supersonic LTO cycle No. 1.

	TO (100%)	C_L (65%)	DE (15%)	AP (34%)	ID (5.8%)
Normalized EI Mass	1.0000	0.2085	0.3089	0.1936	0.1306

Table 32. Gulfstream nvPM, subsonic LTO cycle No. 2.

	TO (100%)	C_L (85%)	AP (30%)	ID (7%)
Normalized EI Mass	1.0000	0.8401	0.2236	0.1422

Table 33. Gulfstream nvPM, supersonic LTO cycle No. 2.

	TO (100%)	C_L (65%)	DE (15%)	AP (34%)	ID (5.8%)
Normalized EI Mass	1.0000	0.5026	0.2012	0.1905	0.1328

Airframe Aerodynamic Results

This section presents planform views of the optimized vehicles, with pressure coefficient contours overlaid, as well as drag polars and L/D trends at 55,000 ft for the 100- pax (Figures 38–40) and 55-pax (Figures 41–43) aircraft, and SSBJ (Figures 44–46). Table 34 captures all designs and also shows the optimized vehicles at off-design Mach numbers. A decrease in peak L/D with Mach number is observed, which is consistent with the physics. In addition, the peak L/D decreases with passenger class, probably because of a reduction in the wing planform area as the vehicle size reduces. The exception to this rule is the SSBJ; however, the highly swept wings for this concept are likely to provide a high-speed L/D benefit that counteracts the smaller planform area. The design space selected appears to have been overly constrained, particularly by the trailing edge sweep bounds. As such, most planforms ultimately appear similar across vehicles. The SSBJ in contrast, with a different baseline and variable bounds, shows a noticeable change in wing sweep as the Mach number is increased, thus justifying the conclusion of a narrow design space for the other vehicles.

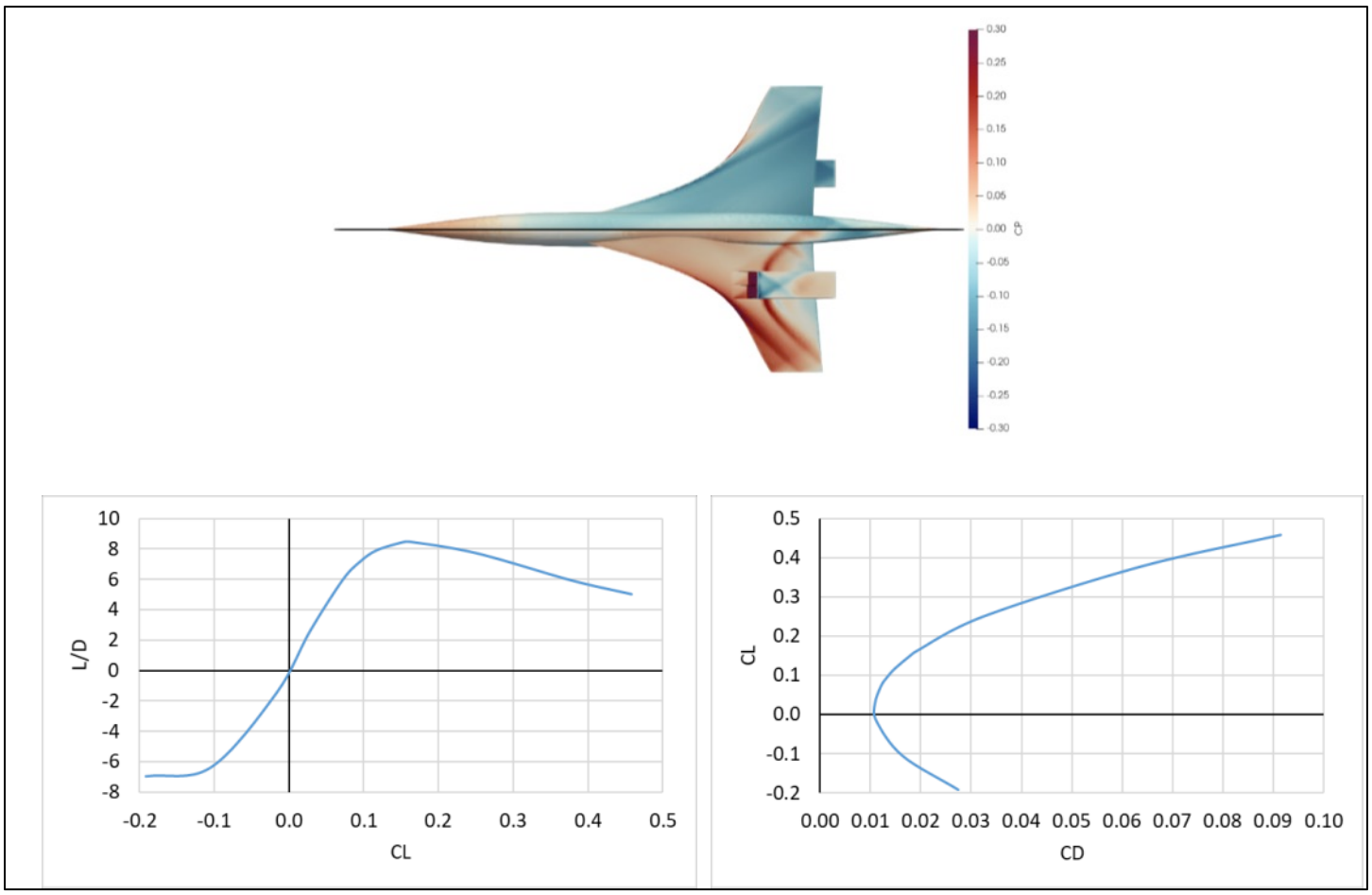

Figure 38. Large SST Mach 1.6 design at Mach 1.6/55,000 ft (peak L/D = 8.46 at C_L = 0.162).

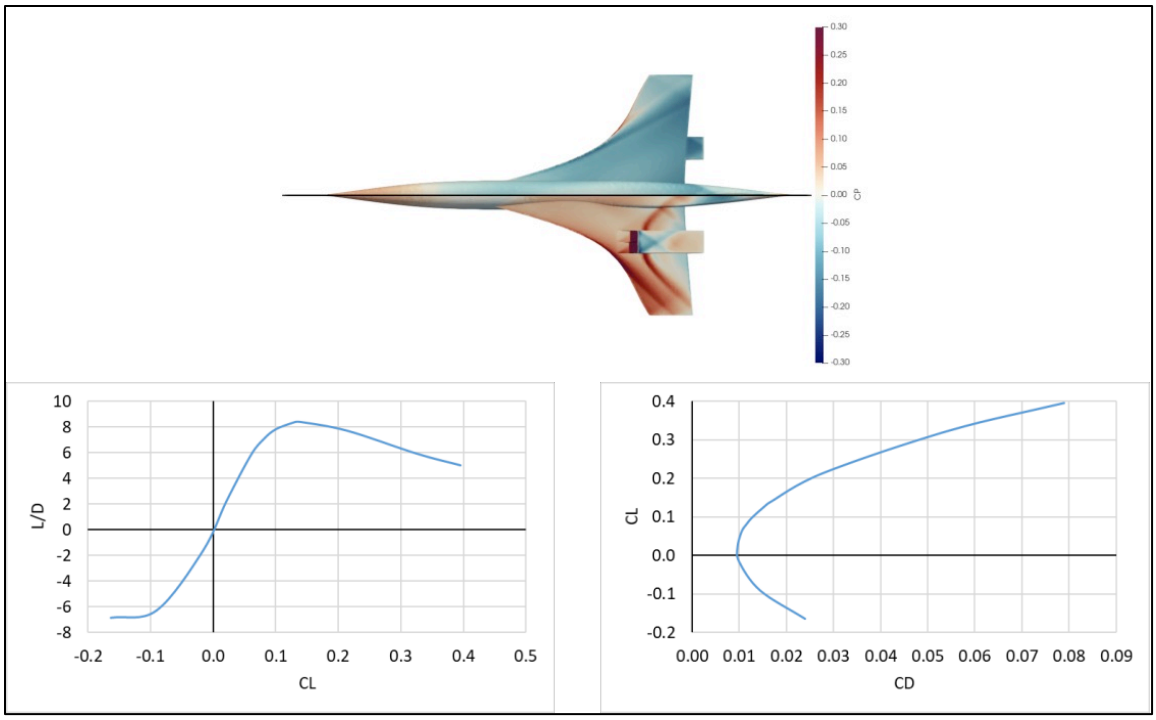

Figure 39. Large SST Mach 1.8 design at Mach 1.8/55,000 ft (peak L/D = 8.39 at C_L = 0.138).

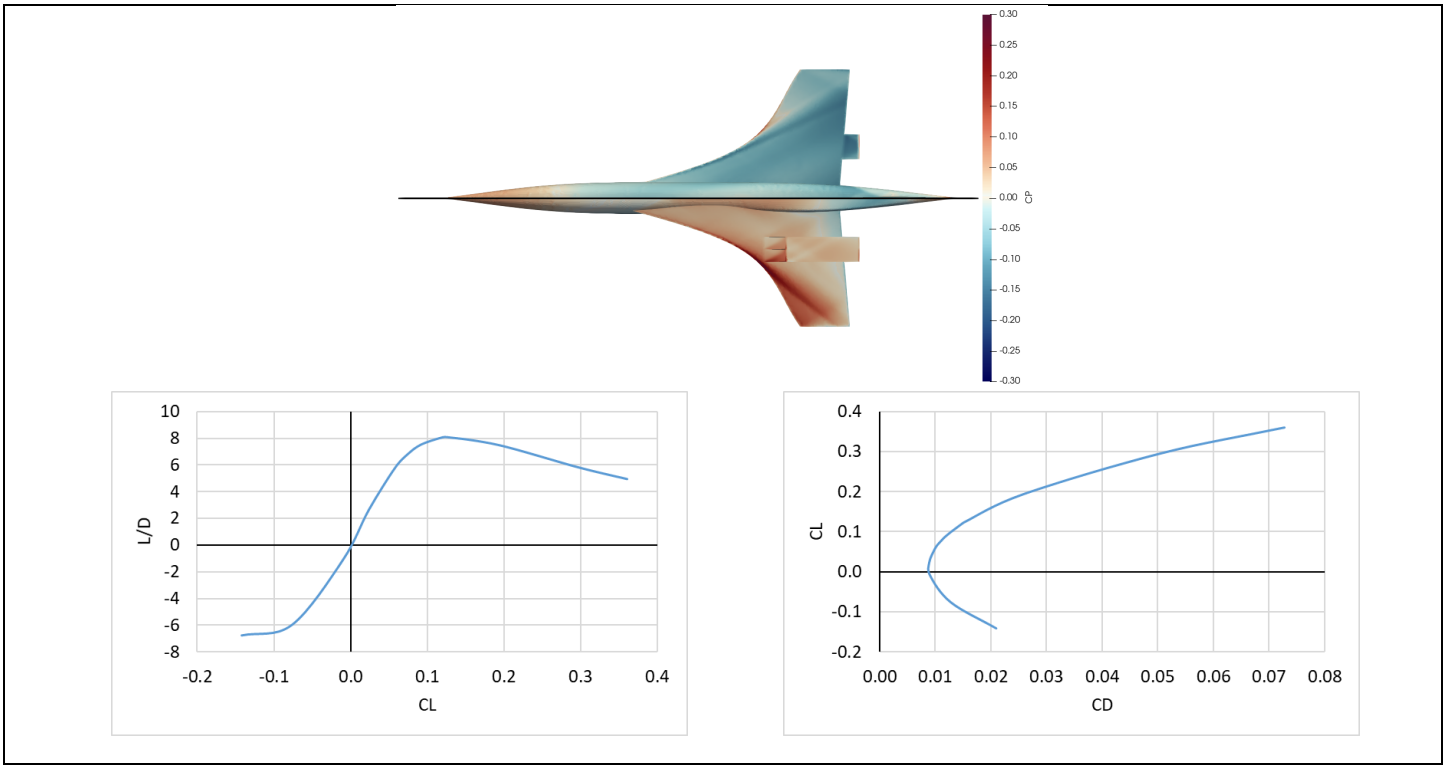

Figure 40. Large SST Mach 2.0 design at Mach 2.0/55,000 ft (peak L/D = 8.09 at C_L = 0.126).

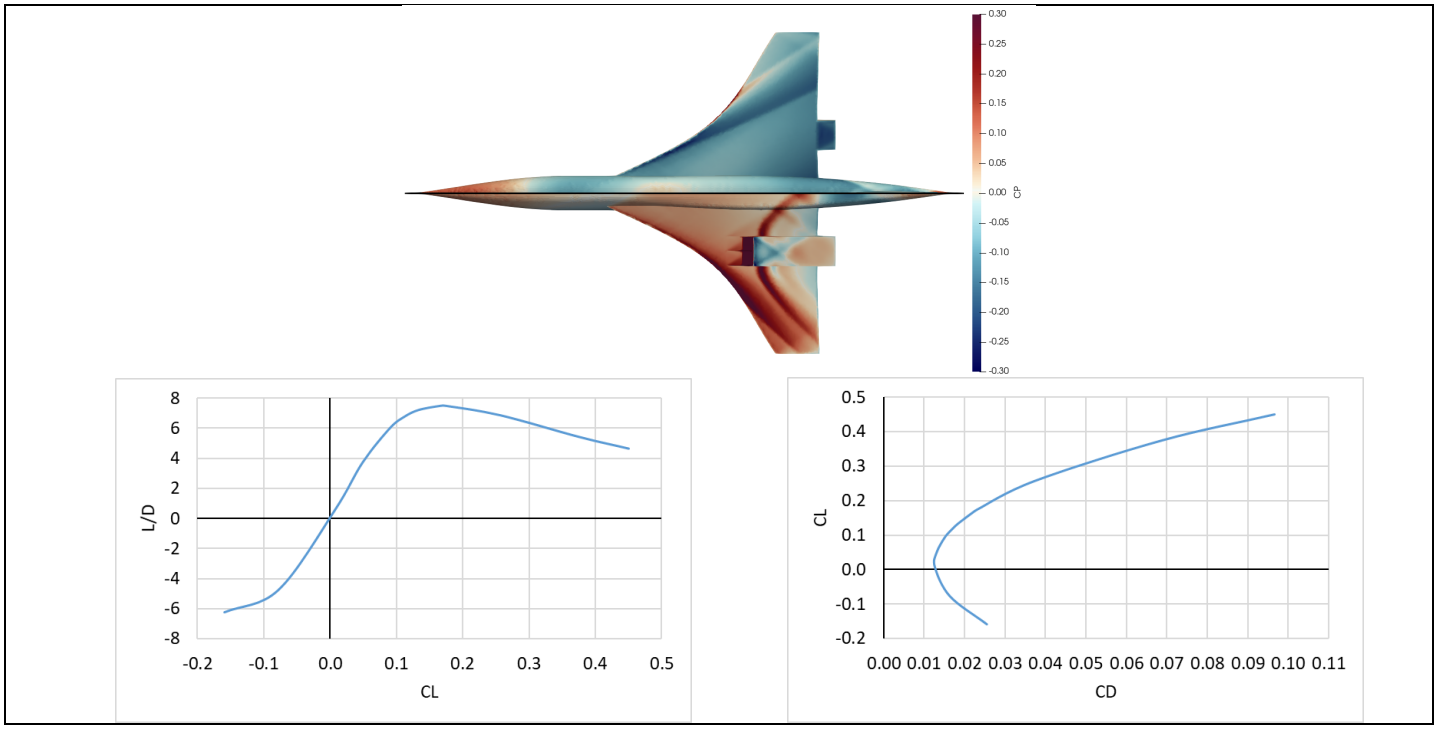

Figure 41. Medium=SST Mach 1.8 design at Mach 1.8/55,000 ft (peak L/D = 7.51 at C_L = 0.174).

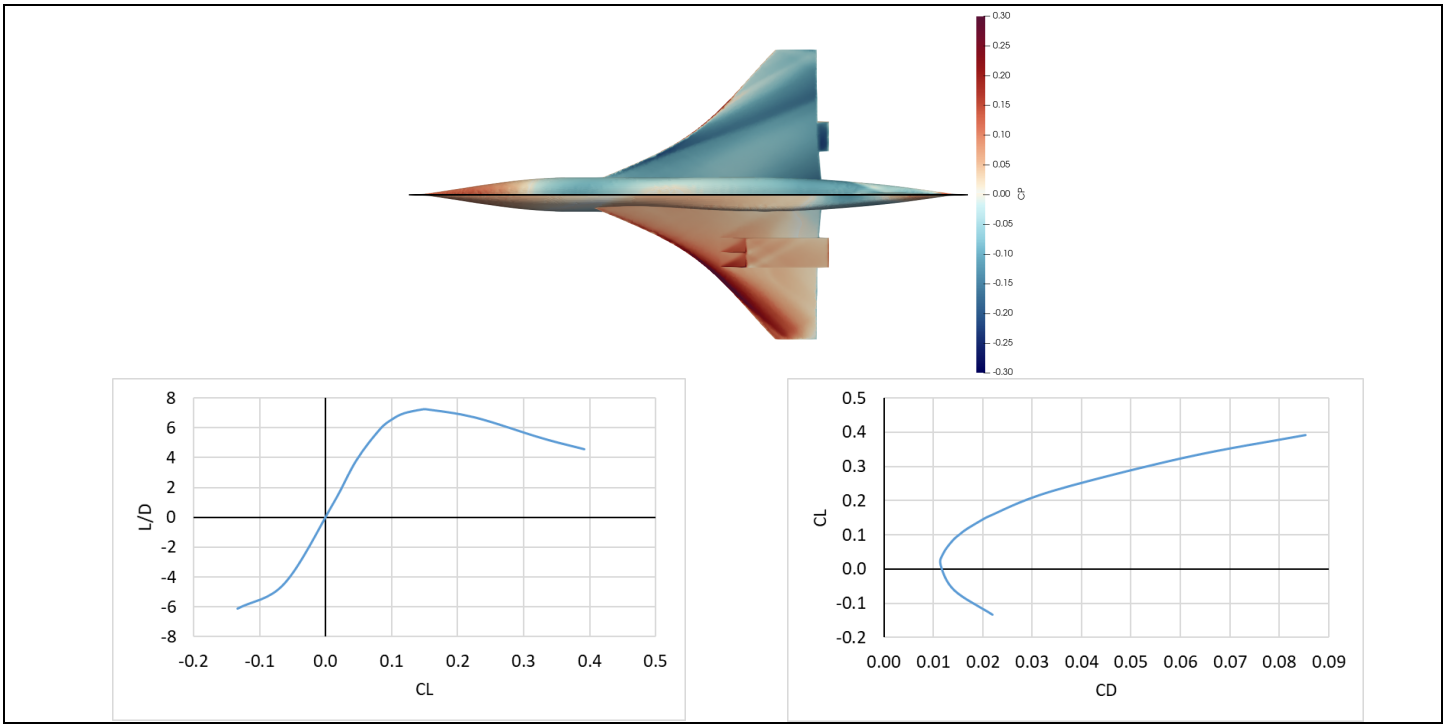

Figure 42. Medium SST Mach 2.0 design at Mach 2.0/55,000 ft (peak L/D = 7.26 at C_L = 0.153).

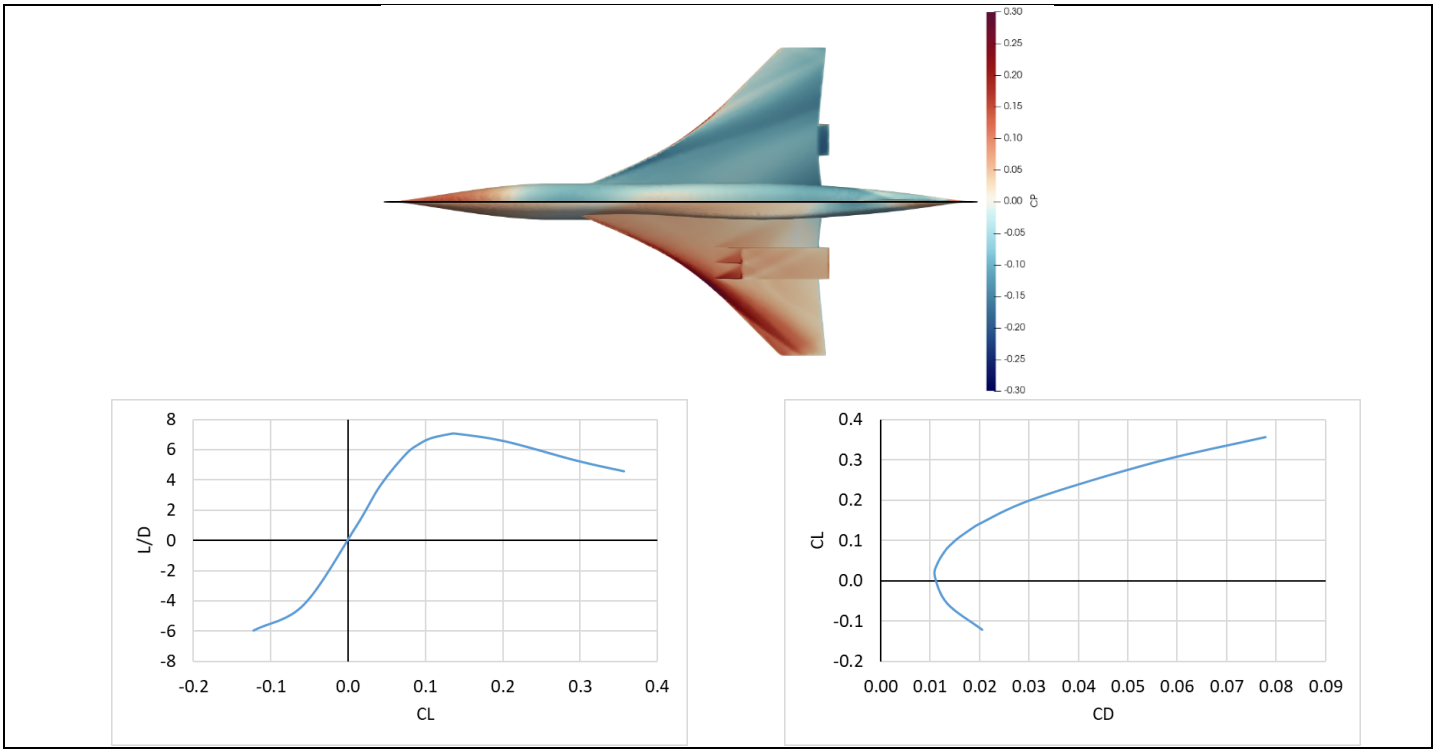

Figure 43. Medium SST Mach 2.2 design at Mach 2.2/55,000 ft (peak L/D = 7.07 at C_L = 0.139).

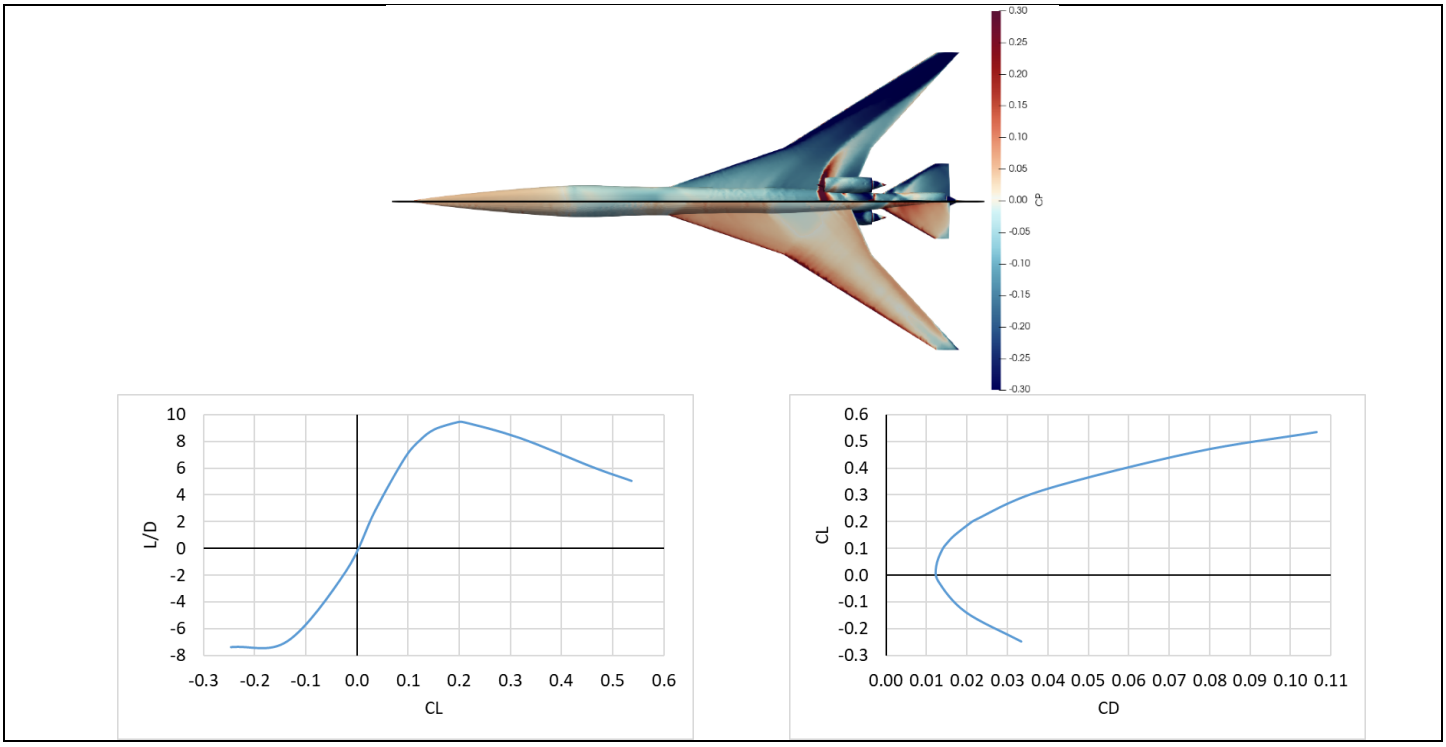

Figure 44. SSBJ Mach 1.4 design at Mach 1.4/55,000 ft (peak L/D = 9.41 at C_L = 0.209).

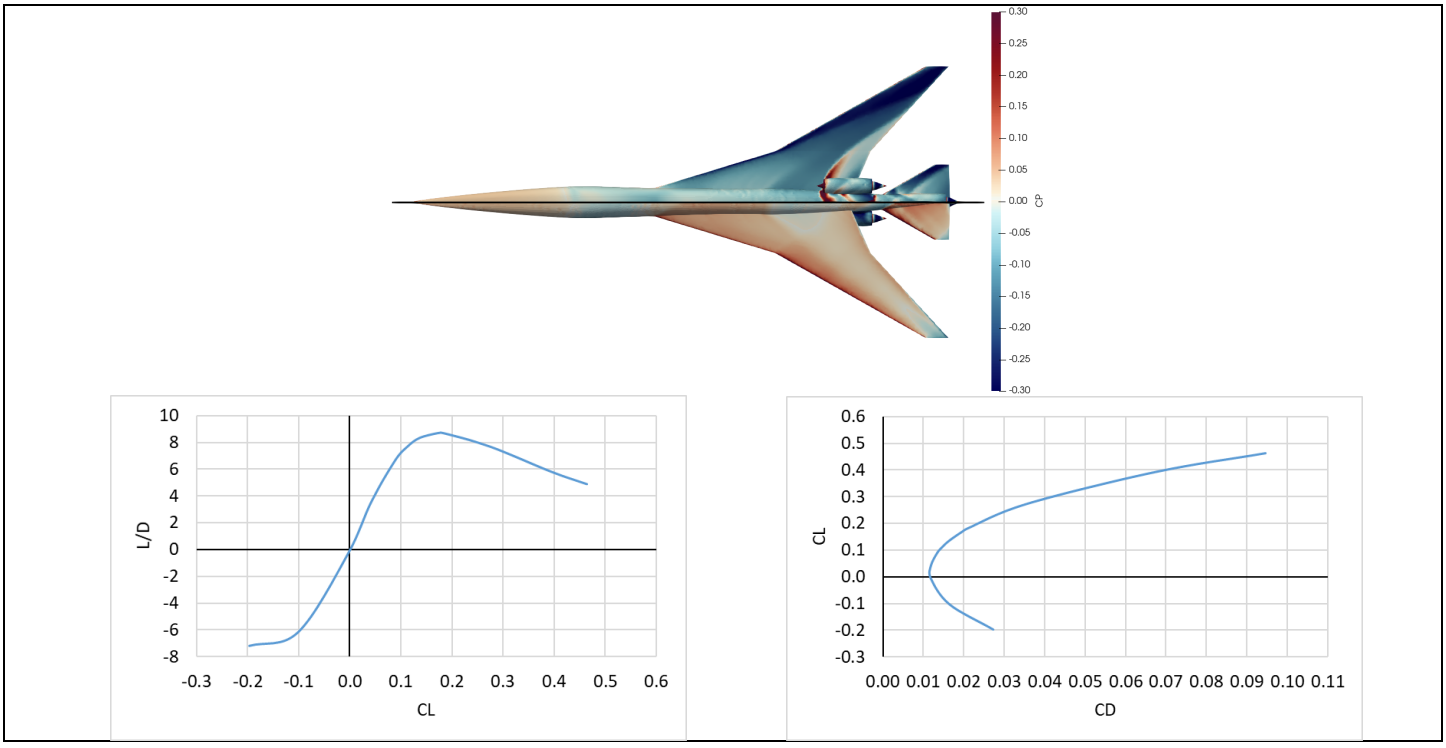

Figure 45. SSBJ Mach 1.6 design at Mach 1.6/55,000 ft (peak L/D = 8.72 at C_L = 0.172).

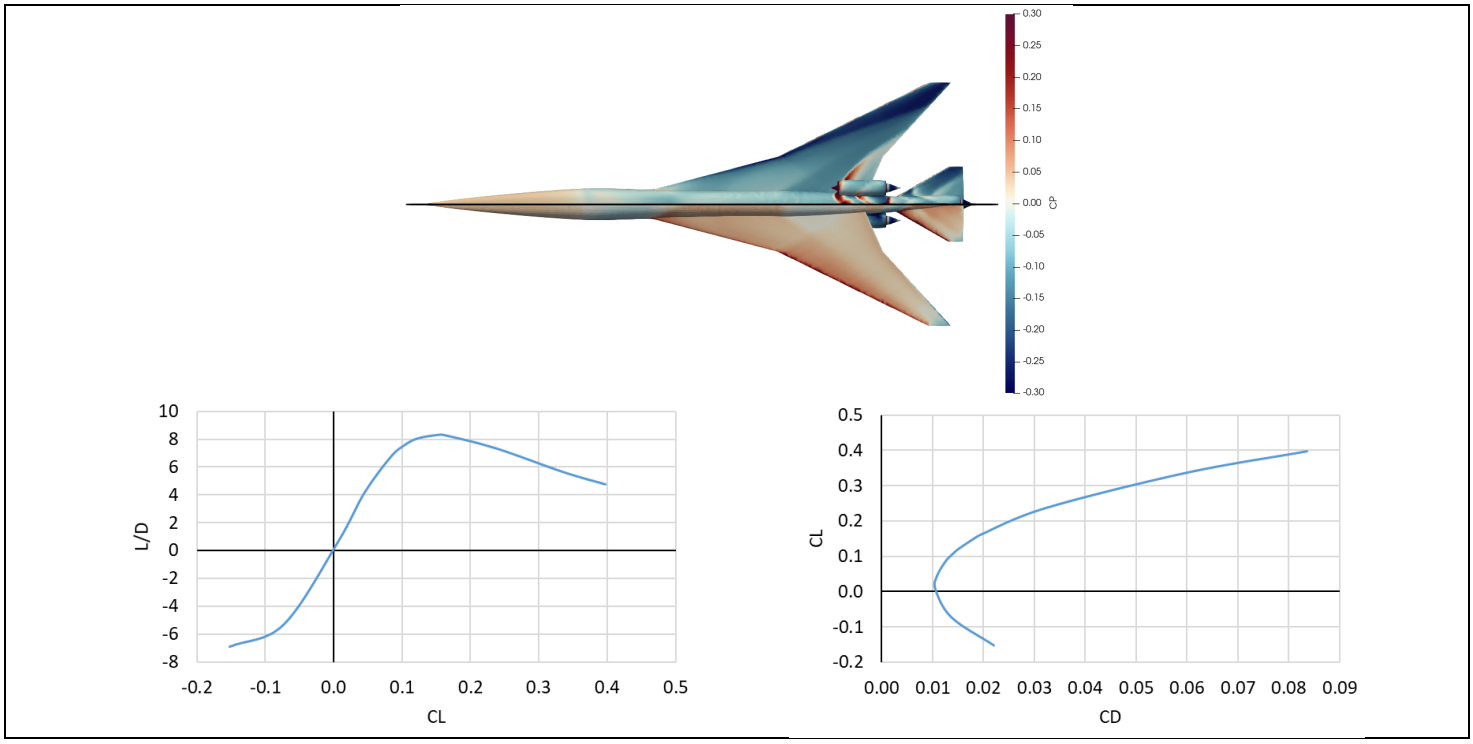

Figure 46. SSBJ Mach 1.8 design at Mach 1.8/55,000 ft (peak L/D = 8.29 at C_L = 0.153).

Table 34. Table of optimum designs with maximum L/D (as computed by **CART3D**) and surface pressure coefficients shown for an altitude of 55,000 ft.

	$M_\infty = 1.4$	$M_\infty = 1.6$	$M_\infty = 1.8$	$M_\infty = 2.0$	$M_\infty = 2.2$
Large SST		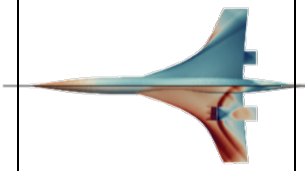 *Max L/D = 8.46*	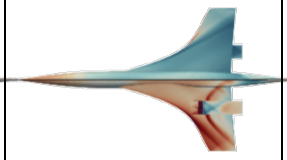 *Max L/D = 8.39*	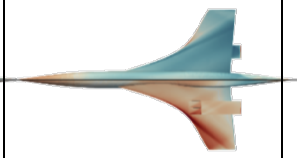 *Max L/D = 8.09*	
Medium SST			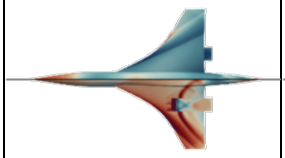 *Max L/D = 7.51*	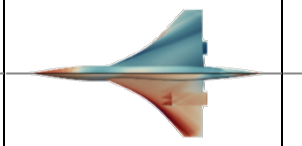 *Max L/D = 7.26*	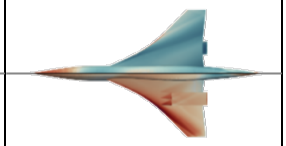 *Max L/D = 7.07*
SSBJ	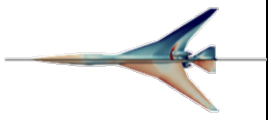 *Max L/D = 9.41*	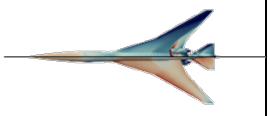 *Max L/D = 8.72*	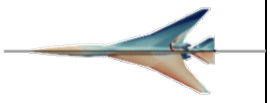 *Max L/D = 8.29*		

Mission Analysis/Vehicle Sizing Results

The vehicle sizing results for all nine vehicles are summarized in Table 35, and the associated aircraft component weight breakdowns are also summarized in Table 36. In addition, Figures 47–49 summarize the resulting mission profiles for each SST class.

Table 35. Summary of SST sizing results.

	SSBJ (8 pax)			Medium SST (55 pax)			Large SST (100 pax)		
	Mach 1.4	**Mach 1.6**	**Mach 1.8**	**Mach 1.8**	**Mach 2.0**	**Mach 2.2**	**Mach 1.6**	**Mach 1.8**	**Mach 2.0**
Design Range (nmi)	4,240	4,240	4,240	4,500	4,500	4,500	5,000	5,000	5,000
Payload (Passengers)	8	8	8	55	55	55	100	100	100
Maximum takeoff weight (lbs)	116,371	128,825	140,070	231,554	275,256	310,752	350,735	374,313	411,435
OEW (lbs)	57,922	63,449	66,760	96,453	113,926	124,369	141,928	151,371	162,172
Fuel Weight (lbs)	56,767	63,697	71,630	123,550	149,780	174,884	187,807	201,942	228,263
Block Fuel (lbs)	49,591	55,904	63,358	109,567	132,728	155,453	167,771	179,658	203,466
Block Time (hr)	5.85	5.23	4.68	5.00	4.60	4.31	6.08	5.49	5.07
T/W	0.469	0.464	0.468	0.420	0.420	0.415	0.365	0.380	0.380
W/S	77	74	76	101	102	106	102	102	105
TOFL (ft)	6,409	6,440	6,695	7,527	7,710	7,996	8,684	8,359	8,523
LDFL (ft)	5,346	5,044	4,781	7,747	7,601	7,619	7,730	7,645	7,618
Vapp (kts)	151.2	147.7	147.2	164.9	164.3	164.5	164.9	164.6	164.7
Wing Area (ft^2)	1,609	1,733	1,838	2,293	2,699	2,932	3,439	3,670	3,918
Sized Thrust (lbf)	18,199	19,924	21,874	24,313	28,902	32,241	32,005	35,560	39,085
Aspect Ratio	3.26	2.72	2.18	2.75	2.25	2.25	2.70	2.35	2.25

Table 36. Summary of SST weight breakdown.

	SSBJ			Medium SST			Large SST		
	M1.4	M1.6	M1.8	M1.8	M2.0	M2.2	M1.6	M1.8	M2.0
WING	12,614	13,991	14,852	17,667	19,828	22,736	31,689	33,491	37,163
HORIZONTAL TAIL	681	856	950	-	-	-	-	-	-
VERTICAL TAIL	630	718	722	253	346	396	338	375	419
VERTICAL FIN	-	-	-	-	-	-	-	-	-
CANARD	-	-	-	-	-	-	-	-	-
FUSELAGE	8,832	8,832	8,832	18,972	18,972	18,972	27,393	27,393	27,393
LANDING GEAR	4,746	5,147	5,393	2,521	8,461	9,250	11,224	11,881	12,624
NACELLE (AIR INDUCTION)	-	-	-	-	-	-	-	-	-
STRUCTURE TOTAL	*27,504*	*29,544*	*30,749*	*39,414*	*47,607*	*51,254*	*70,643*	*73,140*	*77,599*
ENGINES	15,914	18,682	20,163	38,675	46,830	52,443	49,893	55,942	61,200
THRUST REVERSERS	-	-	-	-	-	-	-	-	-
MISCELLANEOUS SYSTEMS	21	22	23	163	178	188	187	197	207
FUEL SYSTEM-TANKS AND PLUMBING	1,854	2,075	2,312	1,917	2,221	2,510	2,348	2,549	2,836
PROPULSION TOTAL	*17,789*	*20,779*	*22,498*	*40,755*	*49,230*	*55,141*	*52,428*	*58,688*	*64,243*
SURFACE CONTROLS	1,062	1,239	1,341	2,433	2,692	3,091	1,583	1,675	1,858
AUXILIARY POWER	459	459	459	706	706	706	903	903	903
INSTRUMENTS	528	564	599	863	910	954	990	1,050	1,107
HYDRAULICS	868	947	1,004	1,652	1,790	1,894	2,278	2,412	2,546
ELECTRICAL	2,094	2,094	2,094	2,713	2,713	2,713	3,157	3,157	3,157
AVIONICS	1,130	1,130	1,130	1,329	1,329	1,329	1,556	1,556	1,556
FURNISHINGS AND EQUIPMENT	3,397	3,397	3,397	-	-	-	-	-	-
AIR CONDITIONING	1,195	1,352	1,509	2,827	3,131	3,434	3,343	3,746	4,149
ANTI-ICING	150	158	163	125	132	140	162	167	170
SYSTEMS AND EQUIPMENT TOTAL	*10,885*	*11,343*	*11,698*	*12,650*	*13,404*	*14,262*	*13,973*	*14,666*	*15,446*
WEIGHT EMPTY	*56,179*	*61,666*	*64,945*	*92,829*	*110,241*	*120,657*	*137,044*	*146,494*	*157,288*
CREW AND BAGGAGE-FLIGHT,	450	450	450	450	450	450	450	450	450
-CABIN,	155	155	155	310	310	310	310	310	310
UNUSABLE FUEL	647	678	700	806	863	901	943	973	1,010
ENGINE OIL	252	268	284	233	260	279	278	298	317
PASSENGER SERVICE	240	232	226	1,486	1,452	1,421	2,203	2,146	2,096
CARGO CONTAINERS	-	-	-	350	350	350	700	700	700
OPERATING WEIGHT	*57,922*	*63,449*	*66,760*	*96,453*	*113,926*	*124,369*	*141,928*	*151,371*	*162,171*
PASSENGERS	1,440	1,440	1,440	9,900	9,900	9,900	18,000	18,000	18,000
PASSENGER BAGGAGE	240	240	240	1,650	1,650	1,650	3,000	3,000	3,000
CARGO	-	-	-	-	-	-	-	-	-
ZERO FUEL WEIGHT	*59,502*	*65,129*	*68,440*	*108,003*	*125,476*	*135,919*	*162,928*	*172,371*	*183,171*
MISSION FUEL	56,769	63,697	71,630	123,550	149,780	174,834	187,807	201,942	228,248
RAMP (GROSS) WEIGHT	*116,371*	*128,825*	*140,070*	*231,554*	*275,256*	*310,752*	*350,735*	*374,313*	*411,419*

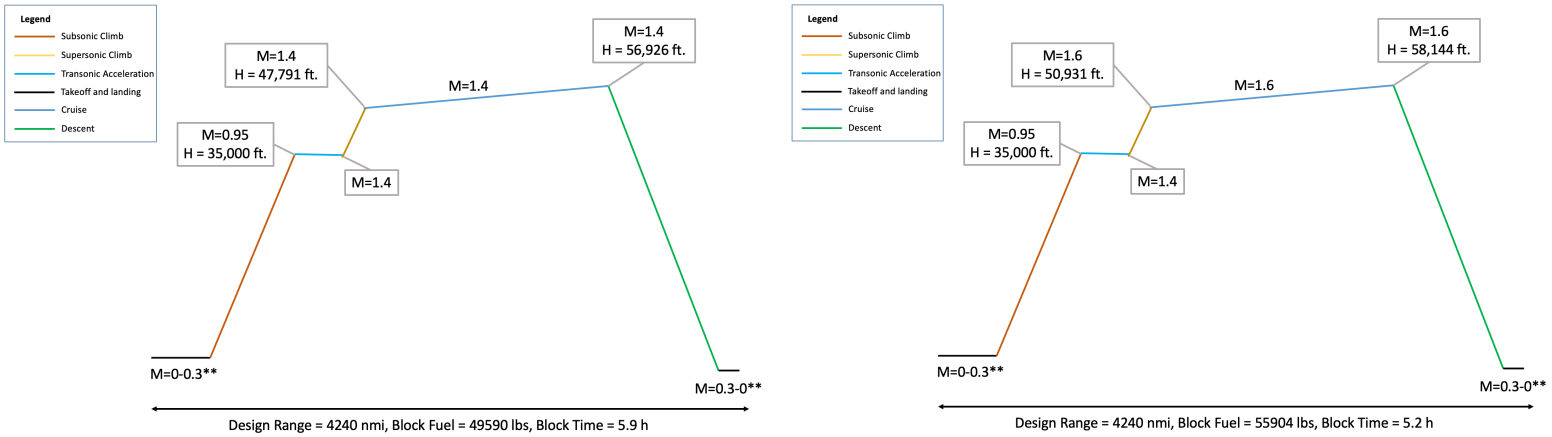

Figure 47. Summary of SSBJ mission profiles.

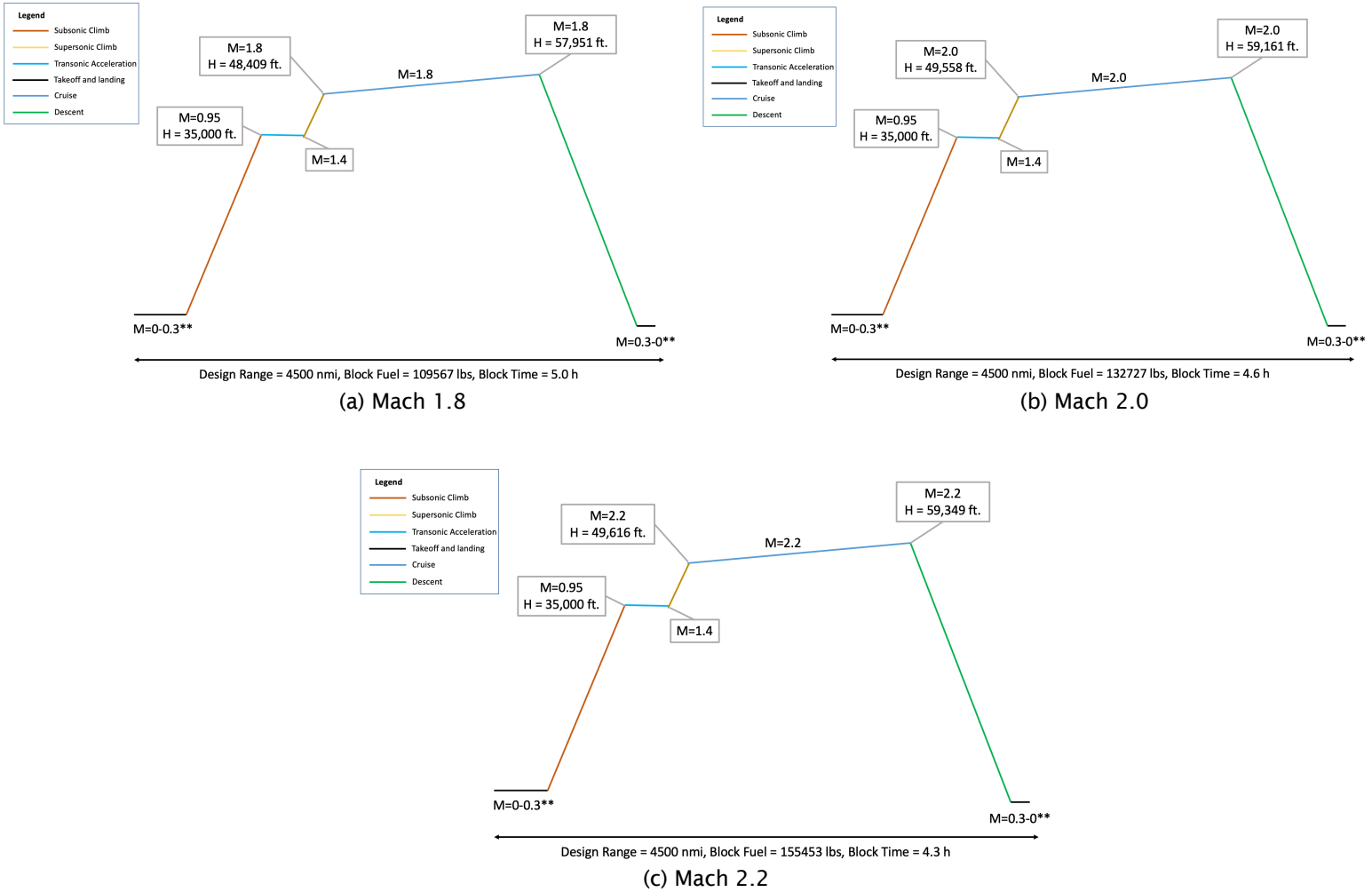

Figure 48. Summary of medium SST mission profiles.

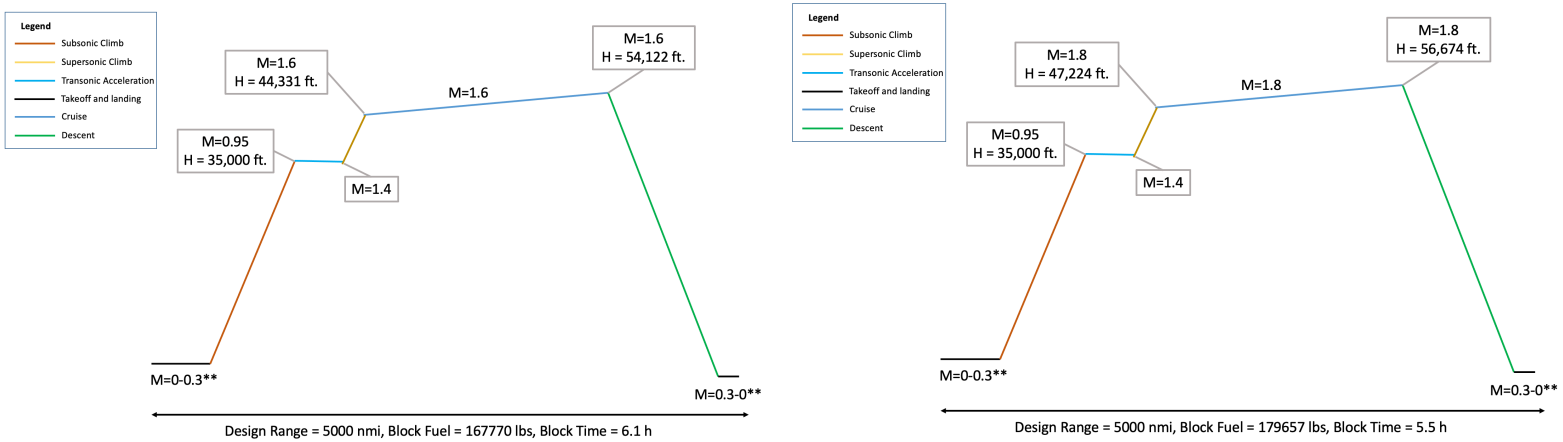

Figure 49. Summary of large SST mission profiles.

Noise Analysis Results

For the takeoff noise analysis, the accumulated data resulting from the DoEs were filtered to include the relevant parameters, i.e., the trajectory variables and the noise values (and corresponding noise margins) associated with each configuration. Although the following analysis focuses on the five main variables described in the Methodology section, many other variables were also included to help assessing the validity of the design point. A collection of viable design points can be seen in Figure 50 where each point represents a simulated configuration and is colored by the total cumulative noise margin for visualization purposes.

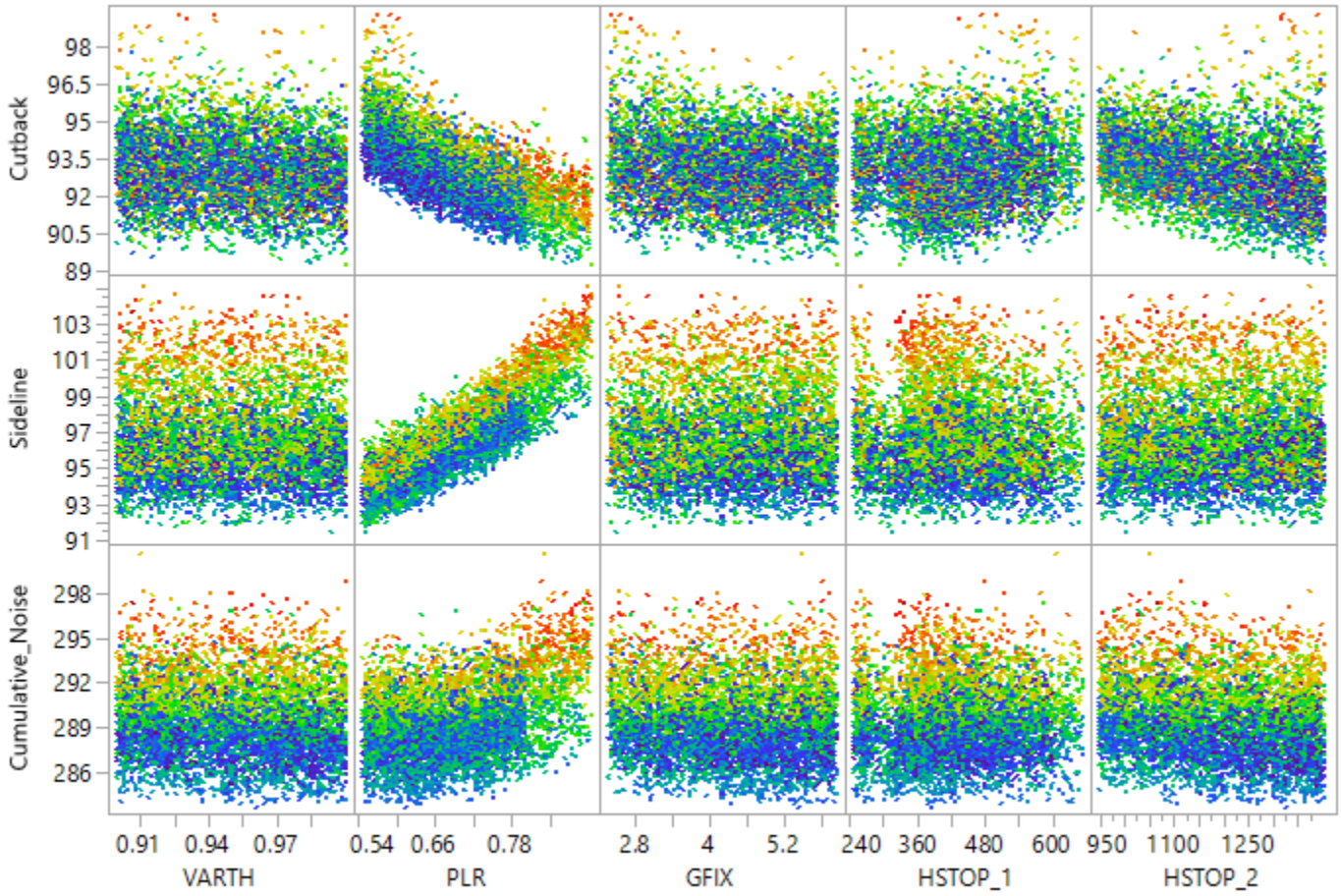

Figure 50. Takeoff noise DoE visualization.

The next step in the analysis is to fit a predictive model (e.g., a neural net) over the data. This process enables use of a prediction profiler, similar to that shown in Figure 51, to a setting for the trajectory variables with the optimal noise configuration. In the present study, the optimal condition was set to a weighted minimum noise, taking the cutback and sideline components into consideration but relying heavily on the total cumulative noise.

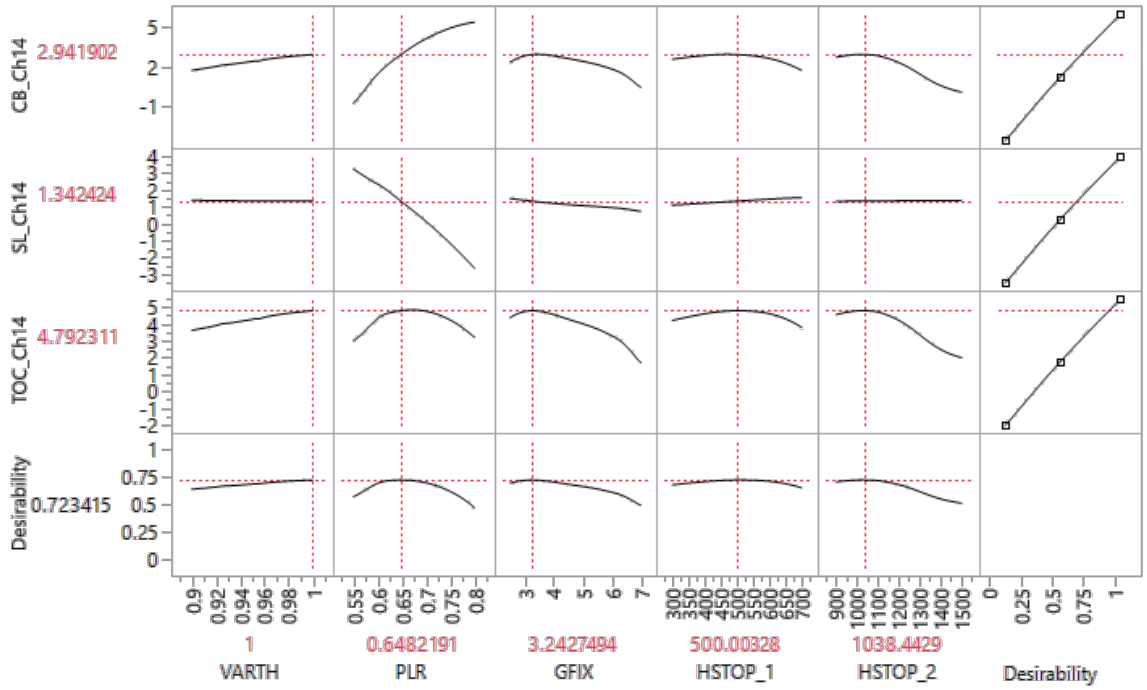

Figure 51. Takeoff noise prediction profiler.

Repeating this process for each aircraft's design Mach number configuration yielded the values shown in Table 37.

Table 37. Takeoff trajectory variable values.

Aircraft	Design Mach	VARTH	PLR	GFIX	HSTOP_1	HSTOP_2
100 PAX	1.6	1.0	0.720	5.51	532.39	1479.58
	1.8	1.0	0.703	5.40	646.48	1371.83
	2.0	1.0	0.717	5.58	416.90	1416.20
55 PAX	1.8	1.0	0.561	6.39	429.58	1536.62
	2.0	1.0	0.613	5.37	405.63	1517.61
	2.2	1.0	0.633	6.21	598.59	1572.54
SSBJ	1.4	1.0	0.739	3.45	512.68	1314.79
	1.6	1.0	0.739	3.45	512.68	1314.79
	1.8	1.0	0.763	2.50	480.00	1150.00

The final variable values from the Noise DoE cases were selected to minimize total noise EPNdB and maximize noise margin. The values selected are shown in Figure 13 under the Mach study section. Figures 52–54 show the contributions of the airframe and each major engine component to the total noise. For each aircraft, for approach airframe noise significantly contributes due to the landing gear, but is negligible for cutback and sideline. Additionally, for cutback and sideline for each aircraft, the jet, exhaust, and core noise are the most dominate noise sources.

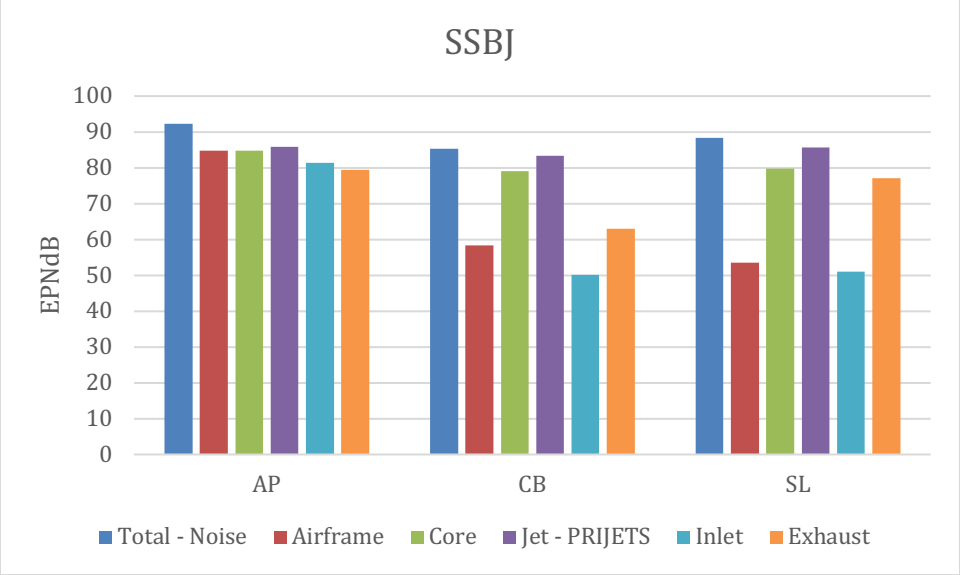

Figure 52. Component noise breakdown for the SSBJ, Mach 1.4.

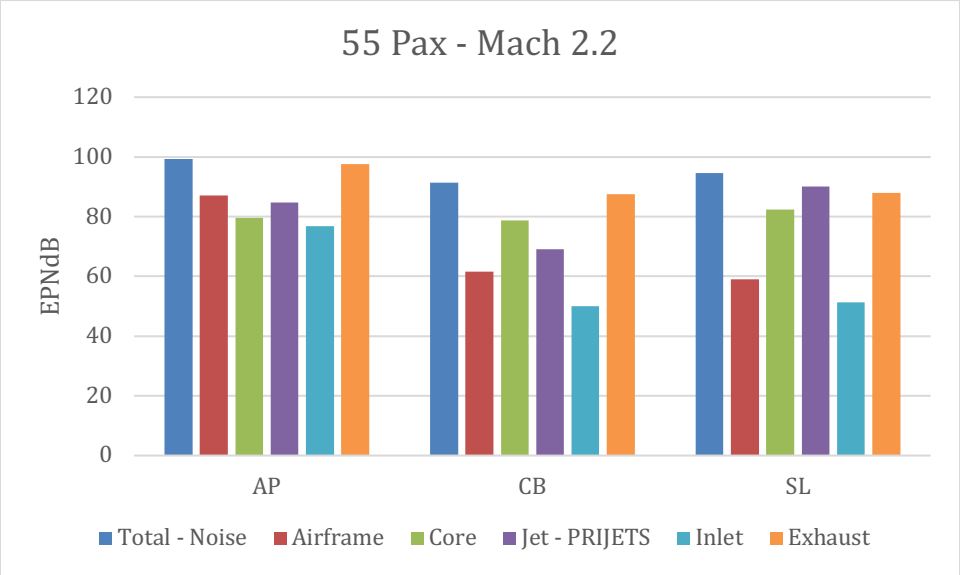

Figure 53. Component noise breakdown for the 55-Pax, Mach 2.2.

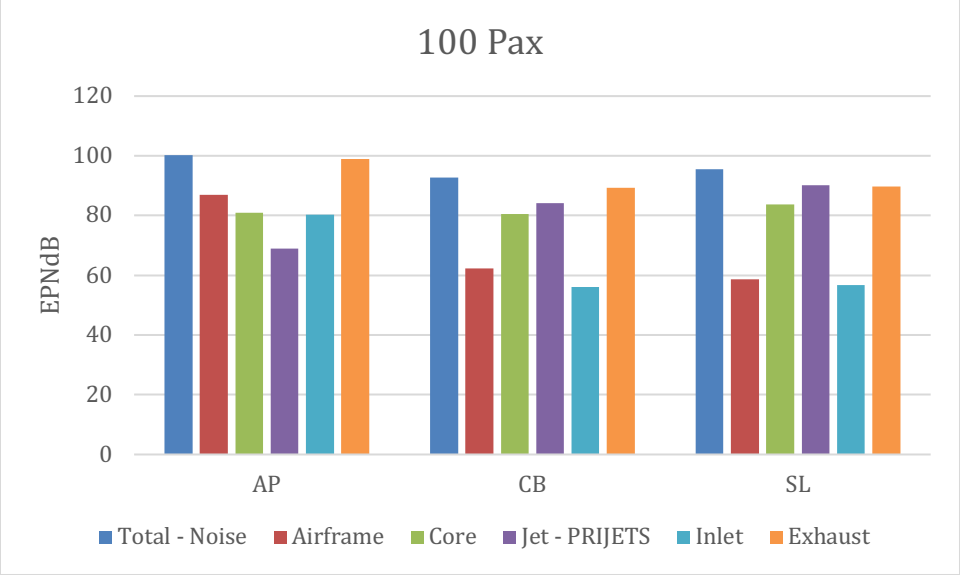

Figure 54. Component noise breakdown for the 100- Pax, Mach 1.8.

Task 5 - SST Modeling in AEDT

Georgia Institute of Technology

Objectives

The primary objective of this task is to develop a method to construct regression models that accurately predict the propulsive performance and aerodynamic characteristics of SST aircraft. In addition, the GT team will validate and provide an implementation plan for the developed approach within AEDT.

Research Approach

Propulsion Regressions

To generate coefficients for net thrust and fuel consumption for each SST concept, the engine deck data are regressed by using a 5th order least-squares linear regression through JMP. In this case, net thrust and fuel flow are both regressed against static pressure ratio, total temperature ratio, Mach number, and power code (δ_s, θ_t, M, and PC, respectively). This process results in two regression equations with 31 coefficients (the unknowns) plus the intercept. For the sake of simplicity and efficient implementation within AEDT, both net thrust and fuel flow have the same regression equation form. An example of the regression equation is shown below.

$$R = a_0 + a_1 * \mathrm{M} + a_2 * \mathrm{M}^2 + a_3 * \mathrm{M}^3 + a_4 * \mathrm{M}^4 + a_5 * \mathrm{M}^5 + a_6 * \mathrm{PC} + a_7 * \mathrm{PC}^2 + a_8 * \mathrm{PC}^3 + a_9 * \mathrm{PC}^4 + a_{10} * PC^5 + a_{11} * \delta_s + a_{12} * \delta_s^2 + a_{13} * \delta_s^3 + a_{14} * \delta_s^4 + a_{15} * \delta_s^5 + a_{16} * \theta_t + a_{17} * \theta_t^2 + a_{18} * \theta_t^3 + a_{19} * \theta_t^4 + a_{20} * \theta_t^5 + a_{21} * \mathrm{M} * \mathrm{PC} + a_{22} * \mathrm{M} * \delta_s + a_{23} * \mathrm{M} * \theta_t + a_{24} * \mathrm{PC} * \delta_s + a_{25} * \mathrm{PC} * \theta_t + a_{26} * \delta_s * \theta_t + a_{27} * \mathrm{M} * \mathrm{PC} * \delta_s + a_{28} * \mathrm{M} * \mathrm{PC} * \theta_t + a_{29} * \mathrm{M} * \delta_s * \theta_t + a_{30} * \mathrm{PC} * \delta_s * \theta_t + a_{31} * \mathrm{M} * \mathrm{PC} * \delta_s * \theta_t$$

Because a good fit cannot be obtained for the whole engine deck data with one regression equation, boxes of different Mach number, altitude, and power code (PC) interval combinations are designated such that the union of the set of boxes encapsulates the design mission and other notional missions for the specific SST concept in question. These boxes were carefully chosen, and the team defined them to minimize the regression errors. The data from the engine deck are then filtered according to these boxes, and the regression exercise explained above is then used for each box, thus resulting in two regression equations, one for net thrust and one for fuel flow, for each designated box. Figure 55 shows the box selection for the 55- Pax Mach 1.8 SST concept, with the box selection for the ascent phase of the design mission in green

and the descent phase in blue. In this case, seven boxes would result in 14 equations. In addition, the box selection is unique for each SST concept, because each concept has a different design mission. A concept with a higher cruise speed and altitude might require more boxes to be defined to obtain good regression results than a concept with lower cruise speed and altitude.

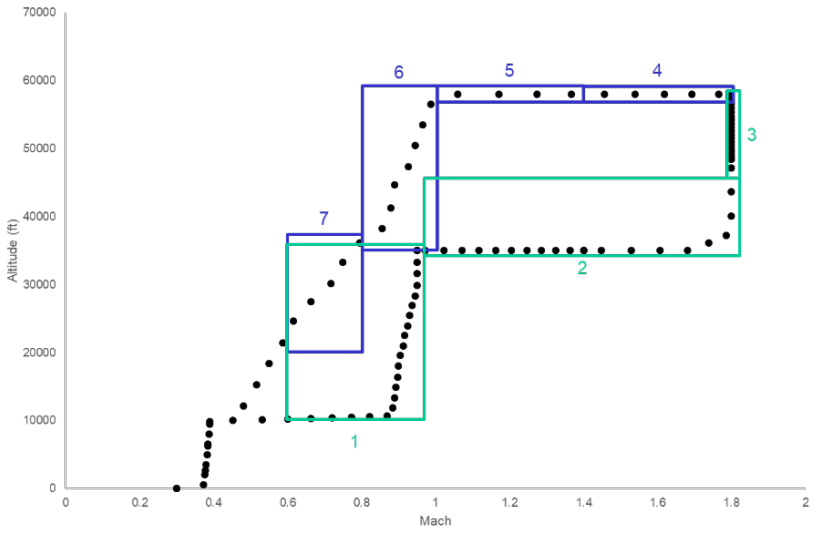

Figure 55. Propulsion box selection for the 55- Pax Mach 1.8 SST concept.

For evaluating the goodness of the fits for each box, the values for predicted value for net thrust and fuel flow that can be obtained with the regression equations and the values for net thrust and fuel flow from the concept engine deck are used to calculate the percentage error. Probability density function distributions are then constructed using JMP to visualize the error for each box individually. A standard deviation of less than 1, a mean equal to 0, and a percentage error values lower than 4% at the 97.5% and 2.5% quantiles are all indicative of a good regression. An example of these percentage error distributions is shown in Figure 56.

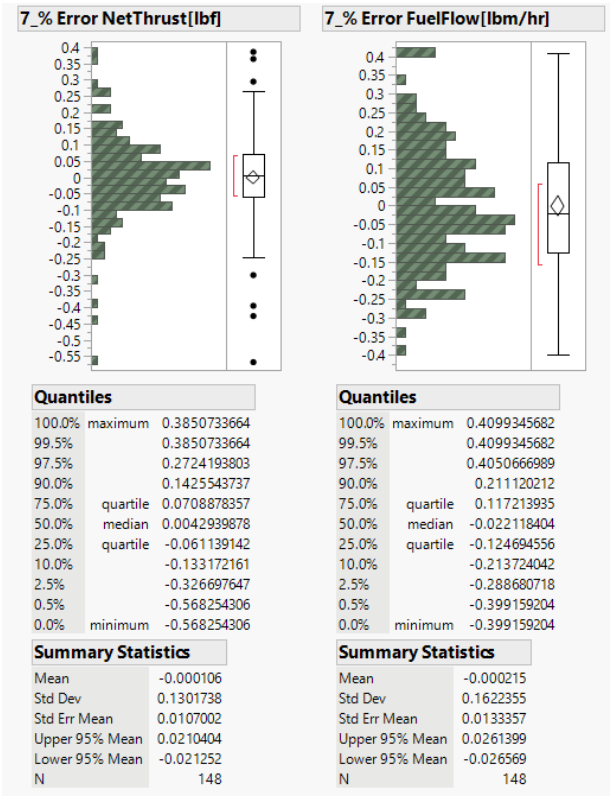

Figure 56. Percentage error distribution example.

After obtaining a promising set of regressions for a particular concept, the next step is to validate them against the concept's design mission and off-design mission data generated using FLOPS. This process is explained in more detail in the validation section below.

Aerodynamic Regressions

To generate coefficients for the regression of the coefficient of drag for each SST concept, the design team provided raw FLOPS data containing cardinal values of Mach number, C_L, altitude, and their corresponding C_D. The adopted strategy first regresses the drag coefficient on those cardinal values by using a stepwise fit before conducting a quadratic interpolation. This strategy was established after a comparison was performed between other strategies including the use of a stepwise fit on continuous variables (errors ranged between −25% and 50%), introduction of a large number of the cardinal values of C_L in the regression by using a stepwise fit coupled with a quadratic interpolation (error ranged between −6.1% and 8.6%). Using the latter strategy with fewer C_L cardinal values and introducing the Mach number as a cardinal value, empowering quadratic interpolation rather than stepwise regression, resulted in significantly better predictions (errors ranged between -1.4% and 1.8%). Hence, the team decided to exploit this strategy for all future aerodynamic regressions, using the latter strategy with fewer C_L cardinal values.

JMP was used to perform the stepwise regression of the drag coefficient on Mach number, altitude, and C_L number. Because the behavior of the drag coefficient is quite different between subsonic, transonic, and supersonic phases, we defined three boxes, one for each speed regime. The set of cardinal values was always chosen to encompass the design mission to avoid extrapolation. Figure 57 shows an example of a supersonic regime equation obtained with the stepwise fit analysis. Figure 58 allows for a graphical understanding of how the cardinal values were exploited to perform the regression.

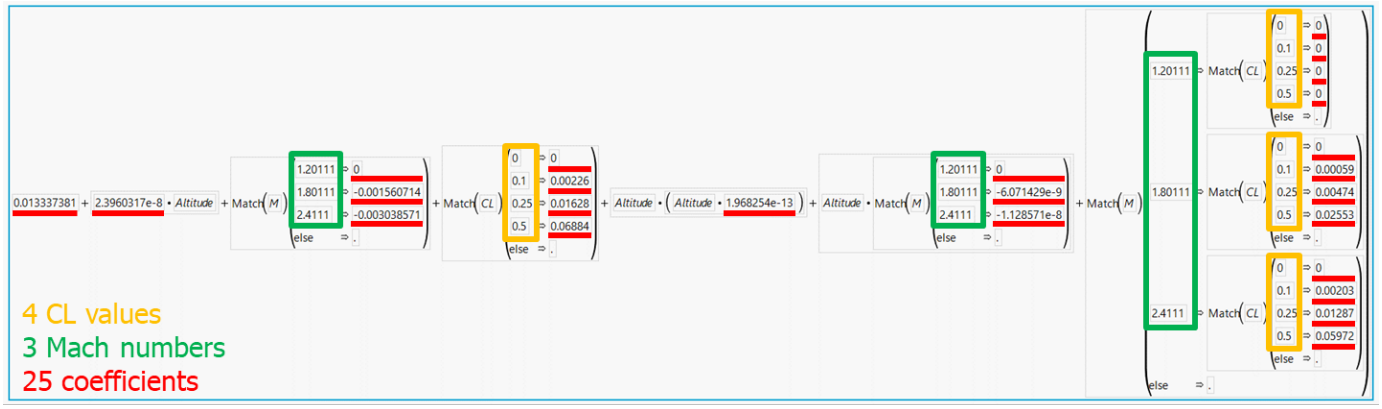

Figure 57. Form of the equation yielded by the stepwise fit on the cardinal values of Mach number (green) and C_L (yellow) and a continuous altitude.

	Altitude	Mach	CL	CD	Pred Formula CD - Subsonic	Pred Formula CD - Transonic	Pred Formula CD - Supersonic
1	0	0.3	0	0.00877	•	•	•
2	0	0.4	0	0.00813	•	•	•
3	0	0.5	0	0.00765	•	•	•
4	0	0.6	0	0.00748	0.007486633	•	•
5	0	0.7	0	0.00739	0.0073944108	•	•
6	0	0.8	0	0.00743	•	•	•
7	0	0.88	0	0.00771	0.0077230774	0.0077705694	•
8	0	1.05	0	0.01669	•	0.0167487013	•
9	0	1.2	0	0.01422	•	0.014294965	0.014
10	0	1.4	0	0.01271	•	•	•
11	0	1.6	0	0.01191	•	•	0.0117775
12	0	1.8	0	0.01085	•	•	•
13	0	2	0	0.01023	•	•	0.0101275
14	0	2.2	0	0.00982	•	•	•
15	0	0.3	0.05	0.00916	•	•	•
16	0	0.4	0.05	0.00853	•	•	•
17	0	0.5	0.05	0.00806	•	•	•
18	0	0.6	0.05	0.00792	•	•	•
19	0	0.7	0.05	0.00786	•	•	•

Figure 58. Example of the regression performed on cardinal values of Mach number, C_L, and altitude in JMP for the different regimes.

The design mission against which the regressions were validated did not have specific cardinal values; the Mach number, altitude, and C_L number were continuous. To enable good predictive capability for any input combination between the original cardinal values of the inputs, we developed a custom-made script to perform quadratic interpolation. The quadratic interpolation form is shown in Figure 59.

$$C_D = a_1 + a_2 h + a_3 h^2 + b_1 + b_2 h + c_1 + d_1$$

$$b_1 = \begin{cases} b_{1,1}, & if M = M_1 \\ b_{1,2}, & if M = M_2 \\ b_{1,3}, & if M = M_3 \end{cases} \quad b_2 = \begin{cases} b_{2,1}, & if M = M_1 \\ b_{2,2}, & if M = M_2 \\ b_{2,3}, & if M = M_3 \end{cases}$$

$$c_1 = \begin{cases} c_{1,1}, & if C_L = C_{L,1} \\ c_{1,2}, & if C_L = C_{L,2} \\ c_{1,3}, & if C_L = C_{L,3} \\ c_{1,4}, & if C_L = C_{L,4} \end{cases} \quad d_1 = \begin{cases} d_{1,1,1}, & if M = M_1 \text{ and } C_L = C_{L,1} \\ d_{1,2,1}, & if M = M_2 \text{ and } C_L = C_{L,1} \\ \vdots & \\ d_{1,3,4}, & if M = M_3 \text{ and } C_L = C_{L,4} \end{cases}$$

Figure 59. Form of the quadratic interpolation.

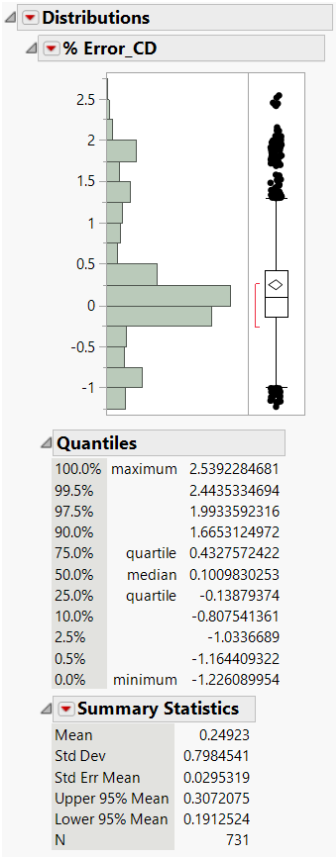

Figure 60. Total C_D error distribution example.

Figure 60 shows an example of total C_D error distribution after the quadratic interpolation. After the fit is satisfactory, the Mach-Alt combinations in the design mission are considered as the validation points.

Validation

The validation exercise consisted of using the propulsion and aerodynamic regressions to obtain values for thrust, fuel flow, and drag coefficient for the SST concept's design mission and off-design mission data generated through FLOPS, and comparing the predicted values to the actual values from those data by calculating the percentage error and constructing error distributions to visualize the results. To perform this exercise in a quick and efficient manner, a Python script was

created that takes the propulsion and aerodynamic regression equations, as well as the data from the FLOPS mission as inputs and calculates the percentage error between the predicted regression outputs and the actual FLOPS outputs for the net thrust, fuel flow, and drag coefficient. A flow chart indicating how the validation process works and how the Python script was developed is shown in Figure 61.

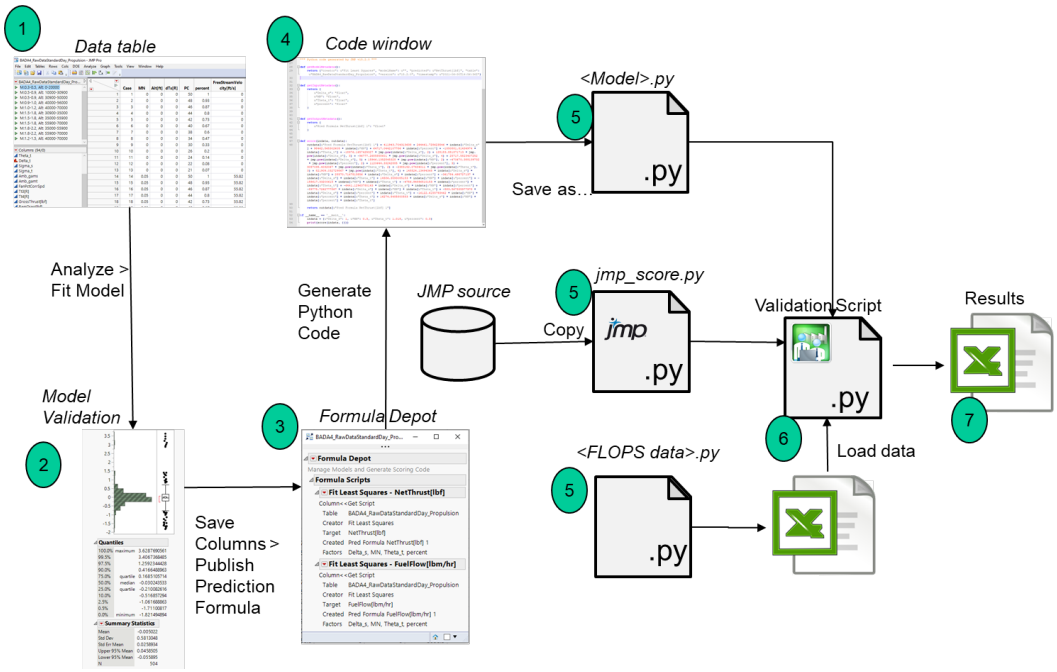

Figure 61. Validation process flow chart.

In addition to serving as a validation tool, the developed mission simulator also serves as a testbed to mimic the eventual implementation of the developed approach within AEDT. It has proven valuable in enabling discussions related to the eventual implementation within AEDT.

Because the FLOPS mission data do not contain values for static pressure ratio and total temperature ratio, atmospheric models must be incorporated into the code to calculate these values as functions of the altitude and Mach number. Various models were used for the troposphere (altitude < 36,089 ft) and stratosphere (altitude > 36,089 ft) portions of the mission data to account for the differences in how the static pressure ratio and total temperature ratio behave between the two regimes. The box selection used for the propulsion and aerodynamic regressions is also incorporated into the script, and the script automatically uses the corresponding regression equation for the segments of the mission data that fall into the designated boxes.

Results

The design mission validation results are presented below for the various SST concepts performed to date. For each, the box selection for the propulsion and aerodynamic regressions is shown, followed by the error distribution results from the validation exercise for each box. For the descent phases, residuals were calculated instead of percentage errors for net thrust, because FLOPS defaults the net thrust to 0 during descent, and therefore the percentage error cannot be calculated.

55- Pax Mach 1.8 SST

The propulsion and aerodynamic box selection of the 55- Pax Mach 1.8 aircraft are depicted in Figure 62. Boxes 1-3 correspond to the ascent phase of the flight, and boxes 4-7 correspond to the descent phase of the flight. Ideally, different boxes would be used as soon as an important change in the behavior occurs, so that the boxes would correspond to a single climb or a single cruise and for a single regime (subsonic, transonic, and supersonic); however, that practice would lead to an enormous number of boxes and some predictive ability would be lost when performing the off-design missions.

Tables 38–41 display the results of the validation mission regarding the propulsion (net thrust and fuel flow) and the aerodynamic (drag coefficient) analysis.

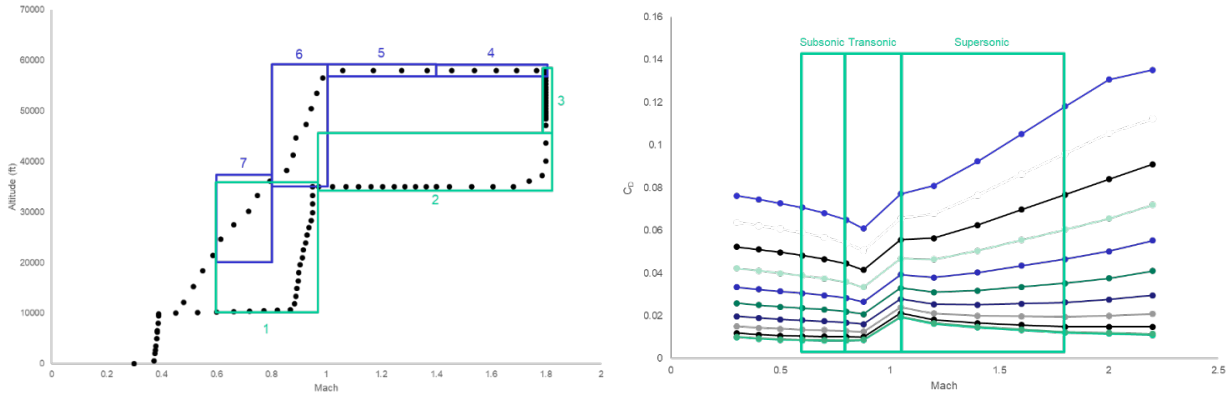

Figure 62. Box selection for the 55- Pax Mach 1.8 SST concept.

Table 38. Ascent net thrust design mission validation results for the 55- Pax Mach 1.8 SST concept.

Box	Minimum % Error	Maximum % Error	Mean	Std. Dev.
1	−0.2720	7.238	1.668	2.337
2	−6.012	1.444	−0.4509	2.181
3	−14.87	−5.453	−10.14	2.091

Table 39. Descent net thrust design mission validation results for the 55- Pax Mach 1.8 SST concept.

Box	Minimum Residual (lbf)	Maximum Residual (lbf)	Mean	Std. Dev.
4	1005	1043	-	-
5	645.6	958.0	-	-
6	649.7	1415	-	-
7	1521	2104	-	-

Table 40. Fuel flow design mission validation results for the 55- Pax Mach 1.8 SST concept.

Box	Minimum % Error	Maximum % Error	Mean	Std. Dev.
1	−0.8251	8.247	1.855	2.700
2	−4.196	1.617	−0.1447	1.585
3	−7.586	−3.662	−6.138	0.8677
4	1.295	5.914	3.788	2.031
5	−44.49	22.72	−2.264	29.88
6	−13.97	13.82	4.280	11.29
7	14.76	21.56	19.05	3.015

Table 41. Drag coefficient design mission validation results for the 55- Pax Mach 1.8 SST concept.

Box	Minimum % Error	Maximum % Error	Mean	Std. Dev.
Subsonic	−0.2149	0.09529	−0.06381	0.09991
Transonic	−3.083	0.3130	−0.1688	0.8298
Supersonic	−3.817	3.610	0.01050	1.509

55- Pax Mach 2.0 SST

As with the previous concept, box selection is depicted in Figure 63, and the propulsion and aerodynamic results are shown in Tables 42–45. A different strategy was implemented in this box selection. Four boxes were chosen for the ascent phase, and three boxes were chosen for the descent phase.

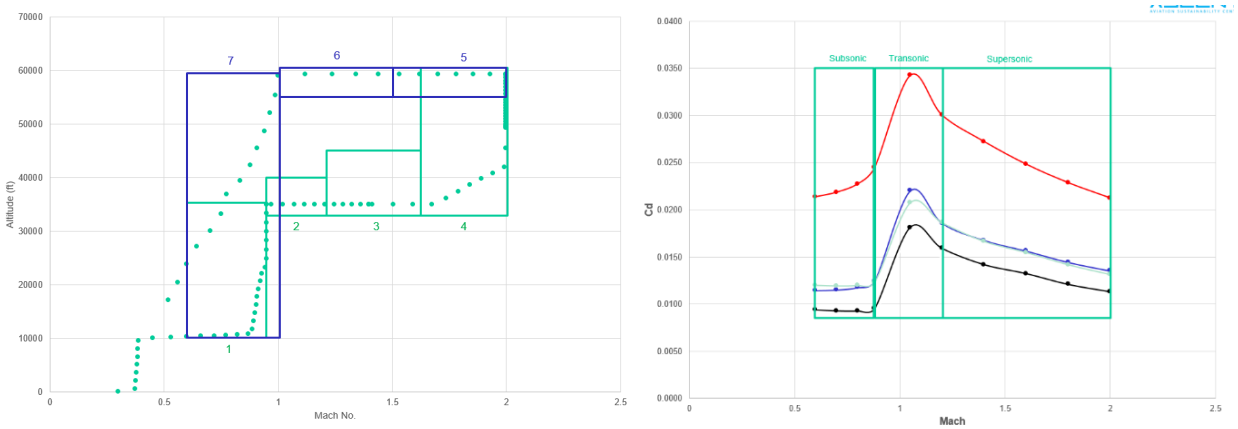

Figure 63. Box selection for the 55- Pax Mach 2.0 SST concept.

Table 42. Ascent net thrust design mission validation results for the 55 Pax Mach 2.0 SST concept.

Box	Minimum % Error	Maximum % Error	Mean	Std. Dev.
1	−0.6312	7.4679	2.1939	2.302
2	−0.6447	0.8229	0.0775	0.1855
3	−1.3195	0.5997	−0.2022	0.5306
4	−14.396	−0.0836	−8.26	4.8826

Table 43. Descent net thrust design mission validation results for the 55- Pax Mach 2.0 SST concept.

Box	Minimum Residual (lbf)	Maximum Residual (lbf)	Mean	Std. Dev.
5	1264.985	1357.4	-	-
6	378.317	1122.76	-	-
7	829.867	2626.8	-	-

Table 44. Fuel flow design mission validation results for the 55- Pax Mach 2.0 SST concept.

Box	Minimum % Error	Maximum % Error	Mean	Std. Dev.
1	−0.6	8.228	2.3948	2.6487
2	−0.5468	0.0735	−0.1963	0.2386
3	−0.2555	0.1888	−0.08954	0.1499
4	−6.7475	−0.07597	−4.2064	2.6087
5	1.146	7.995	4.6834	2.8265
6	−100	0.4387	−37.28	43
7	−11.53	22.80	11.05	11.015

Table 45. Drag coefficient design mission validation results for the 55- Pax Mach 2.0 SST concept.

Box	Minimum % Error	Maximum % Error	Mean	Std. Dev.
Subsonic	−0.5295	0.26315	−0.22175	0.2723
Transonic	−0.053	17.08	9.828	5.1841
Supersonic	−0.8344	2.46127	0.178	0.9405

The propulsion validation exercise for the different SST concepts revealed a clear distinction between the regression equation predictions for net thrust and fuel flow using the data from the engine deck and FLOPS calculations for these values in the design missions. This behavior was observed even though the goodness-of-fit exercise showed no significant error. To investigate this further, data from the engine deck was regressed and validated against themselves to ensure that the Python script was not the source of the error. This exercise yielded near-zero errors for net thrust and fuel flow. The cause of the small discrepancies was in the atmospheric models used by the script to obtain the static pressure ratio and total temperature ratio, which do not exactly match the values of these parameters in the engine deck.

The next step in investigating this issue was to take a point from the FLOPS design mission (Mach, altitude, and PC) and find two very similar points from the engine deck and check what the regressions equation predictions both cases. The results of this exercise are shown in Table 46. The results showed no significant error for the engine deck data points while showing a significant error for the FLOPS data point, although the data were similar. This result suggests that the method used by FLOPS to obtain values of net thrust and fuel flow for a given set of inputs does not match the data from the engine deck. For instance, the engine deck has no values of net thrust for any point close to zero, whereas FLOPS yields values of zero net thrust for any point in the mission categorized as part of the descent phase by default. Any differences in the behavior of the data, as in this example, are bound to cause some errors when the sets of data are validated against each other. This issue is currently being investigated further.

Table 46. FLOPS and engine deck propulsion data comparison.

Parameter	FLOPS Mission	Engine Deck 1			Engine Deck 2		
		Value	Predicted	% Error	Value	Predicted	% Error
MN	1.2734	1.25	1.25	-	1.3	1.3	-
Altitude (ft)	57981	58000	58000	-	58000	58000	-
PC	21	21	21	-	21	21	-
Net Thrust (lbf)	0	200.7	200.69	0.004983	216.2	216.3	-0.04163
Fuel Flow (lbm/hr)	2197	975.7	983.14	-0.7625	587.9	582.4	0.9304

The results for the aerodynamic regressions are promising overall and show no significant errors for most of the concepts. However, for a specific concept (55 Pax Mach 2.0 SST), the team is observing unexpected errors in the transonic phase, not in the entirety of the box/speed regime, but exclusively in between the cardinal number of Mach 0.88 and 1.05. The team is currently investigating the root cause of this issue.

Table 47. Aero data comparison 1.

Parameters	Validation Mission	Data Used for the First Interpolation			Data Used for the First Interpolation		
		Value	Predicted	% Error	Value	Predicted	% Error
MN	0.9453	0.88	0.88	-	1.05	1.05	-
Altitude (ft)	22,226	20,000	20,000	-	20,000	20,000	-
C_L	0.18679	0.19	0.19	-	0.1769	0.1769	-
C_D	0.01855	0.0166	0.01661	0.06	0.0252	0.025193	0.088

Table 48. Aero data comparison 2.

Parameters	Validation Mission	Data Used for the First Interpolation			Data Used for the First Interpolation		
		Value	Predicted	% Error	Value	Predicted	% Error
MN	0.9453	0.88	0.88	-	1.05	1.05	-
Altitude (ft)	22,226	25,000	25,000	-	25,000	25,000	-
C_L	0.18679	0.19	0.19	-	0.1769	0.1769	-
C_D	0.01855	0.0167	0.01671	0.04	0.0253	0.025321	0.066

Tables 47 and 48 above display the closest points found in the data table that were used to perform the initial regression. Their respective errors are all below 1% when the error for the validation mission point is at 17%.

Task 6 - GT Coordination

Georgia Institute of Technology and Purdue University

Objective

The main aim of this coordination task for Georgia Tech is to document interactions with other ASCENT projects as well as other stakeholders such as CAEP Working Groups, original equipment manufacturers (OEMs), and NASA. The research approach highlights only two interactions during the period of performance. The interactions with CAEP Working Groups are documented in the Results section of Task 4.

Research Approach (Georgia Tech)

The Georgia Tech modeling team has provided ASCENT Project 47 MIT researchers with results for the medium SST. During the period of performance, the Georgia Tech modeling team compiled the following information for the GT medium v11.4 closed vehicle and the v11.5 closed vehicle:

- General aircraft properties
  - Number of engines
  - Wing area
  - Wing inclination angle with the horizontal
  - Thrust inclination angle with the horizontal
  - Maximum takeoff weight (MTOW)
- Overall mission analysis
  - Design mission design
  - Total fuel wing capacity
  - Drag polar for clean configuration
  - Detailed mission segment performance
- Airframe constraint on engine size
- Takeoff and landing trajectories
  - Low speed (M < 0.35) aerodynamic properties of the full aircraft
- Noise footprint analysis
  - Airframe flap area
  - Horizontal tail area
  - Vertical tail area
  - Wing area
  - Flap span
  - Horizontal tail span
  - Vertical tail span
  - Wing span
  - Tire diameter of main landing gear
  - Tire diameter of nose landing gear

- Main landing gear strut length
- Nose landing gear strut length
- Number of wheels in main landing gear
- Number of wheels in nose landing gear
- Number of main landing gear
- Number of nose landing gear
- Number of slots for trailing edge flaps
- Flap setting (degrees deflected)
- Coordinates of the wing planform relative to the engine (i.e., top view of the aircraft)

Results (Georgia Tech)

VNRS Takeoff Trajectory

To examine the effects of takeoff trajectories on emission under 3,000 ft. The first step was to generate the relevant takeoff trajectories adhering to regulations. This was performed for both Georgia Tech's 55- passenger, Mach 2.2 SST (GT_MediumSST), and 8 passenger, Mach 1.4 representative supersonic business jet (GT_SSBJ). Four trajectories were established for comparison: 1) No cutback, 2) standard cutback, 3) advanced procedure and 4) a variable noise reduction systems (VNRS). The no cutback trajectory was a maximum thrust takeoff included as the antithesis to the "VNRS Min Noise" trajectory. After the obstacle, the aircraft holds a flight path angle (γ_{obs}) and accelerates to 250 kts (V_{trans}). It then transitions to holding 250 kts, increasing the flight path angle for the rest of the climb. The standard trajectory augmented the no cutback trajectory with a standard pilot-initiated cutback at some altitude (h_{cb}), which was optimized to minimize the combined takeoff certification noise levels at the lateral and flyover observers. The thrust setting for the cutback was determined in accordance with Title 14 CFR Part 36: Noise Standards: Aircraft Type and Airworthiness Certification. The advanced trajectory augmented the standard procedure with a programmed lapse rate (PLR) which is a FADEC initiated thrust reduction after gear retraction and is completed by 150 ft AG. PLR can be overridden by the pilot in emergencies, thus allowing for trading lower engine noise for a shallower/longer initial climb. A PLR with 90% thrust setting was used to match the assumptions of NASA. The advanced trajectory optimized the initial flight path angle, transition speed, and cutback height for the minimum combined takeoff certification noise levels at the lateral and flyover observers. The VNRS Min Noise trajectory used both PLR and PHLD controlled by the flight management system (FMS). For this trajectory, the amount of PLR, the initial flight path angle, the transition speed, and the cutback height were optimized for minimum cumulative noise. All trajectories were constrained (climb gradients, maximum airspeeds, etc.) to ensure compliance with all airworthiness requirements laid out in Title 14 CFR Part 25: Airworthiness Standards: Transport Category Airplanes. The engine deck used to assess the trajectories was for an $\mathrm{ISA} + 18\,°F$, a noise analysis standard condition. The trajectory parameters for GT_MediumSST-GT and GT_SSBJ are shown in Tables 49 and 50, respectively. A comparison of the flight path and thrust settings is shown in Figure 64 for the GT_MediumSST-GT and Figure 65 for the GT_SSBJ. The GT_MediumSST-GT VNRS trajectory had an increased climb time of 1.4 min relative to the standard trajectory. The GT_SSBJ VNRS trajectory had an increased climb time of 0.33 min relative to the standard trajectory.

Table 49. GT_MediumSST trajectory comparison.

Name	TS_{TO}	PLR					Cutback		PHLD	Time from 35 to 3,000 ft [s]	Average Thrust [%]
		h_{PLR} [ft]	TS_{PLR} [%]	γ_{obs}	V_{trans} [kts]	h_{trans} [ft]	h_{cb} [ft]	TS_{cb} [%]			
No Cutback	100%	–	–	12.75°	250	1999	–	–	No	31	100
Standard		–	–	9.6°	235.5	457	2290	39.2	No	44	76.2
Advanced		35	90	8.4°	235	500	2127	38.9	No	64	61.3
VNRS Min Noise		35	63	6.21°	232	583	1573	38.8	Yes	128	45.2

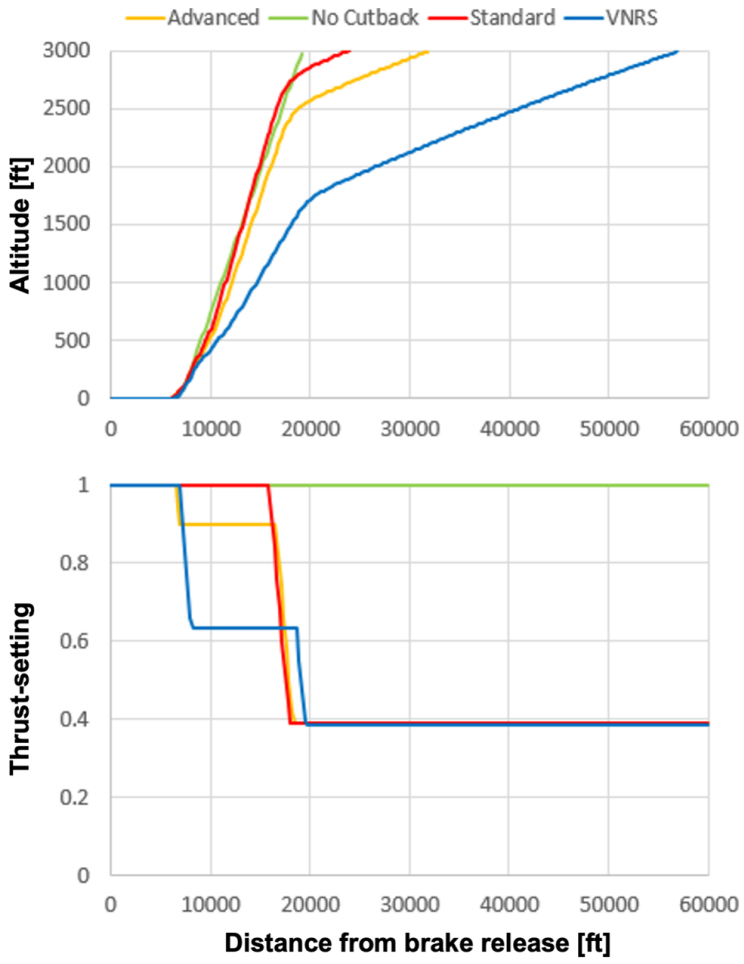

Figure 64. Altitude (top) and thrust setting (bottom) vs. distance from brake release for GT_MediumSST-GT trajectories.

Table 50. GT_SSBJ trajectory comparison.

Name	TS_{TO}	PLR					Cutback		PHLD	Time from 35 to 3,000 ft [s]	Average Thrust [%]
		h_{PLR} [ft]	TS_{PLR} [%]	γ_{obs}	V_{trans} [kts]	h_{trans} [ft]	h_{cb} [ft]	TS_{cb} [%]			
No Cutback	100%	-	-	3.5°	250	433	-	-	No	43.1	100
Standard		-	-	3.1°	250	374	1573	52.6	No	84.9	69.8
Advanced		35	90	2.9°	232	313	1522	53.9	No	82.5	67.8
VNRS Min Noise		35	78.4	3.3°	232	563	1143	53.8	Yes	105	62.2

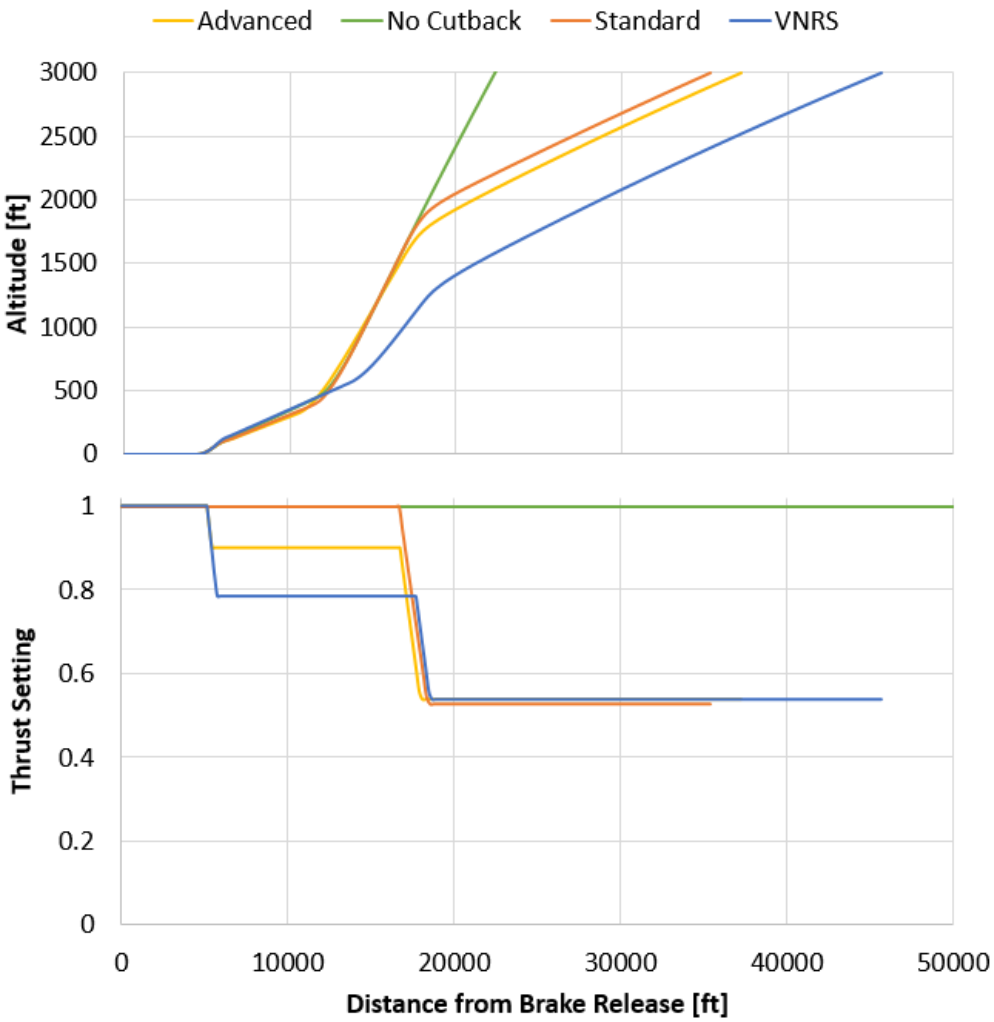

Figure 65. Altitude (top) and thrust setting (bottom) vs. distance from brake release for GT_SSBJ trajectories.

Emission Calculations

After the trajectories were determined, the cumulative NO_x as a function of time between 35 ft and 3,000 ft (i.e., climb out) was determined by integration over the discretized flight profile. The values for fuel flow and EI came from the engine deck. The GT_MediumSST-GT and GT_SSBJ assumed an RQL combustor technology based on the GE correlation, Equation 1, for EI_{NOx} from Niedzwiecki [**Error! Bookmark not defined.**]. The resultant cumulative NO_x for each trajectory of the GT_MediumSST-GT and GT_SSBJ is shown in Table 51.

$$\mathrm{EI_{NOx}} = 23.8 \left(\frac{P_3}{432.7\ \mathrm{psia}}\right)^{0.4} \exp\left(\frac{T_3 - 1027.6°\mathrm{F}}{349.9°\mathrm{F}} + \frac{6.29 - H_0}{53.2}\right) \quad \text{Equation 1}$$

where

P_3 is combustor entrance total pressure

T_3 is combustor entrance total temperature

H_0 is percentage humidity

Table 51. Cumulative NO_x[g] from 35 to 3,000 ft.

Trajectory	GT_MediumSST_GT			GT_SSBJ		
	NO_x [g]	Time from 35 to 3,000 ft [s]	Average Thrust [%]	NO_x [g]	Time from 35 to 3,000 ft [s]	Average Thrust [%]
No Cutback	1279	31	100	558	43.1	100
Standard	1182	44	76.2	626	84.9	69.8
Advanced	1122	64	61.3	572	82.5	67.8
VNRS Min Noise	1159	128	45.2	583	105	62.2
Subsonic Certification Rule	2568	132	85	1612	132	85
Supersonic Certification Rule	1202	120	65	752	120	65

Variability in Pt3, Tt3, FAR and EINO$_x$

As Pt_3, Tt_3, and fuel flow all affect EI and absolute NO_x production, these values are plotted as a function of the percentage maximum available thrust, Mach, and altitude for the VNRS trajectory. Additionally, an upper bound (Mach = 0.5, altitude = 0 ft) and a lower bound (Mach = 0, altitude = 2,500 ft) are included for reference to illustrate the ranges explored in CAEP12_WG3-5_ESTG_WP04 presented by [16]. All values are relative to the ICAO emissions 85% F00 climb point. The GT_MediumSST-GT is plotted in Figure 66, and the GT_SSBJ is plotted in Figure 67.

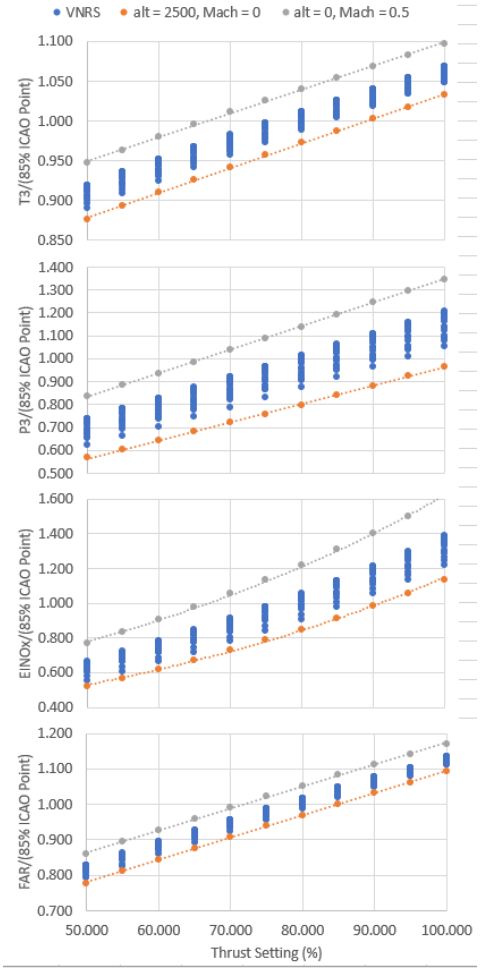

Figure 66. Variability in T_3, P_3, $\mathbf{EINO_x}$, and $\mathbf{FAR}$ with thrust setting for GT_MediumSST-GT.

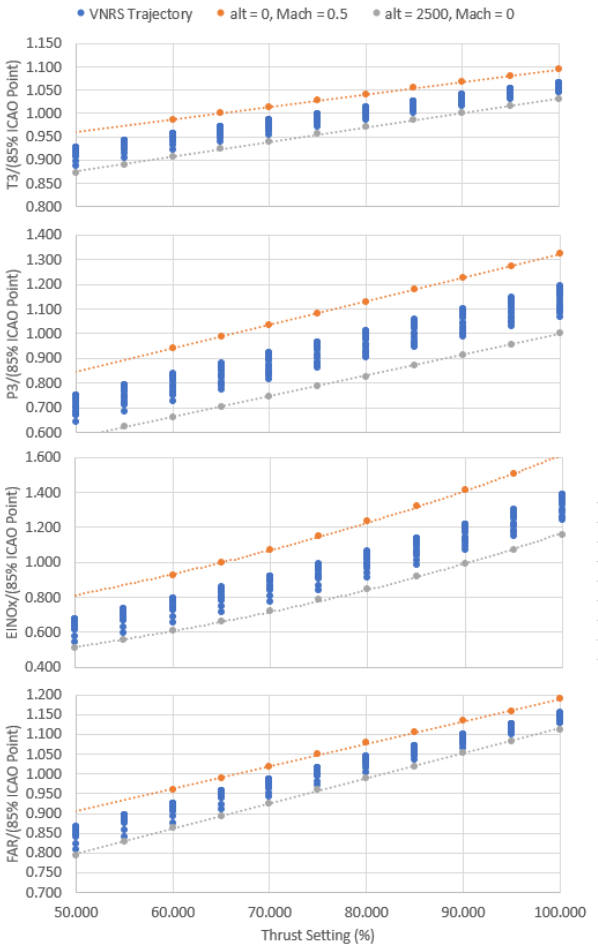

Figure 67. Variability in T_3, P_3, $\mathbf{EINO_x}$, **and FAR** with thrust setting for GT_Medium_SST-GT.

Task 6 - Purdue Coordination

Objectives

This objective comprised coordinating with entities involved in CAEP MDG/FESG, particularly the SST demand task group. In addition, this objective included maintaining the ability to incorporate SST vehicle models designed by our Georgia Tech colleagues and/or SST models developed by others.

Research Approach

For the period of performance covered in this report, the Purdue team was not asked to participate directly in many coordination activities. We did provide updates when requested by our FAA technical monitors, who were active in the CAEP efforts. We have also maintained an approach in FLEET that will allow, with low effort, representation of the performance of aircraft other than the notional lA10 medium SST. To date, the Purdue team has considered only the notional A10 medium SST, but we are prepared to incorporate other aircraft models.

Publications

Jain, S., Mane, M., Crossley, W. A., & DeLaurentis, D. A. Investigating How Commercial Supersonic Aircraft Operations Might Impact Subsonic Operations and Total CO_2 Emissions, AIAA 2021-3014. AIAA Aviation 2021 Forum. August 2021

Mane M., Jain, S., Crossley, W. A. Estimating Market Size for Supersonic Passenger Transport Aircraft, AIAA 2021-2442. AIAA Aviation 2021 Forum. August 2021.

Submitted conference proceedings

Fung, T., Yang, B., Jain, S., Chao, H., Mane, M., Crossley, W. A., & DeLaurentis, D. Fleet-Level Impacts of Different Commercial Supersonic Aircraft Configurations Considering A World-Wide Route Network. Abstract submitted to AIAA Aviation Forum for presentation in June 2022

Yang, B., Fung, T., Jain, S., Chao, H., Mane, M., Crossley, W. A., & DeLaurentis, D. A. Estimating Future Fleet-Level CO2 Emissions Considering a World-Wide Network. Abstract submitted to AIAA Aviation Forum for presentation in June 2022

Outreach Efforts

Multiple interactions with government, industry, and academia have occurred during the course of the project.

ASCENT 10: Aircraft Technology Modeling and Assessment, oral presentation to ASCENT Fall Advisory Committee Meeting, GT, Virtual, September 2020.
ASCENT 10: Aircraft Technology Modeling and Assessment, poster presentation to ASCENT Spring Advisory Committee Meeting, GT, Virtual, April 2021.

Awards

None

Student Involvement

The Georgia Tech student team consists of 11 graduate research assistants (GRA). During the period of performance, the GRA team was organized by vehicle class, i.e., SSBJ, medium SST, and large SST. However, the student members of the team each also supported the disciplinary analysis that best matched their research interests. The disciplinary areas included geometry, aerodynamics, propulsion, weights, noise, mission analysis, and fleet assessment. GRA leads were identified for each topic. Ms. Barbara Sampaio and Mr. Brennan Stewart are the student leads for aerodynamics; Mr. Edan Baltman is the student lead for propulsion; Mr. Brennan Stewart is the student lead for geometry; Mr. Joao De Azevedo is the student lead for noise; Mr. Colby Weit is the student lead for mission analysis; and Mr. Jiajie (Terry) Wen is the student lead for demand and fleet assessment.

The Purdue team included four graduate students over the 1-year period, all of whom have been conducting tasks in support of the effort. Samarth Jain, a continuing PhD student at Purdue, worked on the effort for the entire period. Hsun Chao, a PhD student, moved primarily to another research project but still supports the ASCENT 10 effort in an advisory capability. Suzanne Swaine, a PhD student, participated in the Purdue team through most of this reporting period. In addition, the Purdue team added Boning “Willis” Yang and Tien-Yueh “Edward” Fung, both MS students in Aeronautics and Astronautics, to the team during this reporting period.

Plans for Next Period

Georgia Tech

The plans for the next period include two focus areas: AEDT supersonic modeling implementation and supersonic fuel burn and LTO noise interdependencies. The AEDT supersonic modeling includes working with supersonic airframers and engine OEMs to generate aerodynamics and propulsion regression coefficients to be tested in AEDT. The Georgia Tech modeling team will continue to improve on the SST designs to capture both fuel burn and LTO noise and examine the interdependencies between these two metrics. The modeling team will also be working with both supersonic airframers and engine OEMs to verify assumptions and review results. Other SST classes, i.e., 25 and 75 passenger aircraft, will also be investigated.

Purdue

The Purdue team successfully demonstrated FLEET’s capabilities for modeling and analyzing the introduction of commercial supersonic aircraft to an existing all-subsonic airline fleet model. This demonstration has shown that FLEET is capable of predicting the changes in subsonic aircraft operations on routes where supersonic aircraft also operate (to compensate for the shifting of subsonic business class and above passengers to supersonic aircraft – based on supersonic demand), along with predicting the number of round trips and the number of passengers carried on such routes. The Purdue team also predicted the changes in future supersonic demand and its impacts on supersonic and subsonic operations, depending on various COVID-19-related projected demand scenarios. Additionally, the team successfully developed a “simultaneous”

allocation approach wherein the supersonic and subsonic aircraft are allocated together on the basis of supersonic and subsonic passenger demand. The Purdue team is in the process of updating its route network from a U.S.-touching-only network to a worldwide network.

Future work will include completing FLEET's airline network update to a global network (moving away completely from the U.S. flag carrier airlines only route network currently implemented in FLEET). The team will also assess the fleet-level advantage of having different types and sizes of supersonic aircraft, defined by certain operational specifications (e.g., Mach cutoff over land) and passenger capacity (e.g., 100-seat supersonic aircraft), available to the FLEET global airline. Future work will also include developing a FLEET-like tool for SSBJ operations.

References

Airline Origin and Destination Survey – DB1B [online database], U.S. Dept. of Transportation, Bureau of Transportation Statistics.

Boeing Market Outlook, "Boeing Current Market Outlook 2012-2031", 2012, Retrieved October, 2021. URL http://libraryonline.erau.edu/online-full-text/books-online/Boeing_Current_Market_Outlook_2012.pdf.[19]

IATA Economic Reports, "Air Passenger Market Analysis", December 2020, Retrieved June, 2021. URL https://www.iata.org/en/iata-repository/publications/economic-reports/air-passenger-monthly-analysis---december-2020/.

IATA Press Release, "2020 Worst Year in History for Air Travel Demand", February 2021, Retrieved June, 2021. URL.

IATA Press Release No: 33, "Optimism When Borders Reopen", May 2021, Retrieved June, 2021. URL https://www.iata.org/en/pressroom/pr/2021-05-26-01/.

ICAO, "Effects of Novel Coronavirus (COVID-19) on Civil Aviation: Economic Impact Analysis,", June 2021, Retrieved June, 2021. URL https://www.icao.int/sustainability/Documents/COVID-19/ICAO_Coronavirus_Econ_Impact.pdf.

Mavris, D., DeLaurentis, D., Crossley, W., and Alonso, J. J. (2017), "Project 10 Aircraft Technology Modeling and Assessment: Phase I Report", 2017.

OAG Traffic Analyzer [online database], Official Aviation Guide, Retrieved Dec. 2020. URL https://www.oag.com/traffic-analyzer.

Pearce, B., "COVID-19: An almost full recovery of air travel in prospect," IATA Economic Reports, May 2021, Retrieved June, 2021. URL https://www.iata.org/en/iata-repository/publications/economic-reports/an-almost-full-recovery-of-air-travel-in-prospect/.

"SeatGuru by Tripadvisor", Retrieved Mar. 2019. URL https://seatguru.com/.17.

Wyman, O., "Oliver Wyman Global Fleet & MRO Market Forecast Summary 2017-2027", 2017, Retrieved October, 2021. URLhttps://www.oliverwyman.com/our-expertise/insights/2017/feb/2017-2027-fleet-mro-forecast.html.

Aftomis, Michael J., Berger, Marsha J. and Alonso, Juan J. (2006) "Applications of a Cartesian Mesh Boundary-Layer Approach for Complex Configurations". 44th AIAA Aerospace Sciences Meeting, Reno NV,

Blake, M., Smith, J., Wright, K., Mediavilla, R., Kirby, M., Pfaender, H., Clark, J.P., Volovoi, V., Dorbian, C., Ashok, A. (2010). "Advanced Vehicle concepts and implications for NextGen." NASA CR-2010-216397

Dubois, D. & Paynter, G.C. (2006), "Fuel flow method 2 for estimating aircraft emissions," SAE Transactions Vol. 115, pp. 1-14, Section 1: Journal of Aerospace

The Concorde Flying Manual Volume II. (1976). British Airways Overseas Division with later amendments.

Annual Energy Outlook 2011. (2011). U.S. Energy Information Administration

Bachman, J. (2016). "Supersonic is coming back. Will the airlines buy it?" Bloomberg

Barnhart, P. J. *IPAC - Inlet Performance Analysis Code*. 1997.

Bogaisky, J. (2018). "GE reveals engine that could make Aerion's ambitious supersonic business jet take flight." Forbes

Crichton, D., de la Rosa Blanco, E., Law, T., & Hileman, J. (2007). "Design and operation for ultra-low noise take-off," AIAA 45th Aerospace Sciences Meeting and Exhibit, January 8-11, 2007.

de la Rosa Blanco, E., Hall, C., & Crichton, D. (2007). "Challenges in the silent aircraft engine design," AIAA 45th Aerospace Sciences Meeting and Exhibit, January 8-11, 2007.

Hartmann, A. (1967). "Theory and test of flow mixing for turbofan engines," AIAA 3rd Propulsion Joint Specialist Conference, Vol. 5, No. 6, pp. 522–527. DOI:10.2514/3.43978

Kowalski, E.J. & Atkins Jr., R.A. (1979). "A computer code for estimating installed performance of aircraft gas turbine engines." Advanced Airplane Branch Boeing Military Airplane Company, Vol. I - Final Report

Kuchar, A.P. (1989). "Variable convergent-divergent exhaust nozzle. General Electric Company Aircraft Engine Group", AIAA Education Series, 1989, Chapter 5 of Aircraft Propulsion Systems Technology and Design.

Li, W., Shields, E., & Le, D. (2008). "Interactive inverse design optimization of fuselage shape for low-boom supersonic concepts." Journal of Aircraft, Vol. 45, No. 4, July – August 2008.

Mattingly, J. (2002). Aircraft engine design, AIAA Education Series.
Ozgen, S. (2017). AE 451 aeronautical engineering design I. Middle East Technical University
Pearson, H. (1962). "Mixing of exhaust bypass flow in bypass engine," Journal of The Royal Aeronautical Society, Vol. 66, No. 620, pp. 528–530.
Pratt & Whitney, and General Electric Aircraft Engines. Critical Propulsion Components Volume 1: Summary, Introduction, and Propulsion Systems Studies. 2005.
Raymer, D. (2004). Aircraft design: A conceptual approach. AIAA 1992
Rech, J. & Leyman, C.S. (1981). A case study by Aerospatiale and British aerospace on the Concorde. AIAA Professional Study Series
Scholz, E. (2017). Aircraft design – an open educational resource. Hamburg Open Online University
Schutte, J.S. (2009). "Simultaneous multi-design point approach to gas turbine on-design cycle analysis for aircraft engines," Ph.D. Thesis, Georgia Institute of Technology, May 2009.
Thornock, R.L. & Brown, E.F. (1972). "An experimental study of compressible flow through convergent-conical nozzles, including a comparison with theoretical results," Journal of Basic Engineering, pp.926-930.
Welge, H.R., Bonet, J., Magee, T., Chen, D., Hollowell, S. Kutzmann, A., Mortlock, A., Stengle, J., Nelson, C., Adamson, E., Baughcum, S., Britt, R., Miller, G., Tai, J. (2010). "N+2 supersonic concept development and systems integration," NASA-CR-2010-216842.
Whitcomb, R.T. (1966). "Some consideration regarding the application of the supersonic area rule to the design of airplane fuselages,' NACA Research Memorandum, National Advisory Committee for Aeronautics, Washington, July 1966.
Young, J.B. & Wilcock, R.C. (2002). "Modeling the air-cooled gas turbine part 2-coolant flows and losses," Journal of Turbomachinery, 124(2): pp. 214-221.
Air France, 2003. Manuel d'utilisation Concorde.
Airlines for America, 2017. A4A Passenger Airline Cost Index (PACI).
Boeing, 2019. Commercial market outlook 2019–2038.
Bresenham, J.E., 1965. Algorithm for computer control of a digital plotter. IBM Systems Journal 4, 25–30.
BTS, 1995. American Travel Survey (ATS) 1995. https://www.transtats.bts.gov/.
Daniel, K., Nash, A., Koeing, S., Felner, A., 2010. Theta*: Any-angle path planning on grids. Journal of Artificial Intelligence Research 39, 533–579.
FAA, 2015. 2015 inventory as modeled in Aviation Environmental Design Tool (AEDT).
FAA, 2018. FAA aerospace forecast – fiscal years 2018-2038.
FAA, 2020. Aviation Environmental Design Tool (AEDT) version 3c – user manual.
Graver, B., Rutherford, D., 2018. Transatlantic airline fuel efficiency ranking, 2017.
Hassan, M., Pfaender, H., Mavris, D., 2020. Design tools for conceptual analysis of future commercial supersonic aircraft, in: AIAA Aviation 2020 Forum. doi:10.2514/6.2020-2620.
Henne, P.A., 2005. Case for small supersonic civil aircraft. Journal of Aircraft 42, 765–774.
IATA, 2019. IATA economics chart of the week: Air travel frequency flattens in developed markets, rises in emerging markets.
Liebhardt, B., 2019. Sonic boom carpet computation as a basis for supersonic flight routing, in: AIAA Aviation 2019 Forum, p. 3387.
Liebhardt, B., Gollnick, V., Lütjens, K., 2011. Estimation of the market potential for supersonic airliners via analysis of the global premium ticket market, in: 11th AIAA Aviation Technology, Integration, and Operations (ATIO) Conference, p. 6806.
Liebhardt, B., Linke, F., Dahlmann, K., 2014. Supersonic deviations: Assessment of sonic-boom-restricted flight routing. Journal of Aircraft 51, 1987–1996. doi:10.2514/1.C032591.
Liebhardt, B., Lütjens, K., Tracy, R., Haas, A., 2017. Exploring the prospect of small supersonic airliners – A case study based on the Aerion AS2 jet, i17th AIAA Aviation Technology, Integration, and Operations (ATIO) Conference, p. 3588.Mavris, D., DeLaurentis, D., Crossley, W., & Alonso, J. J. (2017). Project 10 aircraft technology modeling and assessment: Phase I report.
Sun, Y., Smith, H., 2017. Review and prospect of supersonic business jet design. Progress in aerospace sciences 90, 12–38.
WID, 2019. World Inequality Database (WID). https://wid.world/data/.
Zheng, X.S., Rutherford, D., 2019. U.S.–Latin America airline fuel efficiency ranking, 2017–2018.

Task 4 References

[1] Salas Nunez, L., Tai, J. C., & Mavris, D. N. (2021). The Environmental Design Space: Modeling and Performance Updates. January, 1–15. https://doi.org/10.2514/6.2021-1422

[2] Kirby, M. R., & Mavris, D. N. (2008). The Environmental Design Space. 26th International Congress of the Aeronautical Sciences ICAS, 1–9.

[3] HARTMANN, A. (1967). Theory and test of flow mixing for turbofan engines. AIAA 3rd Propulsion Joint Specialist Conference, 5(6), 522–527. https://doi.org/10.2514/3.43978

[4] Pearson, H. (1962). Mixing of Exhaust Bypass Flow in Bypass Engine. Journal of the Royal Aeronautical Society, 66(620), 528–530.

[5] Berton, J. J., Haller, W. J., Senick, P. F., Jones, S. M., & Seidel, J. A. (2005). A comparative propulsion system analysis for the high-speed civil. Nasa/Tm—2005-213414, December.

[6] SEIDEL, J., HALLER, W., & BERTON, J. (1991). Comparison of turbine bypass and mixed flow turbofan engines for a high-speed civil transport. AIAA Aircraft Design Systems and Operations Meeting. https://doi.org/10.2514/6.1991-3132

[7] Welge, H. R., Bonet, J., Magee, T., Chen, D., Hollowell, S., Kutzmann, A., Mortlock, A., Stengle, J., Nelson, C., Adamson, E., Baughcum, S., Britt, R. T., Miller, G., & Tai, J. (2010). N+2 Supersonic Concept Development and Systems Integration. http://www.sti.nasa.gov

[8] Kowalski, E.J. & Atkins Jr., R.A. (1979). "A computer code for estimating installed performance of aircraft gas turbine engines." Advanced Airplane Branch Boeing Military Airplane Company, Vol. I - Final Report

[8] https://software.nasa.gov/software/LEW-19686-1

[10] Gauntner, J. W. (1980). Algorithm for Calculating Turbine Cooling Flow and Resulting Decrease in Turbine Efficiency. https://ntrs.nasa.gov/search.jsp?R=19800011581

[11] Grondahl, C. M., & Tsuchiya, T. (2001). Performance benefit assesment of ceramic components in an MS9001FA gas turbine. Journal of Engineering for Gas Turbines and Power, 123(3), 513–519. https://doi.org/10.1115/1.1335476

[12] Schutte, J. S. (2009). SIMULTANEOUS MULTI-DESIGN POINT APPROACH TO GAS TURBINE ON-DESIGN CYCLE ANALYSIS FOR AIRCRAFT ENGINES.

[13] Denney, R. K., Tai, J. C., Kestner, B. K., & Mavris, D. N. (2005). Variable Cycle Optimization for Supersonic Commercial Applications. In Source: SAE Transactions (Vol. 114).

[14] Pratt & Whitney, & General Electric Aircraft Engines. (2005). Critical Propulsion Components Volume 2: Combustor. https://ntrs.nasa.gov/citations/20050185254

[15] Niedzwiecki, R. W. (1992). Low Emissions Combustor Technology for High-Speed Civil Transport Engines.

[16] ICCAIA CAEP12_WG3-5_ESTG_WP04